Experimental and CFD investigation of gas phase freeboard combustion

Andersen, Jimmy; Glarborg, Peter; Jensen, Peter Arendt; Lovmand Hvid, Søren

Publication date:
2009

Document Version
Publisher's PDF, also known as Version of record

Experimental and CFD investigation of gas phase freeboard combustion

PhD Thesis

Jimmy Andersen

Technical University of Denmark
Department of Chemical Engineering
CHEC research group
2009

Preface

This thesis is written in partial fulfilment of the requirements to obtain the Doctor of Philosophy degree (PhD) at the Technical University of Denmark (DTU).

The work has been carried out from May 2006 to May 2009 at the Combustion and Harmful Emission Control (CHEC) Research Centre, Department of Chemical Engineering, DTU. The project has been supervised by Prof. Peter Glarborg, Ass. Prof. Peter Arendt Jensen and Senior Engineer Søren Lovmand Hvid.

The work was financed by the Technical University of Denmark, DONG Energy, Vattenfall, Babcock & Wilcox Vølund, B&W Energy, The Danish Technical Research Council, and the Public Service Obligation programme under contract PSO 4792.

I would like to express my sincere thanks to a number of people who have contributed to this project. First of all my supervisors for their guidance, inspiration and feedback. Students Kristian Nørgaard and Trine Mosgaard Giselsson for their hard work, and technicians Thomas Wolfe and Henrik Kløft for technical guidance.

Thanks to friends, fellow PhD students and other colleagues at CHEC for their help and support during the last three years. Finally thanks to my family, my wife, Stine, and my children, Alexander and Amalie, for bearing over with me during this work.

Jimmy Andersen Esbjerg, Denmark Dec 30th, 2009

Abstract

Reliable and accurate modeling capabilities for combustion systems are valuable tools for optimization of the combustion process. This work concerns primary precautions for reducing NO emissions, thereby abating the detrimental effects known as “acid rain”, and minimizing cost for flue gas treatment.

The aim of this project is to provide validation data for Computational Fluid Dynamic (CFD) models relevant for grate firing combustion conditions. CFD modeling is a mathematical tool capable of predicting fluid flow, mixing and chemical reaction with thermal conversion and transport. Prediction of pollutant formation, which occurs in small concentrations with little impact on the general combustion process is in this work predicted by a post-processing step, making it less computationally expensive.

A reactor was constructed to simulate the conditions in the freeboard of a grate fired boiler, but under well-defined conditions. Comprehensive experimental data for velocity field, temperatures, and gas composition are obtained from a 50 kW axisymmetric non-swirling natural gas fired combustion setup under two different settings. Ammonia is added to the combustion setup in order to simulate fuel-NO formation during grate firing biomass combustion conditions. The experimental results are in this work compared to CFD modeling. The modeling results show, that the CFD model captured the main features of the combustion process and flow patterns. The application of more advanced chemical reaction mechanisms does not improve the prediction of the overall combustion process, but do provide additional in-

formation about species (especially H_2 and radicals), which is desirable for post-processing pollutant formation.

NO formation is post-processed using various ammonia oxidation schemes and different post-processing techniques. The results in some cases provide a reasonable agreement with the experimental data. In general the application of advanced combustion modeling and more advanced ammonia oxidation mechanisms does not improve the agreement with experimental data compared to the simple eddy dissipation (mixed is burned) approach with post processing of a global combustion mechanism.

The experimental setup does however not serve as a perfect validation case. The Reynolds numbers in the system put the flow regime in the transitional region, where turbulence modeling is difficult. Furthermore, the inclined jets show an affinity towards wall attachment, the entire modeling result is very sensitive to the prediction of these jets.

Resumé

Pålidelig og præcise modelleringsevner er et værdifuldt værktøj til at optimere forbrændingssystemer og processer. Optimering af forbrændingsprocessen er et oplagt primært tiltag til at reducere NOx emissioner og dermed reducere de skadelige miljøkonsekvenser såsom syreregn, og medvirke til at minimere omkostninger ved sekundær rensning af røggassen.

Formålet med dette projekt er at levere valideringsdata til numeriske fluid mekaniske modeller (CFD), specifikt henvendt til ristefyrings forhold. CFD modellering er et matematisk værktøj, som kan forudsige strømningsforhold, opblanding, kemisk reaktioner og medfølgende varmeudvikling og transport. Forudsigelse af dannelse af forureningsprodukter, som oftest forekommer i lave koncentrationer med lille indflydelse på den generelle forbrændingsproces, kan estimeres med et post-processeringstrin, hvilket reducerer de beregningsmæssige omkostninger betydeligt.

En model reaktor er blevet bygget med det formål at simulere forholdene i fribordet på et ristefyret forbrændingsanlæg, men under kontrollerede forhold. De eksperimentelle måleresulter er i dette studie sammenholdt med CFD modelleringsresultater.

Eksperimentel resultater indbefatter en omfattende kortlægning af reaktore med hensyn til hastighedsfelter, temperaturer og gas sammensætning er målt i en 50kW aksesymmetrisk naturgasfyret forbrændingsreaktor. Ammoniak blev tilført forbrændingen for at simulere dannelse af brændsels-NOx under biomasse ristefyrings forhold.

Modelleringsresultater viser, at CFD modellen fanger de generelle forhold,

hvad angår forbrændingsproces og strømningsforhold. Brug af mere avancerede forbrændingsmekanismer forbedrede ikke overensstemmelsen med målte data, men tilførte resultater for gasfase komponenter (specielt H_2 og radikaler), som er påkrævet for efterfølgende at estimere NOx dannelse.
Bestemmelse af NOx dannelse er gjort med forskellige ammoniak oxidationsmekanismer. Resultaterne giver i nogle tilfælde en god overensstemmelse med med målte data. Generelt er der dog ikke opnået en væsentlig bedre overensstemmelse mellem måle og modelleringsdata, ved at anvende mere avancerede forbrændings og ammoniak oxidationsmekanismer, hvor der er opnået udmærket overensstemmelse ved brug af en simpel opblandingsbestem forbrændingsrate og en simpel ammoniak mekanisme.
Dette gør at forsøgsanlægget nok ikke er perfekt til valideringsformål. Reynolds tallet i systemet viser at strømningen ikke er fuldt turbulent, hvilket er bekymrende, da dette er en vigtig antagelse for mange af de anvendte modeller. Desuden er de skrå luftdyser som leverer sekundærluften tilbøjelige til at påhæfte sig på reaktor væggen, hvilket gør flowforholdene og dermed hele processen meget følsom og ustabil.

Contents

List of Figures

List of Tables

Chapter 1

Introduction

Renewable fuels such as biomass and waste are becoming increasingly important as fuels in energy production, in order to decrease the fossil fuel dependence and CO_2 emissions. In the coming years the change of energy source from fossil fuels to renewable energy sources will increase. In Denmark wind power is an important technology in this transition toward sustainable energy production, however wind power is non-dispatchable, meaning that the energy output must be taken when it is available, and other resources, primarily sustainable thermal power production must be used to match supply with demand. An increased and effective utilization of biomass and waste is therefore increasingly important for the energy production of tomorrow.

Biomass fuels are characterized by having significantly lower heating value and higher moisture content than fossil fuels [1]. In addition the composition and characteristics of biomass fuels and waste can vary significantly. Another well known implication with biomass fuels is the often high content of alkali chlorides, which causes deposition and corrosion problems in thermal power plants. [2, 3]

The grate firing technology is often applied for combustion of biomass and waste. The advantage of the grate firing technology is that it can handle coarse fuels, fuel diversity and high moisture contents [4]. However due to the corrosion issues, biomass plants are often run at lower steam temperatures

than fossil fuel powered plants, with comparatively lower electrical efficiency. Other techniques often used in thermal conversion of biomass are fluidized bed combustion [5] which offers some of the same advantages and drawbacks as grate firing. Biomass is also included in energy production in co-firing with pulverized coal [6, 7], this causes serious challenges for fuel handling, but have advantages in corrosion reduction due to sensitizing effects between the fuel types.

Figure 1.1 illustrates a grate combustion process. The fuel enters from the left side typically fed in by a stoker. The relatively coarse and moist fuel then falls to the grate, where it is transported to the right typically by grate movements (vibrations, side to side movements or continuous caterpillar track traveling).

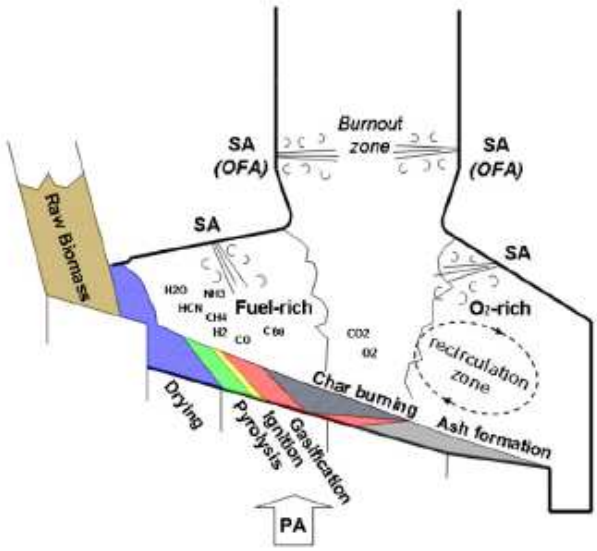

Figure 1.1: Illustration of the grate combustion concept [4].

While on the grate the fuel undergoes thermal conversion initiated by a drying step. At temperatures around 200-400 °C [8] the pyrolysis process initiates and volatile compounds such as hydrocarbons, CO, H_2 and fuel bound nitrogen compounds are released during the pyrolysis and gasification steps. In biomass nitrogen is usually fixated in some kind of amine or amid

structure [9], which primarily will be released as NH_3 [10]. HCN and HNCO are however also observed released from biomass pyrolysis [11].
Further down on the grate the remaining char will react with the primary air in a char burnout step. The nitrogen constituent released from this process will primarily be NO [12]. This leaves only ash left on the grate.
Above the grate in the freeboard section the released compounds will react with supplied secondary and over fire air.

1.1 CFD modeling of grate fired boilers

Computational Fluid Dynamics (CFD) is a powerful tool for predicting flow and thermal conversion in combustion systems. It is often applied in order to optimize efficiency and minimize pollutant emissions and depositioning in grate fired boilers through optimizing the distribution of secondary air [13, 14, 15, 16, 17].
Typically when performing a CFD analysis of a grate fired combustion system, the model is split into two steps - the first step is a bed model describing the fuel conversion and release from the grate [18, 19, 20], thereby providing the inlet conditions for the second step; a CFD second combustion stage model.
The accuracy and validity of a CFD analysis of such a large scale facility is very dependent on the application of suitable boundary conditions, and especially modeling of the grate is a serious challenge. [18, 21]
Furthermore the modeling of large scale facilities are often black box models, where no or very little in furnace measurement data are available for validating the model predictions.
This work consists of detailed measurement data and modeling of a bench-scale gas fired combustion facility designed to imitate the conditions in a large scale grate fired combustion facility. The experimental results serves as validation data for CFD models and testing the accuracy of the presently applied industrial CFD approaches.

1.2 Modeling NO formation

The final scope of this work is the modeling of NO formation integrated in a CFD approach. NO is an emission gas that causes acidic rain and in Denmark strict regulations [22] are put on NOx emissions. The term NOx refers to Nitrogen oxides, NO is the most redundant nitrogen oxide emitted from biomass combustion [10].
NO is formed during combustion primarily through conversion of Nitrogen species in the fuel or by high temperature oxidation of N_2 from the combustion air. In grate fired boilers temperatures are relatively low and NO originating from the fuel nitrogen content is the main source of NO [10, 23, 4]. As Table 1.1 shows, the fuel nitrogen content varies significantly for different biomass types and even for the same type of biomass fuels, their chemical content may differ, depending on growing conditions (e.g., the place and the season). As a comparison, the current NO emission limit would only allow approximately 0.05 wt% N to convert to NO.

Fuel	N wt% dry and ash free	reference
Coal	0.76-1.2	[6, 3]
Straw	0.46-0.76	[4, 3]
Waste	0.97-1.45	[4]
Wood	0.10-0.6	[6, 4]

Table 1.1: Typical nitrogen content in coal and biomass.

If NO emission regulations are not met, removal of NO from the flue gas is necessary, by applying expensive flue gas cleaning methods. Often this will make a biomass plant unfeasible. This serves as motivation for minimizing NO formation in the fuel bed and in the second stage combustion, where CFD modeling can serve as a valuable tool. This work focuses on understanding and modeling the NO formation and destruction above the grate.

1.3 References

[1] A. Demirbas. *Prog. Energ. Combust. Sci.*, 30:219–230, 2004.

[2] H.P. Nielsen, F.J. Frandsen, K. Dam-Johansen, and L.L. Baxter. *Prog. Energ. Combust. Sci.*, 26:283–298, 2000.

[3] A. Demirbas. *Prog. Energ. Combust. Sci.*, 31:171–192, 2005.

[4] C. Yin, L.A. Rosendahl, and S.K. Kær. *Prog. Energ. Combust. Sci.*, 34:725–754, 2008.

[5] E.J. Anthony. *Prog. Energ. Combust. Sci.*, 21:239–268, 1995.

[6] M. Sami, K. Annamalai, and M. Wooldridge. *Prog. Energ. Combust. Sci.*, 27:171–214, 2001.

[7] L.L. Baxter. *Fuel*, 84:1295–1302, 2005.

[8] M. Stenseng, A. Jensen, and K. Dam-Johansen. *J. Analyt. Appl. Pyrolysis*, 58-59:765–780, 2001.

[9] F. Tian, J. Yu, L.J. McKenzie, J. Hayashi, and C. Li. *Energy Fuels*, 21:517–521, 2007.

[10] P. Glarborg, A.D. Jensen, and J.E. Johnsson. *Prog. Energy. Combust. Sci.*, 29:89–113, 2003.

[11] K-M. Hansson, J. Samuelsson, C. Tullin, and L-E. Åmand. *Combust. Flame*, 137:265–277, 2004.

[12] R.P. van der Lans, L.T. Pedersen, A. Jensen, P. Glarborg, and K. Dam-Johansen. *Biomass and Bioenergy*, 19:199–208, 2000.

[13] W. Dong and W. Blasiak. *Energ. Conv. Manag.*, 42:1847–1896, 2001.

[14] S. Kær, L.A. Rosendahl, and L.L. Baxter. *Fuel*, 85:833–848, 2006.

[15] W. Blasiak, W.H. Yang, and W. Dong. *J. Energy Inst.*, 79:67–79, 2006.

[16] Y.B. Yang, R. Newman, V. Sharifi, J. Swithenbank, and J Ariss. *Fuel*, 86:129–142, 2007.

[17] C. Yin, L. Rosendahl, S. Kær, S. Clausen, S.L. Hvid, and T. Hille. *Energy Fuels*, 22:1380–1390, 2008.

[18] Y.B. Yang, Y.R. Goh, R. Zakaria, V. Nasserzadeh, and J. Swithenbank. *Waste Management*, 22:369–380, 2002.

[19] S.K. Kær. *Biomass and Bioenergy*, 28:307–320, 2005.

[20] H. Zhou, A.D. Jensen, P. Glarborg, P.A. Jensen, and A. Kavaliauskas. *Fuel*, 84:389–403, 2005.

[21] C. Ryu, D. Shin, and S. Choi. *J. Air Waste Manage. Assoc.*, 52:174–185, 2002.

[22] Danish Ministry of the Environment. Bekendtgørelse om store fyr, BEK nr 808 af 25/09/2003.

[23] G. Stubenberger, R. Scharler, S. Zahirovic, and I. Obernberger. *Fuel*, 87:783–806, 2008.

Chapter 2

Experimental setup

An experimental setup has been constructed to serve as a validation case for CFD modeling, approximating temperature and combustion conditions of the freeboard section of a grate-fired power plant. The setup is illustrated in Figure 2.1. A more detailed description of parts of the setup is found in appendix B along with tabulated experimental data. The setup is an almost 3 meter long cylindrical construction that consists of two major sections; a first-stage reactor and a freeboard section. In the first-stage reactor, flue gas from a substoichiometric natural gas flame is mixed with additional natural gas. This gas mixture simulates the pyrolysis and primary combustion gases emerging from a fuel bed at grate firing conditions. The combustion gases are led through a flow straightener, which can be thought of as an analogy to the surface of the bed layer, and into the freeboard section, where secondary air is added axi-symmetrically to complete the combustion process.

Figure 2.2 describes in detail the geometry of the freeboard section, which has a diameter of 49 cm. The secondary air inlet consists of 210 small holes with a diameter of 2.5 mm positioned in a circle 221 mm from the center axis. The secondary air enters the freeboard section in a 45 degree angle.

Several ports provide access to the reactor for temperature measurements and gas sampling at different positions, as well as visual access for optical measurements. Ammonia addition to the reactor is done to facilitate fuel-NO

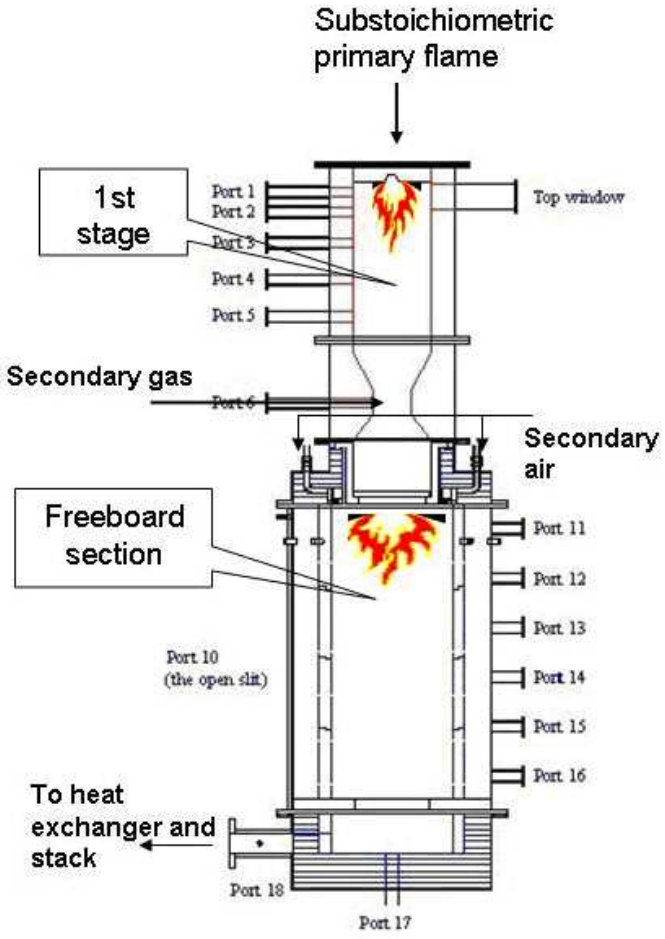

Figure 2.1: Illustration of the experimental setup

formation - the major source of NO_x in solid fuel combustion [1].

Flue gas from a substoichiometric natural gas flame is mixed with additional natural gas. This gas mixture is simulates the pyrolysis and primary combustion gases emerging from a fuel bed at grate firing conditions. The ammonia is added with this secondary natural gas stream. The combustion gases are led through a flow straightener, which can be thought of as an analogy to the surface of the bed layer, and into the freeboard section, where secondary air is added axi-symmetrically to complete the combustion process.

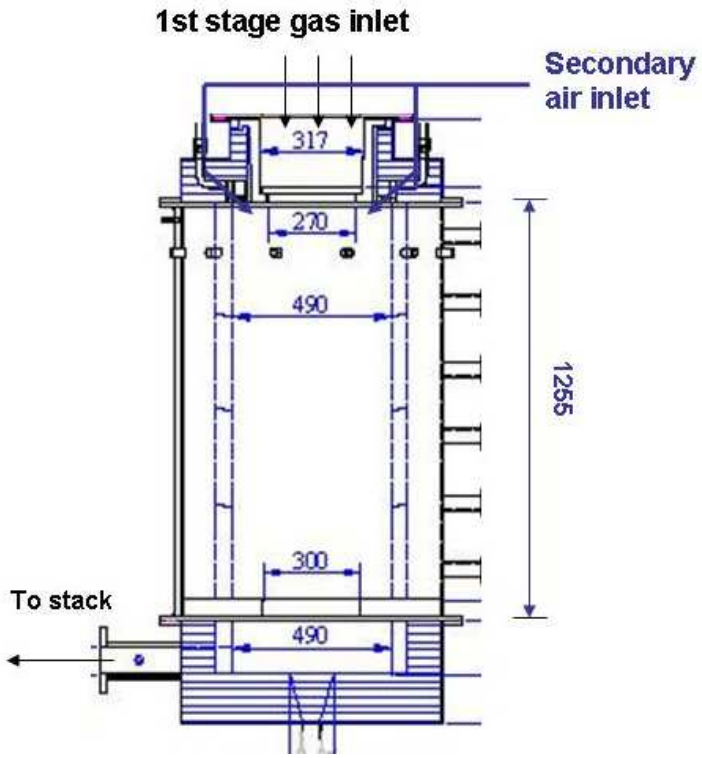

Figure 2.2: Geometry of the freeboard section - all measures in mm.

2.1 Gas analysis

Extractive gas analysis was performed using an oil-cooled probe to quench the sample gas before leading it at 150°C via teflon piping, through a hot filter to an UV based ABB Limas HW NH_3-NO analyzer. After the NH_3 analyzer, the flue gas was quenched, water was condensed, and the gas was led to a Fischer-Rosemount NGA 2000 analyzer to measure CO, CO_2 and O_2 concentrations, and an IR based Fischer-Rosemount NGA 2000 NO analyzer. The measurements were made by inserting the probe to the ports and traversing. A data point was collected after approximately 5 minutes of steady gas concentration measurement. In general the standard deviation on species was less than the analyzer uncertainties (O_2 0.1%, CO_2 0.2%,CO 0.05% and NH_3 and NO 5ppm).

2.1.1 NH_3 sampling

The configuration of the sampling probe is important for a successful quantitative sampling of a combustion gas containing reactive species as CO, NO and especially NH_3. The collection of a sample of hot gas requires the use of a probe preferably as small as possible to minimize the flow disturbance but also to allow as little residence time in the probe as possible. The probe needs to be cooled so that the gas sample is rapidly quenched and no secondary reactions are occurring in the probe or in tubes and filters on the way to the gas analyzers. Danish environmental authorities [2] recommend that sampling of hot gases for determination of emissions is performed at 180 °C. This temperature is low enough to obtain immediate quenching of the combustion gas, but high enough to avoid water condensation, which could absorb ammonia from the sample gas. In the temperature interval 180-230°C formation of ammoniumsulphates may occur through reactions with SO_3, but with natural gas being the only fuel, the sulfur content is assumed to be too low for any ammonium compounds to be formed. Furthermore the gas sample line needs to be of an inert material to avoid catalytic reactions, especially catalytic oxidation of NH_3 is possible on steel surfaces.

Streibel et al.[3] used an air cooled quartz lined lance at 250-300°C to sample ammonia in a waste incineration plant. Åmand et al. [4] used a water cooled steel probe with an inner quartz liner electrically heated to 200°C and a quartz filter at the tip of the probe to analyze ethene and ammonia from a circulating fluidized bed boiler [4]. Kassman et al. [5] made theoretical estimations of the ammonia at the probe tip used by Åmand et al [4]. They found that a catalytically active filter cake and the quartz filter (at approx. 1100 K) along with homogeneous reactions due to slow quenching could lead to a loss of up to 20% of the ammonia [5]. Kasmann et al. also found that saturation of heated teflon tubing with ammonia was occurring, meaning that before a measurement can be obtained, sampling has to be done for some time (approx. 2 hours) to achieve saturation of the sample lines [5].

Based on the recommendations from the literature, a small oil-cooled gas

sampling probe was constructed. The probe, which had an inner quartz tube to avoid catalytic reactions, was kept at a temperature of 180°C. The gas transport from the probe through the heated quartz filter was done using heated teflon tubes. Figure 2.3 sketches the probe and gas sampling configuration.

Unfortunately the ammonia analyzer had some cross sensitivity, especially when measuring in a fuel-rich environment. A quantitative estimate of the NH_3 concentration was obtained by switching on and off the ammonia addition and reporting the difference in measured NH_3 concentration.

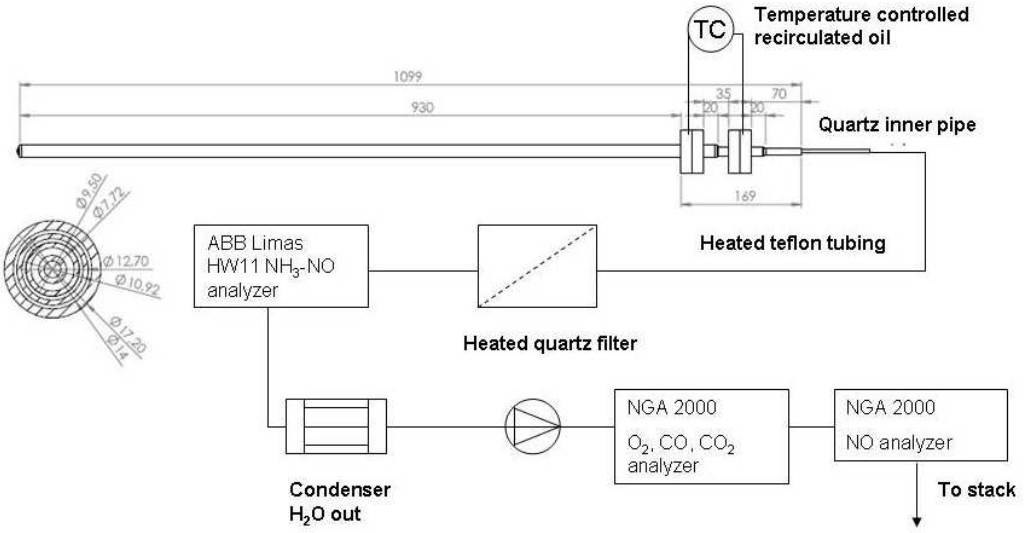

Figure 2.3: Sketch of the gas sampling system

2.2 Temperature measurements

Temperature measurements were performed with a small VDI/VDE 3511 type suction pyrometer. A suction pyrometer was chosen, since measurements with ordinary thermocouples were strongly affected by radiation. The suction pyrometer had an extended ceramic tip of 400 mm, to avoid that the water cooled section of the pyrometer could act as a cooling tube inside

the furnace. A sketch of the pyrometer and its dimensions can be seen in Figure 2.4. The suction rate necessary to achieve steady temperature measurements (unaffected by radiation) was determined to be approximately 2 Nm^3/h. This is approximately 3% of the total flow rate through the setup, and it corresponds to a measurement volume with a diameter of 6 cm.

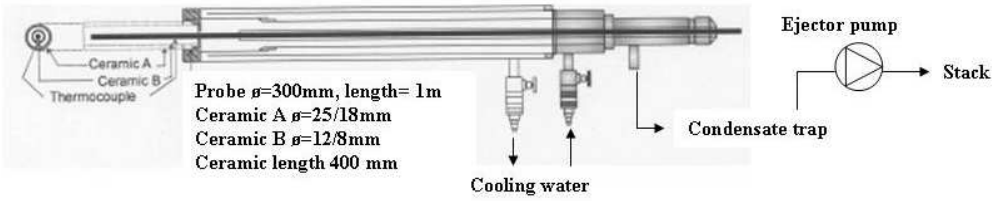

Figure 2.4: Sketch of the suction pyrometer

2.3 Velocity measurements

Laser Doppler Anemometry (LDA) is a technique for measuring gas velocities. The measurements are performed indirectly by measuring the velocity of tracer particles in the fluid flow. The main advantage of the LDA technique is that it is non-intrusive, and therefore well suited for the present purpose. A 4W Dantec Dynamics Argon-ion coherent laser was used during the experiments to obtain the axial velocities. Alumina particles with a mean diameter of 1μm were used as seeding material. Alumina (Al_2O_3) was chosen because it is an inert material that can withstand the high temperatures in the reactor. Small particles are preferred since they will follow the gas flow. Velocity measurements of the axial velocity component were performed in six different positions. Measurements were performed for a time span of 5 minutes in 13 evenly spaced points over the entire cross section of the freeboard section. This gives an increment of 4 cm. The measurement volume (the volume of the intersecting laser beams) had a length in the radial direction of 10.5 mm. Laser measurements were performed through a quartz window mounted in 6

different positions on an open slit port (port 10 on Figure 2.1).

2.4 Boundary conditions

Since only the secondary combustion chamber is intended to serve as a validation case for numerical models, proper boundary conditions need to be applied. An accurate determination of boundary conditions is essential in order to achieve a successful CFD analysis of any system.
Full scale data from Avedøre grate fired combustion facility shows that for a 100% load with straw as fuel, the O_2 concentration in the exhaust is typically 6,6% [6]. The air is staged with 15 kg/s entering as primary air and 20 kg/s as secondary air. By transferring this information to the pilot scale reactor, the following setting was chosen:

- A primary to secondary air ratio of 15/20.
- A total exit dry O2 content of 6,6% dry

Two different settings are analysed and presented within this work. The inlet gas flows and temperatures are summarized in Table 2.1. It is noted that the only difference between the two settings are the secondary air flow; the primary gas flow and its composition are identical for the two settings.

Table 2.1: Boundary conditions: Gas flows and gas temperatures - all volumetric flows are normalized to, 0 °C and 1 atm.

	Setting 1	Setting 2
1st stage air	430 l/min	430 l/min
primary natural gas	46.5 l/min	46.5 Nl/min
secondary natural gas	22.3 l/min	22.3 l/min
Total primary mass flow	10.13 g/s	10.13 g/s
Inlet temperature of primary flow	1027°C	1027°C
Secondary air flow	575 l/min	303 l/min
Secondary air mass flow	12.2 g/s	6.5 g/s
Secondary air temperature	400°C	400°C

In the present case, the natural gas fuel is already partly oxidated. In order to determine the inlet gas phase composition, the secondary air injection was moved further downstream, and the inlet gas mixture composition could

be determined by measuring in the first available measurement port 8 cm into the freeboard section. It was then assumed that the gas composition in this position was identical to the freeboard inlet conditions during ordinary operation of the setup. This is a decent assumption since the fuel-rich gas mixture is not undergoing any dramatic changes or experiencing contact air. This is confirmed by a PFR calculation of the inlet gas mixture at 1300K. Neither the combustibles (CH_4 and CO) or NH_3 undergo significant conversion from entering the setup to contact with the secondary air. The residence time from the secondary gas inlet to the freeboard entrance is approximately 0.5 second.

Table 2.2 displays the average measured gas inlet composition. It was not possible to measure all species, so the inlet concentration of natural gas and water vapor is estimated based on a 1 second plug flow calculation of the 1st stage combustion, while assuming that the added secondary natural gas does not react before entering the freeboard section. Two different sets of boundary inlet flows are applied in the CFD modeling, depending on whether or not the chemical mechanisms include H_2.

The content of NO in the primary gas mixture was measured to approximately 30 ppmv, while the concentration of NH_3 was calculated to be 620 ppmv.

Table 2.2: Measured and calculated boundary condition for the primary gas composition, all concentration indications are volume based.

	CH_4	CO	CO_2	O_2	H_2O	H_2	N_2
Gas measurement	N/A	2.4-2.9 % dry	9.4-10.0 % dry	0 % dry	N/A	N/A	
Calculated based on inlet flows	5.8 %dry	2.2 % dry	9.9 % dry	0 % dry	17.1 %	2.4 % dry	balance
CFD input (no H_2)	6.0 %dry	2.9 %dry	9.9 % dry	0 % dry	18 %	-	balance
CFD input (with H_2)	5.8 %dry	2.2 %dry	9.9 % dry	0 % dry	17.1 %	2.4	balance

Wall temperature measurements

Another boundary condition that was explicitly determined was the wall temperature, which was measured using an Optris CT 2MH 1.6 μ wavelength range Infra Red detector. The measurements were performed through a win-

dow, opposite of a pure wall section. The measurements were averages of 54 mm diameter spots on the opposite wall. The IR thermometer was calibrated using black body cavities at 800°C and 1000°C, and the transmissivity of the furnace window was determined to be 0.88 (12% signal loss through the window). It is noted that the 1.6 μm wavelength range at which the thermometer operates makes it possible to perform measurements through ordinary glass windows.

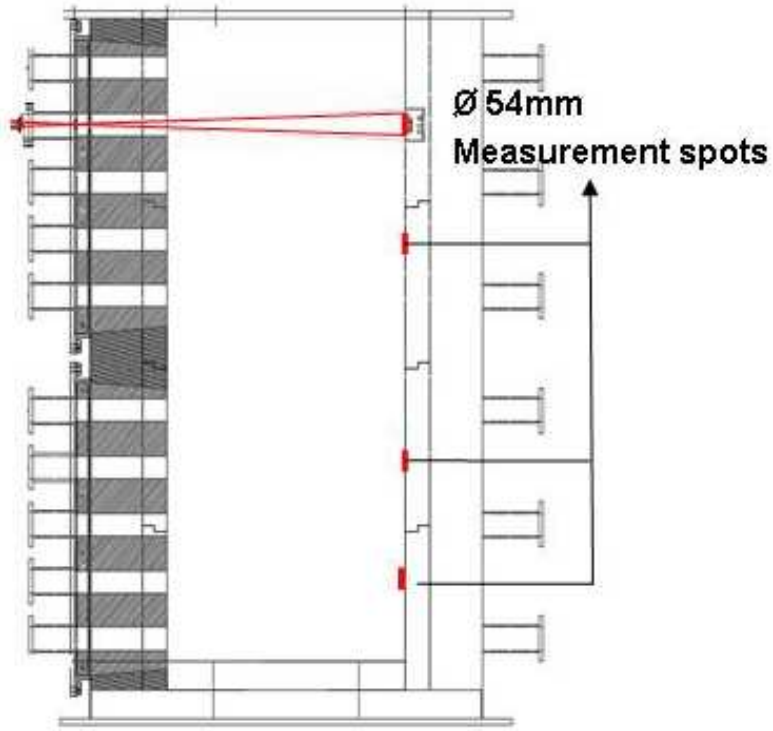

Figure 2.5: Sketch of the IR wall temperature measurement configuration.

The temperature is determined based on the detected Infra Red signal by assuming that the wall emissivity can be set to 1 due to cavity effects of the measurement through a small hole in a surface. The wall temperature measurements are summarized in Table 2.3. Apparently the difference in wall temperature is very small and irregular along the freeboard section, so a constant wall temperature of 967°C and 1077°C is applied in the CFD

computations for setting 1 and 2, respectively. During the CFD calculations the emissivity of the alumina coated walls is assumed to be 0.3 [7].

Table 2.3: Boundary conditions: wall temperatures

	Temperature °C	
position/mm	Setting 1	Setting 2
188	962	1078
388	960	1066
788	975	1090
988	950	1080

2.5 References

[1] P. Glarborg, A.D. Jensen, and J.E. Johnsson. *Prog. Energy. Combust. Sci.*, 29:89–113, 2003.

[2] *Determination of concentrations of ammonia in gas flows*. Metodeblad nr. MEL-24 (in danish) available online 26-04-2009: http://www.ref-lab.dk/cms/site.aspx?p=6727, Force technology, 2007.

[3] T. Streibel, K. Hafner, F. Mühlberger, T. Adam, R. Warnecke, and R. Zimmerman. *Anal. Bioanal. Chem.*, 384:1096–1106, 2006.

[4] L-E Åmand, H. Kassman, M. Karlsson, and B. Leckner. *J. Inst. of Energy*, 70:25–30, 1997.

[5] H. Kassman, L-E Åmand, and B. Leckner. *J. Inst. of Energy*, 70:95–101, 1997.

[6] C. Yin, L. Rosendahl, S. Kær, S. Clausen, S.L. Hvid, and T. Hille. *Energy Fuels*, 22:1380–1390, 2008.

[7] R.B. Bird and W.E. Stewart and E.N. Lightfoot. *Transport Phenomena, 2nd edition*. John Wiley and Sons Inc., 2002.

Chapter 3

CFD modeling basics

CFD is an abbreviation for Computational Fluid Dynamics, CFD modeling is used in numerous applications, from aerospace modeling to food processing and power production. What CFD modeling basically can do is to predict the flow of fluid and heat through a computational domain. This is done by solving the governing transport equations [1]:

$$\frac{\partial \rho}{\partial t} + (\nabla \cdot \rho \mathbf{v}) = S_m \tag{3.1}$$

Equation (3.1) is the equation of continuity and it is developed by writing a mass balance over a volume element. In equation (3.1) ρ is the fluid density, t is time, and $\mathbf{v}$ is a direction velocity vector. ρ $\mathbf{v}$ is the mass flux, and its divergence symbolized with $\nabla \cdot \rho$ $\mathbf{v}$ can be considered as the net rate of mass efflux per unit volume. S_m is a source term, which for instance could appear from vaporization from a dispersed phase [2].

$$\frac{\partial}{\partial t}(\rho \mathbf{v}) = -\nabla \cdot (\rho \mathbf{v}\mathbf{v}) - \nabla p + \nabla \overline{\overline{\tau}} \tag{3.2}$$

Momentum acceleration = convection + molecular transport (pressure term + viscous term)

The equation of motion also known as the Navier-Stokes equation is displayed in equation (3.2), it can be derived by doing a momentum balance over a vol-

ume element [2]. In equation (3.2) the left side represents the rate of increase of momentum per unit volume. the first expression on the right side of the equal sign represents the rate of momentum addition by convection per unit volume. The last two expressions represent the rate of momentum addition by molecular transport due to pressure and viscous forces respectively, with $\overline{\overline{\tau}}$ being the viscous stress tensor. Gravitational and external forces has been left out of equation (3.2)

$$\overline{\overline{\tau}} = \mu[\nabla \mathbf{v} + \nabla \mathbf{v}^T - \frac{2}{3}\nabla \cdot \mathbf{v}\overline{\overline{I}}] \tag{3.3}$$

The viscous stress tensor can be expressed as in equation (3.3), with μ being the molecular viscosity and $\overline{\overline{I}}$ is the unit tensor and the second term on the right hand side is the effect of volume expansion.[1, CHAPTER 9]
The equations (3.2) and (3.3) express the motion of fluid, equation (3.4) states the motion of heat:

$$\frac{\partial}{\partial t}(\rho E) + \nabla \cdot (\mathbf{v}(\rho E + p)) = \nabla \cdot \left(k_{eff}\nabla T - \sum_j h_j \mathbf{J}_j + (\overline{\overline{\tau}} \cdot \mathbf{v})\right) + S_h \tag{3.4}$$

Transient term + Convection = Conduction + Species Diffusion + Viscous Dissipation + External Heat source

The first term on the left side expresses the rate of increase in energy per unit volume, and the second term addresses the energy increase due to convective transport and compression. k_{eff} is the effective conductivity $(k + k_t)$, where k_t is the turbulent thermal conductivity, defined according to the turbulence model being used (see chapter 3.2), $\mathbf{J}_j$ is the diffusion flux of species j and h_j is the species enthalpy. The first three terms on the right-hand side of equation (3.4) represent energy transfer due to conduction, species diffusion, and viscous dissipation, respectively. S_h represents an external heat source, which for instance could be the heat released from a chemical reaction, when enabling radiation models (see chapter 3.3) S_h includes a radiation term.

[1, 2]
Basically equations (3.1)-(3.4) are the equations that needs to be solved to describe motion and heat transfer in a fluid flow. However if the CFD analysis is to have any meaning modeling reacting flows the transport of individual fluid species need to be taken into consideration [1, CHAPTER 12]:

$$\frac{\partial}{\partial t}(\rho Y_i) + \nabla \cdot (\rho \mathbf{v} Y_i) = -\nabla \cdot \mathbf{J}_i + R_i + S_i \tag{3.5}$$

Transient term + Convection = Species Diffusion + Chemical reaction + External production

In equation (3.5) Y_i is the individual species mass fraction, R_i represents the production (or consumption) of species due to chemical reaction and S_i is an additional source term for species production for instance from vaporization [1, CHAPTER 14].

3.1 Solution methods

The computational domain is often described using a Finite Volume Method (FVM), which means that the domain is divided into minor control volumes, or cells. The transport equations, which are partial differential equations (3.1)-(3.5) are then assigned to each cell and solved using a discretization method, where the partial differential equations are rewritten to algebraic equations using an integral derivation method. These algebraic equations are then solved to predict mass, momentum and energy transport at discrete points in the computational domain.[3]
The solution procedures in solving the discretization equations can be divided into two main categories, relating to whether the compressible or incompressible form of the equation of motion is being solved.
The compressible form solution procedure is also referred to as density-based solvers because a direct coupling between pressure and density can be formulated through the equation of state (the ideal gas law at ideal gas conditions).

Solving the incompressible form of the equation of motion uses a different strategy since there no longer exists a coupling between pressure and fluid density. Mathematical manipulations of the continuity and momentum equations are then used to derive an additional relationship for the pressure, for instance a Poisson type equation for the pressure correction can be applied. Solvers using this approach are referred to as segregated or pressure based solvers.

The solution procedure described above is the approach used in the commercial FVM based CFD tool FLUENT, which is the CFD program that is used during this project.

Basically how the discretization works in FLUENT can be understood by observing the change of the integral equation expressing the steady-state conservation equation for transport of a scalar quantity ϕ, written in integral form over an arbitrary control volume [1, CHAPTER26]:

$$\oint \rho\phi\mathbf{v}d\mathbf{A} = \oint \Gamma_\phi \nabla\phi \cdot d\mathbf{A} + \oint_V S_\phi \tag{3.6}$$

In equation (3.6) $\mathbf{A}$ is an area vector, Γ_ϕ is the diffusion coefficient of the scalar and S_ϕ is the source term per unit volume. Equation (3.6) takes on expresses the general forms of transport: convection=diffusion+source term. Equation (3.6) is applied over each cell in FLUENT and discretized as follows:

$$\sum_f^{Nfaces} \rho_f\phi_f\mathbf{v}_f\mathbf{A}_f = \sum_f^{Nfaces} \Gamma_\phi(\nabla\phi)_n \cdot \mathbf{A}_f + S_\phi V \tag{3.7}$$

In equation (3.7) f relates to each face of the cell faces, A_f is the area of each face and $\rho_f\phi_f\mathbf{v}_f\mathbf{A}_f$ expresses the mass flux through each cell. By default, FLUENT stores discrete values of the scalar at the cell centers. However, face values are required for the convection terms in Equation (3.7) and must be interpolated from the cell center values. This is accomplished using an interpolation scheme (for instance first order upwind or second order upwind for convection). Finally a linearization of the discretized equations over the

entire computational domain is done and the resultant linear equation system is solved to yield updated values of the dependent variables. The method of linearization can either be segregated or coupled:
The segregated approach solves for a single variable field sequentially (e.g. p) by considering all cells at the same time. It then solves for the next variable field by again considering all cells at the same time, and so on.

The coupled solver solves the governing equations of continuity, momentum, energy and species transport simultaneously (i.e., coupled together).
Implicit coupled solver: For a given variable, the unknown value in each cell is computed using a relation that includes both existing and unknown values from neighboring cells. Therefore each unknown will appear in more than one equation in the system, and these equations must be solved simultaneously to give the unknown quantities.
Explicit coupled solver: For a given variable, the unknown value in each cell is computed using a relation that includes only existing values. Therefore each unknown will appear in only one equation in the system and the equations for the unknown value in each cell can be solved one at a time to give the unknown quantities [1].

So to summarize how the solution procedure in FLUENT:

- The computational domain is divided into discrete control volumes (cells)

- Integration of the governing equations on the individual control volumes to construct algebraic equations for the discrete dependent variables such as velocities, pressure, temperature, and conserved scalars.

- Linearization of the discretized equations and solution of the resultant linear equation system to yield updated values of the dependent variables.

Other CFD tools rely on different solution procedures such as the Finite Element Method (FEM). Generally, FEM discretizes the partial differential transport equations using calculus of variations or method-of-weighted-residuals approaches. [3] FEM analysis is often used in structural mechanics (i.e. solving for deformation and stresses in solid bodies or dynamics of structures) while computational fluid dynamics tends to use FVM methods, since CFD problems usually require discretization of the problem into a large number of cells/gridpoints (millions or more), therefore cost of the solution favors simpler, lower order approximation within each cell.

3.2 Modeling turbulence

Aside from solving the transport equations described in chapter 3 all commercial CFD codes are equipped with different sub-models, making the code able to handle various flow problems such as turbulence, radiation, chemical reactions and multiphase flows.

Turbulent flows are characterized by having the fluid velocities fluctuating in an apparently random fashion, in contrast to laminar flows which tend to be steady or be fluctuating in a periodic fashion.

Turbulence in fluid flows is also observed as large and small eddies or vortices, which can transport quantities such as energy, momentum, and especially important for combustion science; individual fluid species. The fluctuating velocities cause the transported quantities to fluctuate as well. [1, CHAPTER 11]

Turbulence arises when the inertial forces governing the fluid motion exceed the damping effect induced by the fluid viscosity. This means that fluids with higher viscosity (i.e. liquids) will require higher velocities before turbulence takes effect, than low viscosity fluids such as gases. This viscosity dependent onset of turbulent motion also appears in the definition of the Reynolds

number, which describes the relationship between inertial and viscous forces:

$$Re = \frac{Inertial\ forces}{Viscous\ forces} = \frac{v\rho D}{\mu} \quad (for\ pipe\ flow) \tag{3.8}$$

If the dimensionless Reynolds number exceeds a certain critical value turbulent motion will start, for fluid flow in a pipe this value is around 2000.

Turbulent flows are referred to as dissipative; meaning that kinetic energy from the fluid motion is converted into turbulent kinetic energy, which results in the formation of large eddies. These large eddies are then eventually broken down into smaller eddies which results in generation of heat through viscous dissipation.
The length scale in which the large turbulent eddies are formed is denoted l_0 and is determined by the fluid inertia and the size and nature of the surrounding geometry. The main part of the heat generation occurs from dissipation of the smallest eddies, whose size is limited by the Kolmogorov length scale, l_K. The ratio between the smallest and largest eddy length scales is related to the Reynolds number as:

$$\frac{l_0}{l_K} = Re^{3/4} \tag{3.9}$$

The relationship in equation (3.9) indicate that at turbulent Reynolds numbers the size difference of the turbulent eddies can be several orders of magnitude.

3.2.1 Mathematical description of turbulence

The fluctuations induced by turbulent flow are usually modeled by dividing the instantaneous properties of a scalar in the conservation equation into mean and fluctuating components:

$$\phi = \overline{\phi} + \phi' \tag{3.10}$$

In equation (3.10) ϕ describes any conserved scalar variable, $\overline{\phi}$ represents its ensemble average and ϕ' is the deviation from average.

The substitution of the averaged scalars into the equations of continuity (3.1) and momentum (3.2) gives the following expressions:

$$\frac{\partial \rho}{\partial t} + \frac{\partial}{\partial x_i}(\rho \cdot \overline{v_i}) = 0 \tag{3.11}$$

$$\frac{\partial}{\partial t}(\rho \cdot \overline{v_i}) + \frac{\partial}{\partial x_j}(\rho \cdot \overline{v_i} \cdot \overline{v_j}) = -\frac{\partial \overline{p}}{\partial x_i} + \frac{\partial}{\partial x_j}(\partial \overline{\tau_{ij}} - \rho \overline{v_i' v_j'}) \tag{3.12}$$

In equation (3.12) subscripts i and j refers to the directions 1,2,3, and x is the direction variable. Equations (3.11) and (3.12) are called Reynolds Averaged Navier Stokes (RANS) equations. Comparing equation (3.11) and (3.12) to the standard Navier Stokes equations (equations (3.1) and (3.2)) extra terms appear due to the effect of turbulence:

$$-\rho \overline{v_i' v_j'}$$

These extra terms are designated Reynolds stress terms, and the modeling of these terms is known as the turbulence closure problem, which is a major challenge in computational fluid dynamics turbulence modeling. [3, 1]

3.2.2 Turbulence models

A wide variety of turbulence models are offered in FLUENT. The models can be divided into two major parts; RANS based models, which rely on ensemble averaging of the fluctuating variables, and Large Eddy Simulation models that partly use direct numerical simulation to describe the turbulent motion. The RANS based models consist of a group of 1 (Spalart Almares) and 2 (standard k-ϵ, RNG k-ϵ, Realizable k-ϵ, Standard k-ω and SST k-ω) equation models. All are based on the Boussinesq hypothesis [4], which relates the Reynolds stresses to the mean velocity gradients by introducing a turbulent viscosity. The most complex RANS based model, the Reynolds Stress Model (RSM) solves transport equations for each of the terms in the Reynolds-stress tensor along with the a transport equation for the dissipation rate making it a 5 equation model in 2D and a 7 equation model in 3D.

In combustion applications the RSM model are reported to outperform the lower equation models especially under strongly swirling conditions. [5, 6, 7, 8] In non swirling flames the advantage of the RSM is less pronounced [9, 10]. In industrial combustion applications a k-ϵ type model is often applied. Especially the standard k-ϵ model is popular due to its robustness [1].

3.3 Modeling radiation

Heat can be transferred by either convection, diffusion or radiation. Heat transfer by convection and diffusion is included in the governing equation describing the heat transport (equation (3.4)). However transport through radiation needs to be added as a source term in equation (3.4). In many CFD applications radiative heat transfer is not important, but in systems where the temperature can be quite high as in various combustors, radiative heat transfer can become the dominating source of heat transport. Since the rate of chemical reaction (especially thermal NO formation) can be very sensitive to temperature fluctuations, it is important when modeling combustion to calculate the temperature distribution in the computational domain accurately.

Radiation is basically an electromagnetic mechanism that allows heat to be transfered with the speed of light through regions of space that are devoid of matter. [2] In radiative heat transfer the focus is on describing absorption, emission and scattering of radiant energy in a participating gray medium.
The radiative transfer equation describes these effects at position $\vec{r}$ in the direction $\vec{s}$:[1, CHAPTER 12]

$$\frac{dI(\vec{r}\vec{s})}{ds} + (a+\sigma_s)I(\vec{r}\vec{s}) = an^2\frac{\sigma T^4}{\pi} + \frac{\sigma}{4\pi}\int_0^{4\pi} I(\vec{r}\vec{s})\Phi(\vec{s}\vec{s}')d\Omega' \qquad (3.13)$$

In equation (3.13) $\vec{s}'$ is a scattering direction vector, s is the path length, a is the medium absorption coefficient, n is the refractive index which is the factor by which the phase velocity of electromagnetic radiation is slowed in

a given material, σ_s is a scattering coefficient, σ is the Stefan-Boltzmann constant, I is the radiation intensity, Φ is a phase function and Ω' a solid angle.
The accuracy of the solution of the radiative heat transfer is highly dependent on accurate knowledge about the radiative properties of both combustion product gases and entrained particles such as coal or soot.
In gases radiation is absorbed and emitted only at the discrete frequencies at which electrons become excited. [3] The main radiative interaction in combustion processes come from H_2O, CO and CO_2.
NO_X and SO_X are also strong radiation absorbers and emitters, but their concentrations are usually so small that the effect can be neglected.

3.4 Radiation modeling in CFD

FLUENT provide five different radiation models:

- Discrete transfer radiation model (DTRM)
- P-1 Radiation model
- Rosseland radiation model
- Surface-to-surface radiation model (S2S)
- Discrete ordinates radiation model (DO)

3.5 Radiation models - discussion

Of the five different radiation models provided by FLUENT the P1 and DO models are the more applicable models when describing gas phase combustion processes. No model in FLUENT by default takes into consideration the discrete wavenumbers at which gas phase species are reported to absorb radiative waves - although it is possible to implement non-gray radiation in the DO model. Instead the gaseous radiant absorption can be estimated based

on a weighted sum of gray gases model (WSGGM) [11], which estimate the gray gas absorption based on mixture composition and temperature. This approach is reported to be a good simplification of the gas mixture emissivity [12].

The work by Ilbas [13] modeling a non-premixed hydrogen-methane flame in FLUENT applying three different radiative settings (No radiation model / P1 / DTRM) showed that both radiation models caused the temperature predictions to comply with measurements, but without radiation models enabled temperature predictions could be overestimated dramatically. An accurate description of the temperature distribution was found to be essential in order to model NO formation. [13]

Wang and coworkers [14] performed a very detailed study describing both effects of soot particles and non-gray gas radiative effects from a propane fueled, oxygen enriched, turbulent, non-premixed, jet flame. Two P1 based radiation modeled was applied, one being similar to the FLUENT application, the other one (p1-FSK) also capable of describing non-gray characteristics of the medium. The results show that soot radiation decrease the flame temperature and thereby NO_X emission substantially, and that non-gray gas effects are important even in a sooting environment.[14]

Habibi et al. [15] compared radiation models in modeling of a steam cracking furnace, and found that the P-1 and DO models gave acceptable results and outperformed the Rosseland model [15].

3.6 References

[1] Fluent inc., Centerra Resource Park, 10 Cavendish Court, Lebanon, NH 03766. *Fluent 6.2 users guide*, 2005.

[2] R.B. Bird and W.E. Stewart and E.N. Lightfoot. *Transport Phenomena, 2nd edition*. John Wiley and Sons Inc., 2002.

[3] A.M. Eaton, L.D. Smoot, S.C. Hill, and C.N. Eatough. *Prog. Energy Combust. Sci.*, 25:387–436, 1999.

[4] J.O. Hinze. *Turbulence*. McGraw-Hill Publishing Co., 1975.

[5] A. Ridluan, S. Eiamsa-ard, and P. Promvonge. *Int. Com. Heat Mass Transf.*, 34:860–869, 2007.

[6] A.E. German and T. Mahmud. *Fuel*, 84:583–594, 2005.

[7] J.L. Xia, G. Yadigaroglu, Y.S. Liu, J. Schmidli, and B.L. Smith. *Int. J. Heat Mass Transf.*, 41:1485–1491, 1998.

[8] F. Breussin, F. Pigari, and R. Weber. *Proc. Combust. Inst.*, 26:211–217, 1996.

[9] H. Knaus, S. Richter, S. Unterberger, U. Schnell, H. Maier, and K.R.G. Hein. *Exp. Therm. Fluid Sci.*, 21:99–108, 2000.

[10] F. Tabet-Helal, B. Sarh, A. Menou, and I. Gökalp. *Combust. Sci. Technol.*, 178:1887–1909, 2006.

[11] T.F. Smith, Z.F. Shen, and J. N. Friedman. *J. Heat Transfer*, 104:602–608, 1982.

[12] N. Lallemant, A. Sayret, and R. Weber. *Prog. Energy Combust. Sci.*, 22:543–574, 1996.

[13] M. Ilbas. *International Journal of Hydrogen Energy*, 30:1113–1126, 2005.

[14] L. Wang, D.C. Haworth, S.R. Turns, and M.F. Modest. *Combust Flame*, 141:170–179, 2005.

[15] A. Habibi, B. Merci, and G.J. Heynderickx. *Computers and Chemical Engineering*, 31:1389–1406, 2007.

Chapter 4

CFD and combustion chemistry

The most simple way of handling combustion modeling in CFD is to treat the reaction terms that appear as source terms in the individual species transport equations (see equation (3.5)) as Arrhenius expressions:

$$k_{forward} = A_r \cdot T^{\beta_r} \cdot e^{-E_r/RT} \tag{4.1}$$

In equation (4.1) A_r is the pre-exponential Arrhenius factor, β_r is a dimensionless temperature exponent, E_r is the activation energy for the reaction and R is the universal gas constant. The reverse rate constant can be found by finding the equilibrium constant, K_r through the thermodynamic properties of the reactants and products, and then use the relationship that the ratio between the forward and reverse reaction equal K_r:

$$k_{reverse} = \frac{k_{forward}}{K_r} \tag{4.2}$$

In FLUENT the laminar finite rate model uses the approach described above. However for most practical combustion systems, the turbulent mixing causes the rate limiting step in destruction of the combustion participants.

4.1 The eddy dissipation model

In order to account for the rate limiting effect of mixing processes, Magnussen and Hjertager [1] developed a combustion model (based on the eddy break-up model presented by Spalding [2]) that accounted for the turbulent mixing of fuel and products. This eddy dissipation model assumes that the chemical reaction rate is governed by the large-eddy mixing time scale $\frac{k}{\epsilon}$: [3, CHAPTER 14]

$$R_{i,r} = \nu'_{i,r} M_{w,i} A \rho \frac{\epsilon}{k} \underbrace{min}_{R} \left(\frac{Y_R}{\nu'_{R,r} M_{w,R}} \right) \tag{4.3}$$

In equation (4.3) $R_{i,r}$ is the rate of production of species i due to reaction r, $\nu'_{i,r}$ is the stoichiometric coefficient, M_w denotes the molar weight of either species i, or reactant R. A is an empirical constant (=4,0) and Y_R is the mass fraction of the particular reactant R. The expression $\underbrace{min}_{R}$ means that the rate is determined from whatever reactant that causes the minimum reaction rate, either oxygen or fuel.

Magnussen and Hjertager [1] also formulated a second expression describing the dissipation of eddies containing hot products. The theory here is that the dissipation of hot product eddies is necessary in order to release the energy that ensures that eddies containing fuel and oxidiser can react:

$$R_{i,r} = \nu'_{i,r} M_{w,i} A B \rho \frac{\epsilon}{k} \left(\frac{\sum_P Y_P}{\sum_j^N \nu''_{j,r} M_{w,j}} \right) \tag{4.4}$$

In equation (4.4) B is an empirical constant and P denotes any product species.

One problem when applying the Eddy Dissipation model is that the temperature is not included anywhere, which actually means that combustion proceeds whenever turbulence is present. This can give some problems) and therefore FLUENT provides an Eddy Dissipation / Finite Rate model. This model evaluates both the rate of turbulent mixing and the Arrhenius rate of reaction, and uses the minimum value. [3, CHAPTER 14]

The Eddy Dissipation model is one of the more popular models to describe turbulence-chemistry although it has some weaknesses. In the eddy-dissipation model every reaction has the same turbulent rate, and therefore the model should be used only for one, or two-step global reactions. The model cannot predict kinetically controlled species such as radicals. [4]

4.2 The Eddy Dissipation Concept

For more detailed reaction mechanisms FLUENT offers the Eddy Dissipation Concept (EDC) model, which is an extension of the Eddy Dissipation model based on the work by Gran and Magnusson [5]. In the EDC model chemical reactions are assumed to occur in the fine structures of the computational cells. These small scale structures can be pictured as a part of the cell, where Kolmogorov sized eddies containing combustion species are situated so close together, that mixing on the molecular level is taking place as illustrated in figure 4.1.

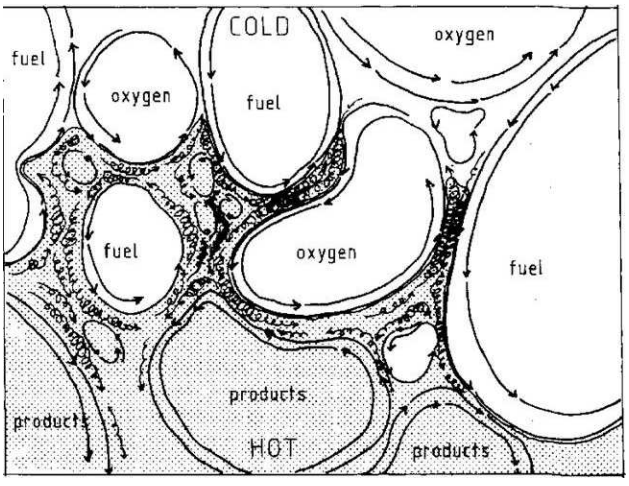

Figure 4.1: This figure illustrates the areas of great mixing between the large scale eddies. It is these areas that are evaluated and modeled as ideal reactors in the EDC model.[6]

The volume fraction of these fine scales is modeled in FLUENT as: [3, CHAPTER 14]

$$\gamma^3 = C_\gamma^3 (\frac{\nu\overline{\epsilon}}{\overline{k}^2})^{3/4} \tag{4.5}$$

ν is the kinematic viscosity and C_γ is a volume fraction constant (2,1377). The time scale for which the chemical reactions occur, τ^*, is found by (4.6).

$$\tau^* = C_\tau (\frac{\nu}{\overline{\epsilon}})^{1/2} = C_{\tau^*} t_K \tag{4.6}$$

In (4.6) C_τ is a model constant (=0,4082) and t_K is the Kolmogorov time scale. In FLUENT, combustion in the fine scales of the computational cells is assumed to occur as a constant pressure reactor, with initial conditions taken as the current species and temperature in the cell. Reactions proceed over the time scale, τ^*. The source term in the conservation equation for the mean species i, is modeled as:

$$\omega_i = \frac{\rho\gamma^2}{1-\gamma^3} \frac{(Y_i^* - Y_{i,init})}{\tau^*} \tag{4.7}$$

Where $Y_{i,init}$ and Y_i^* is the fine scale species mass fraction before and after the reaction. The mass fraction after reaction is found using the Arrhenius expressions for the relevant reactions.
The EDC model is computationally expensive, which limits its use in practical systems. [3, CHAPTER 14]

4.3 Mixture fraction approach

Several turbulence-chemistry submodels in FLUENT are based on the mixture fraction approach. The basic idea of this approach is to separate fluid dynamics and chemistry by introducing a chemistry-independent conserved

scalar; the mixture fraction, f. The mixture fraction approach is only applicable for non-premixed combustion, where a fuel and an oxidizer inlet is defined:

$$f = \frac{Z_i - Z_{i,ox}}{Z_{i,fuel} - Z_{i,ox}} \tag{4.8}$$

Where Z_i is the elemental mass fraction for element, i. The subscript ox denotes the value at the oxidizer stream inlet and the subscript fuel denotes the value at the fuel stream inlet.
Under the assumption of equal diffusivities, the species equations can be reduced to a single equation for the mixture fraction. While the assumption of equal diffusivities is problematic for laminar flows, it is generally acceptable for turbulent flows where turbulent convection overwhelms molecular diffusion. The Favre mean (density-averaged) mixture fraction, $\overline{f}$, equation is: [3, CHAPTER 15]

$$\frac{\partial}{\partial t}(\rho\overline{f}) + \nabla \cdot (\rho \mathbf{v}\overline{f}) = \nabla \cdot (\frac{\mu_t}{Sc_t}\nabla\overline{f}) \tag{4.9}$$

Where μ_t it the turbulent viscosity, $\overline{v}$ is the overall velocity vector and Sc_t is the turbulent Schmidt number:

$$Sc_t = \frac{\mu_t}{\rho D_t} \tag{4.10}$$

Under the assumption of chemical equilibrium, all thermochemical scalars (species fractions, density, and temperature) are uniquely related to the mixture fraction.

4.3.1 Probability Density Functions

In order to obtain averaged values of fluctuating scalars such as temperature, species fractions and density from the instantaneous values obtained through the mixture fraction dependence, FLUENT uses Probability Density Functions (PDFs). How the averaged values are related to the instantaneous

values depends on the turbulence-chemistry interaction model. The Probability Density Function, $p(f)$, can be thought of as the fraction of time that the fluid spends in the vicinity of the state f. Figure 4.2 plots the time trace of mixture fraction at a point in the flow (right-hand side) and the probability density function of f (left-hand side).

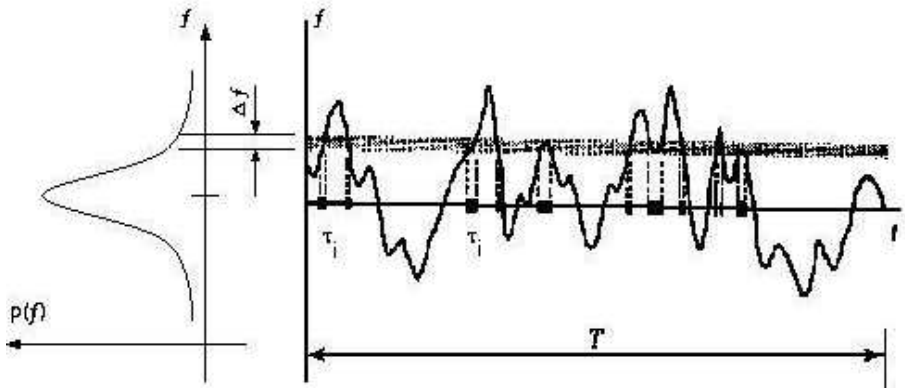

Figure 4.2: Graphical description of the Probability Density Function. [3]

The shape of the function depends on the nature of the turbulent fluctuations in $p(f)$. In practice, $p(f)$ is unknown and is modeled as a mathematical function that approximates the actual PDF shapes that have been observed experimentally. In FLUENT two types of PDF shapes can be computed using either the double delta function or the β function. The double-delta function is the most easily computed, while the β-function most closely represents experimentally observed PDFs. These functions and therefore the shape of the PDF depends solely on the mean mixture fraction $\overline{f}$ and its variance $\overline{f'^2}$, a transport equation for this variance is also modeled similar to the mean value (see equation(4.8)). [3, CHAPTER 15]

4.3.2 Chemistry tabulation

For an equilibrium, adiabatic, single-mixture-fraction case, the mean temperature, density, and species fraction are functions of the $\overline{f}$ and $\overline{f'^2}$ only. Significant computational time can be saved by computing these integrals

once, storing them in a look-up table, and retrieving them during the simulation.
An extension to this chemistry tabulation is the ISAT algorithm (In Situ Adaptive Tabulation) which initially, during simulations, builds the tables for quick accessing later on. The advantage of this approach is that it only builds up tables for the relevant regions of the composition space. The ISAT algorithm is intended for use with the composition PDF transport, EDC and Laminar Finite rate combustion models. [3, CHAPTER 15,18]

4.4 Non-premixed equilibrium modeling

Based on the transport of the introduced scalar, the mixture fraction and its variance, a chemical equilibrium model can be applied. By assuming chemical equilibrium and adiabatic conditions[1] all species fractions, density and temperature is related to the mixture fraction values. Equations for individual species does therefore not need to be solved, instead, species concentrations are derived from the predicted mixture fraction fields. Interactions between turbulence and chemistry is accounted for using a PDF. The thermochemistry calculations are preprocessed and tabulated for look up.
The non-premixed equilibrium model allows intermediate (radical) species prediction, dissociation effects, and rigorous turbulence-chemistry coupling. The method is computationally efficient in that it does not require the solution of a large number of species transport equations.
However some general assumptions need to be valid in order for the non-premixed equilibrium combustion model to be applicable:

- The chemical system must be of the diffusion type with discrete fuel and oxidizer inlets.

- The Lewis number must be unity. (This implies that the diffusion

[1] FLUENT offers a non-adiabatic extension model to account for heat transfer through wall boundaries, droplets, and/or particles.[3, CHAPTER 15]

coefficients for all species and enthalpy are equal, a good approximation in turbulent flow).

- The flow must be turbulent.
- The chemistry is assumed infinitely fast. (This is not the case for soot formation, NO_X chemistry and low temperature CO oxidation)[3, 7]

4.5 Laminar Flamelet modeling

The laminar Flamelet approach models a turbulent flame as an ensemble of laminar flamelets. The laminar flamelet model is suited to predict moderate chemical non-equilibrium in turbulent flames due to aerodynamic straining by the turbulence. The advantage of the laminar flamelet approach is that realistic chemical kinetic effects can be incorporated into turbulent flames. The chemistry can then be preprocessed and tabulated, offering tremendous computational savings. However, the laminar flamelet model is limited to modeling combustion with relatively fast chemistry. The flame is assumed to respond instantaneously to the aerodynamic strain, and thus the model cannot capture deep non-equilibrium effects such as ignition, extinction, and slow chemistry (like NO_X).[3, CHAPTER 15]
The laminar flamelet concept deviates from the equilibrium model by introducing a scalar dissipation rate. The scalar dissipation, χ is defined as:

$$\chi = 2D \left|\nabla f\right|^2 \tag{4.11}$$

In equation (4.11) D is a representative diffusion. The scalar dissipation rate can be regarded as a diffusivity in mixture fraction space, a strain rate of 0 equals the equilibrium condition. In FLUENT the scalar quantity transported is the stoichiometric dissipation rate χ_{st}, which is found through (4.12):

$$\chi_{st} = \frac{C_\chi \epsilon \overline{f'}^2}{k} \tag{4.12}$$

Where C_χ is a constant (=2 by default). Mean species mass fractions and temperature in the turbulent flame can be determined from the PDF of χ_{st} and f expressed in general as:

$$\overline{\phi} = \int \int \phi(f, \chi_{st}) p(f, \chi_{st}) df d\chi_{st} \tag{4.13}$$

where ϕ represents species mass fractions and temperature. χ_{st} and f are assumed to be statistically independent, so the joint PDF p(χ_{st},f) can be simplified as p(χ_{st}) p(f). The tabulated field which is stored (see chapter 4.3.2) will then have a three dimensional structure.
For non-adiabatic laminar flamelets, the additional parameter of enthalpy is required. However, the computational cost of modeling flamelets over a range of enthalpies is prohibitive, so in FLUENT some approximations are made. For more information see [3, CHAPTER 15].
In FLUENT flamelets can be generated, or imported flamelet files calculated with other stand-alone packages.

4.6 Composite PDF model

FLUENT also offers a composite PDF model intended for modeling finite rate kinetic effects in turbulent reacting flows.
An alternative to Reynolds-averaging the species and energy equations is to derive a transport equation for their single-point, joint probability density function (PDF). This PDF, denoted by P, can be considered to be proportional to the fraction of the time that the fluid spends at each species composition and temperature state. The evolution of the composition probability function (PDF) can be described by a transport equation derived rigorously from the Navier-Stokes equations as:

$$\frac{\partial}{\partial t}(\rho P)+\frac{\partial}{\partial x_i}(\rho v_i P)\frac{\partial}{\partial \psi_k}(\rho S_k P) = -\frac{\partial}{\partial x_i}[\rho \langle v_i" \mid \psi\rangle P]+\frac{\partial}{\partial \psi_k}[\rho \left\langle \frac{1}{\rho}\frac{\partial J_{i,k}}{\partial x_i} \mid \psi \right\rangle P] \tag{4.14}$$

In equation (4.14) P is the favre joint probability density function, which have N+1 dimensions for N species and temperature states. v is the Favre mean fluid velocity vector and v_i" is the fluctuation vector, S_k is the reaction rate for species k, $J_{i,k}$ is the molecular diffusion flux vector for species k in direction i. The notation $\langle \ldots \rangle$ denotes expectations and $\langle A \mid B \rangle$ is the conditional probability of event A, given the event B occurs.

In equation (4.14) the terms on the left-hand side are closed, while those on the right-hand side are not and require modeling. The first term on the left-hand side is the unsteady rate of change of the PDF, the second term is the change of the PDF due to convection by the mean velocity field, and the third term is the change due to chemical reactions. The two terms on the right-hand side represent the PDF change due to scalar convection by turbulence (turbulent scalar flux), and molecular mixing/diffusion, respectively. The principal strength of the PDF transport approach is that the highly-nonlinear reaction term is completely closed and requires no modeling. Whereas information about neighboring points is missing and all gradient terms, such as molecular mixing, are unclosed and must be modeled. The mixing model is critical because combustion occurs at the smallest molecular scales when reactants and heat diffuse together. Modeling mixing in PDF methods is not straightforward, and is the weakest link in the PDF transport approach. Since the many dimensions of the composition PDF model cannot be solved by the finite volume method, a Monte Carlo based method is used when solving the PDF transport equations. This method involve imaginary particles moving randomly through physical space due to particle convection, and also through composition space due to molecular mixing and reaction. [3, 7]

The composition PDF transport model can be computationally very expensive because of the detailed chemical kinetics, and it is only available with the segregated solver, which can be a problem in cases where there is a strong

coupling between species and pressure.

4.7 Summary on combustion models

In the previous chapters a series of combustion models offered by FLUENT have been presented. When focus is on incorporating chemical kinetics to CFD modeling, the eddy dissipation concept (EDC), The mixture fraction approaches (laminar flamelet or PDF equilibrium) or the composition PDF transport model seems to be the applicable models. However when focusing on NO formation, the equilibrium and laminar flamelet approaches show some limitations, this leaves the choices between the EDC model and the composition PDF transport model, both being computationally expensive and therefore challenging when modeling large scale industrial applications.

4.8 Combustion mechanisms

The choice of combustion mechanisms in CFD modeling is usually a compromise between accuracy and computational effort. For many large scale modeling cases, the investment in detailed chemical mechanisms and advanced chemistry submodels becomes to computationally prohibitive. Instead it is often chosen to apply a simple global mechanism or even neglect finite rate chemistry and let the mixing control the combustion process using the Eddy Dissipation approach. Two global combustion mechanisms and a skeletal combustion mechanism has been applied in this work. A more elaborate discussion on the performance of global combustion mechanisms can be found in appendix A.

4.8.1 The Westbrook and Dryer two-step mechanism (WD)

The Westbrook and Dryer two step mechanism has been applied in the Eddy Dissipation/Finite rate framework. The WD model consists of two reactions, where the last step, oxidation of CO to CO_2, is reversible. The mechanism is listed in the form of three irreversible steps,

$$CH_4 + 1.5\ O_2 \rightarrow CO + 2\ H_2O \qquad \text{(WD1)}$$

$$CO + 0.5\ O_2 \rightarrow CO_2 \qquad \text{(WD2)}$$

$$CO_2 \rightarrow CO + 0.5\ O_2 \qquad \text{(WD3)}$$

Table 4.1 displays the reaction rate data for the WD mechanism. The rate constants for (WD1) and (WD2) originate from Dryer and Glassman [8] who studied high temperature oxidation reactions of carbon monoxide and methane under fuel lean conditions ($\lambda > 2$) in a turbulent flow reactor. Later, Westbrook and Dryer [9] included the reverse reaction step for CO_2 decomposition (WD3) in order to reproduce the proper heat of reaction and pressure dependence of the [CO]/[CO_2] equilibrium.

Table 4.1: Westbrook and Dryer global multi step methane combustion mechanism with kinetic data - units in cm, s, cal, mol

Mechanism	Reactions	A	β	Ea	reaction orders	Ref
WD1	CH_4 + 1.5 O_2 → CO + 2 H_2O	1.59E13	0	47.8E3	$[CH_4]^{0.7}[O_2]^{0.8}$	[8]
WD2	CO + 0.5 O_2 → CO_2	3.98E14	0	40.7E3	$[CO][O_2]^{0.25}[H_2O]^{0.5}$	[8]
WD2r	CO_2 → CO + 0.5 O_2	5.0E08	0	40.7E3	$[CO_2]$	[9]

4.8.2 The Jones and Lindstedt four-step mechanism (JL)

The Jones and Lindstedt mechanism can be implemented using the EDC approach. Jones and Lindstedt [10] developed four-step global mechanisms for several hydrocarbon fuels. For methane it involves the following steps,

$$CH_4 + 0.5\ O_2 \rightarrow CO + 2\ H_2 \qquad \text{(JL1)}$$

$$CH_4 + H_2O \rightarrow CO + 3\ H_2 \quad \text{(JL2)}$$

$$H_2 + 0.5\ O_2 \rightleftharpoons\ H_2O \quad \text{(JL3)}$$

$$CO + H_2O \rightleftharpoons\ CO_2 + H_2 \quad \text{(JL4)}$$

The mechanism consists of two irreversible reactions, (JL1) and (JL2), describing the initial oxidation steps of a hydrocarbon. The two reversible reactions, (JL3) and (JL4), control the rate of reaction for CO and H_2. The rate coefficients for methane combustion are displayed in table 4.2. Jones and Lindstedt validated the model against data for premixed methane and propane flames along with diffusion flame data for a methane-air flame. The mechanism was reported to perform well for both fuel-lean and moderately fuel-rich stoichiometries [10]. More on the implementation of the Jones-Lindstedt mechanism can be found in appendix A

Table 4.2: Jones Lindstedt global multi step methane combustion mechanism with the kinetic rate data - units in cm, s, cal, mol

#	Reactions	A	β	Ea	reaction orders	Ref
JL1	CH_4 + 0.5 $O_2 \rightarrow$ CO + 2 H_2	7.82E13	0	30.0E3	$[CH_4]^{0.5}[O_2]^{1.25}$	[10]
JL2	CH_4 + $H_2O \rightarrow$ CO + 3 H_2	0.30E12	0	30.0E3	$[CH_4][H_2O]$	[10]
JL3	H_2 + 0.5 $O_2 \rightleftharpoons$ H_2O	1.21E18	-1	40.0E3	$[H_2]^{0.25}[O_2]^{1.5}$	[10]
JL4	CO + $H_2O \rightleftharpoons$ CO_2 + H_2	2.75E12	0	20.0E3	$[CO][H_2O]$	[10]

4.8.3 Skeletal mechanism

The final mechanism applied is the skeletal mechanism (SKEL) derived from a comprehensive detailed chemical kinetic mechanism developed by Yang and Pope [11]. It contains 16 species and 41 reaction steps. The application of this mechanism increases the computational load significantly; the mechanism does however also include predictions of radical species, which can be important for accurate post-processing of pollutant formation.

4.9 References

[1] B.F. Magnussen and B.H. Hjertager. *Proc. Combust. Inst.*, 16th:719–729, 1976.

[2] D.B. Spalding. *Proc. Combust. Inst.*, 13:649–657, 1971.

[3] Fluent inc., Centerra Resource Park, 10 Cavendish Court, Lebanon, NH 03766. *Fluent 6.2 users guide*, 2005.

[4] A. Brink, C. Mueller, P. Kilpinen, and M. Hupa. *Combust. Flame*, 123:275–279, 2000.

[5] I.R. Gran and B.F. Magnussen. *Combust. Sci. Technol*, 119:171–190, 1996.

[6] I.S. Ertesvaag. *Turbulent strøyming og forbrenning.* Tapir, 2000.

[7] M.S. Skjødt-Rasmussen. Fluent 6.1 - Basic Training Notes. CHEC research centre, Department of Chemical Engineering, Technical University of Denmark, Kgs. Lyngby, 2005,. note.

[8] F.L. Dryer and I. Glassman. *Proc. Combust. Inst.*, 14:987–1003, 1972.

[9] C.K. Westbrook and F.L. Dryer. *Combust. Sci. Technol.*, 27:31–44, 1981.

[10] W.P. Jones and R.P. Lindstedt. *Combust. Flame*, 73:233–249, 1988.

[11] B. Yang and S.B. Pope. *Combust. Flame*, 112:16–32, 1998.

Chapter 5

Combustion results

This chapter includes a paper which is published the journal "Energy and Fuels". It contains the main results for experimental results and comparison with CFD modeling. Focus in the paper is on the main combustion process - NO formation is adressed in chapter . The paper also includes a description of the experimental setup, which is omitted here (chapter 2 describes the experimental setup in detail.

Experimental and numerical investigation of gas phase freeboard combustion. Part I: Main combustion process

Jimmy Andersen[1], Peter Arendt Jensen[1], Knud Erik Meyer[2], Søren Lovmand Hvid[3], and Peter Glarborg[1,*]

1: Department of Chemical and Biochemical Engineering, Technical University of Denmark, DK-2800 Kgs. Lyngby, Denmark

2: Department of Mechanical Engineering, Technical University of Denmark, DK-2800 Kgs. Lyngby, Denmark

3: DONG Energy, Kraftværksvej, DK-7000 Fredericia, Denmark

*: Corresponding author: pgl@kt.dtu.dk

5.1 abstract

Experimental data for velocity field, temperatures, and gas composition have been obtained from a 50 kW axisymmetric non-swirling natural gas fired combustion setup under two different settings. The reactor was constructed to simulate the conditions in the freeboard of a grate fired boiler, but under well-defined conditions. The experimental results are compared to CFD modeling predictions, using the Eddy Dissipation Model (EDM) as well as the Eddy Dissipation Concept (EDC). The use of EDC allows implementation of more advanced combustion schemes; we have tested the four-step global mechanism by Jones and Lindstedt [Combust. Flame 73:233-249 1988], and the 16 species, 41 reactions skeletal mechanism by Yang and Pope [Combust. Flame 112:16-32 1998]. The CFD model captured the main features of the combustion process and flow patterns. The application of more advanced

chemical mechanisms did not improve the prediction of the overall combustion process, but did provide additional information about species (especially H_2 and radicals), which is desirable for post-processing pollutant formation.

5.2 Introduction

Validation of computational fluid dynamics (CFD) models is essential if this modeling approach is to be the basis of research and design work. A considerable amount of validation data have been reported for different types of flames and combustion systems, especially swirling flames (gas/pulverised coal)[1, 2, 3] and jet flames [4, 5]. Masri et al. [6] reviewed experimental investigations of non-premixed turbulent flames. CFD modeling has also been applied to simulate a number of large-scale combustion facilities [7, 8, 9, 10, 11]. However, it is difficult to validate CFD models in large scale, since measurements from such facilities are mostly limited to exit gas emissions and temperatures.

CFD modeling is emerging as an important tool in analysis and troubleshooting for combustion in the freeboard of grate-fired units. Recently, Yin et al. [12] reviewed the concept of grate firing. However, only a limited amount of data is available for validation of CFD models for this application. A few reported studies, i.e. the pilot-scale incinerator work by Samec et al. [13] and the bubbling fluidized bed work by Brink et al. [14], deal with freeboard combustion, but none of these studies involve detailed in-furnace measurements.

The objective of the present work is to supply validation data for modeling the mixing and gas phase reactions taking place in the freeboard section of a grate fired boiler. To provide well-defined boundary and reaction conditions, the freeboard section is approximated by a 50 kW axisymmetric non-swirling natural gas fired combustion setup. Experimental data for velocity field, temperatures, and gas composition have been obtained and compared to CFD modeling predictions, using the commercial CFD code FLUENT 6.3 [15]. The CFD modeling predictions employ the Eddy Dissipation Model (EDM) and the Eddy Dissipation Concept (EDC), respectively, as well as chemical schemes from simple mixing-controlled reactions to more advanced combustion schemes. The present paper deals with the main features of the fuel oxidation and combustion process, while a companion paper [16]

emphasizes NO formation.

5.3 Experimental setup

See chapter 2.

5.4 Modeling approach

The commercial CFD code FLUENT 6.3 has been used to analyze the flow and combustion phenomena taking place in the experimental facility. The CFD code uses a finite volume approach. An incompressible (pressure based) solver has been used and second order interpolation schemes have been applied along with the SIMPLE [19] pressure-velocity coupling scheme. A 2D axi-symmetric CFD solver was used. The mesh applied in the modeling consisted of 186,000 quadrilateral cells. A grid independence test confirmed that this resolution was sufficient. The flow straightener plate consisted of 6 rings of holes with hole diameters of 16mm. In the 2D implementation these are converted to 6 slits, the measures are given in Figure 5.1. The secondary inlet air was modeled as a slit with the slit centre at freeboard radius 221 mm. The radius of the slit is 0.371 mm to obtain the same entrance area as the original holes.

One problem appeared when modeling the flow pattern in the setup. Regardless of turbulence model and variations in boundary condition within the uncertainties, the secondary air jet attached to the upper furnace wall. This eventually led to a reduction in the jet velocity and an underestimation of velocity and turbulent kinetic energy in the first measurement plane. We attribute this phenomena to a Coanda type effect [20, 21], where shear effects create a low pressure region beneath the inclined jet, attracting the jet to the wall. The 2D slit approximation of the ring of jets may facilitate this phenomena in the calculations. In reality, gaps between the jets might allow

Ring nr.	#holes	Slit center	Total area	Slit pos min	Slit pos max
0	1	0	201	0	8
1	6	48	1206	20	28
2	12	96	2413	44	52
3	20	144	4021	67.67	76.4
4	28	192	5630	91.3	100.67
5	36	240	7238	115.2	124.8

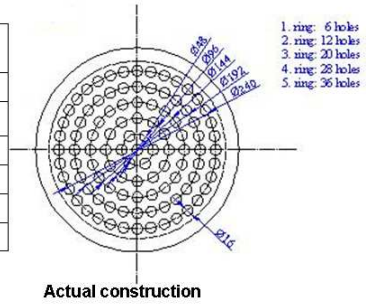

Figure 5.1: Measures for the flow straightener plate, slit pos. min. and slit pos. max. indicate positions for the 6 slits, when the flow straightener plate is converted to a 2D geometry.

a free jet to stabilize. The problem was accommodated in the calculations by artificially extending the secondary air inlet 5 mm into the freeboard area, in contrast to the actual physical geometry. Appendix E elaborates on the studies and modeling efforts related to this jet attachment phenomenon.
The choice of turbulence, radiation- and turbulence-chemistry interaction submodels is elaborated in the next sections. Gravity was included in the calculations. However, buoyancy had only a minor influence on predictions and was neglected in the calculations shown in the present work. The small impact of buoyancy is attributed to the low temperature gradients in the domain, where the inlet primary gas enters at 1300K.

5.4.1 Modeling turbulence

A complex flow pattern is observed in the experimental setup, with recirculation zones and a low Reynolds number (Re=500-1000) jet flow playing a dominant role. This kind of flow would be expected to be a challenge for simple RANS based two equation turbulence models, since parts of the flow are expected to be in the transitional region.
The Standard k-ϵ model [22] (SKE) is chosen for the modeling. Even though other turbulence models are reported to be more accurate and reliable for a

wider class of flows, the robustness of the SKE model, along with the reasonable results obtained regarding velocity and turbulence levels, has made it the choice for the present calculations. The default turbulence model constant settings are applied in the calculations ($C_{1\epsilon}$ = 1.44, $C_{2\epsilon}$ = 1.92, C_μ = 0.09, σ_k=1.0, σ_ϵ = 1.3)[22].

Modeling radiation

The radiation model chosen is the Discrete Ordinates (DO) radiation model [23], with domain based weighted sum of gray gases model (WSGGM) approximation of the absorption coefficient. Since it is a pure gas phase combustion, a scattering coefficient of 0 was chosen.

Modeling turbulence-chemistry interaction

Two different turbulence - chemistry interaction models have been applied. The first one is the Eddy Dissipation model (EDM) [24]. In order to account for the rate limiting effect of mixing processes, Magnussen and Hjertager [24] developed a combustion model (based on the eddy break-up model presented by Spalding [25]) that accounted for the turbulent mixing of fuel and products. This *Eddy Dissipation model* assumes that the chemical reaction rate is governed by the large-eddy mixing time scale $\frac{k}{\epsilon}$.
A limitation of the Eddy Dissipation model is that it does not involve temperature as a parameter. Instead the presence of product species is required - in these calculations product species enters with the inlet flow. This way combustion proceeds whenever a sufficient level of turbulence is present. The EDM constants are kept as default, with A being 4.0 and B=0.5.
The second turbulence-chemistry interaction model used is the Eddy Dissipation Concept (EDC). This approach is an extension of the Eddy Dissipation model [24] based on the work by Gran and Magnussen [26, 27]. In the EDC model chemical reactions are assumed to occur in the fine structures of the computational cells. These small scale structures can be pictured as a part

of the cell, where Kolmogorov sized eddies containing combustion species are situated so close together, that mixing on the molecular level is taking place. The EDC model in FLUENT evaluates the volume of each cell, where mixing on a molecular scale is occurring, and treats this part of the cell as a constant pressure reactor. The volume fraction of these fine scales is modeled in FLUENT as: [15]

$$\gamma^3 = C_\gamma^3 (\frac{\nu \overline{\epsilon}}{\overline{k}^2})^{3/4} \tag{5.1}$$

Here ν is the kinematic viscosity and C_γ is a volume fraction constant (2.1377). The time scale for which the chemical reactions occur, τ^*, is found by equation 5.2.

$$\tau^* = C_\tau (\frac{\nu}{\overline{\epsilon}})^{1/2} = C_{\tau^*} t_K \tag{5.2}$$

In equation 5.2 C_τ is a model constant (0.4082) and t_K is the Kolmogorov time scale. In FLUENT, combustion in the fine scales of the computational cells is assumed to occur as a constant pressure reactor, with initial conditions taken as the current species and temperature in the cell.

5.4.2 Combustion mechanisms

The choice of combustion mechanism is highly dependent on the level of detail requested from the CFD analysis. A simple two step mechanism along with the Eddy Dissipation model can be adequate when the goal is to estimate heat transfer and major species conversion in a combustion process. This way no kinetic limitations are put on the reaction rate. In the present study this approach is applied as a baseline standard CFD approach [15]:

$$CH_4 + 1.5\ O_2 \rightarrow CO + 2\ H_2O \tag{step1}$$

$$CO + 0.5O_2 \rightarrow CO_2 \tag{step2}$$

The Jones and Lindstedt [28] global four step combustion mechanism (JL) is implemented in the EDC approach as elaborated in Andersen et al. [29]. Four step mechanisms are offered for several hydrocarbon fuels. For methane it involves the following steps,

$$CH_4 + 0.5\ O_2 \rightarrow CO + 2\ H_2 \tag{JL1}$$

$$CH_4 + H_2O \rightarrow CO + 3\ H_2 \tag{JL2}$$

$$H_2 + 0.5\ O_2 \rightleftharpoons\ H_2O \tag{JL3}$$

$$CO + H_2O \rightleftharpoons\ CO_2 + H_2 \tag{JL4}$$

The mechanism includes two irreversible reactions, (JL1) and (JL2), describing the initial oxidation steps of a hydrocarbon. The two reversible reactions, (JL3) and (JL4), control the rate of reaction for CO and H_2. Jones and Lindstedt validated the model against data for premixed methane and propane flames along with diffusion flame data for a methane-air flame. The mechanism was reported to perform well for both fuel-lean and moderately fuel-rich stoichiometries [28]. One advantage of applying this mechanism is that it includes a prediction of H_2, which can be required in post-processing of NO formation.

The final mechanism applied is the skeletal mechanism (SKEL) derived from a comprehensive detailed chemical kinetic mechanism by Yang and Pope [30]. It contains 16 species and 41 reaction steps. The application of this mechanism increases the computational load significantly; however, the mechanism does also include predictions of radical species.

5.5 Results and Discussion

The key measured emission data for the two settings analyzed are summarized in Table 5.1. The higher secondary air flow applied in setting 1 results

in a higher outlet O_2 concentration, but also the NO emission is increased in setting 1. Several of the result plots in this section contain two experimental series, one labeled near side and one labeled far side. These labels refer to the side of the reactor from which the experiments are performed, either by inserting an extraction probe or by laser measurements.

Table 5.1: Measured exhaust concentration data for the two settings analyzed, all concentration indications are volume based.

	Setting 1	Setting 2
Overall stoichiometry (λ)	1.4	1.02
O_2	6.7 % dry	0.7 % dry
CO	0.0% dry	0.0% dry
CO_2	7.7 %	11.0 %
NO	207 ppm dry	170 ppm dry

In the initial calculations the flow pattern and turbulence levels are frozen from the Eddy Dissipation solution for setting 1, while concentrations and temperature fields are calculated using EDC as well. This approach provides the chemical mechanisms with similar prerequisites and makes them easier to compare. The reason for this will be elaborated later.

Figures 5.2 to 5.7 show comparisons of measurement data and CFD calculations. The measurements display high velocities at the secondary air inlets and a recirculation zone is measured near the walls in the top section of the reactor. The setting 2 flame shows a high CO and low O_2 concentration in the centre at the top of the furnace chamber. For the setting 1 flame, a high O_2 concentration is observed at all radial positions, including that only 88 mm from the top, indicating a fast and early mixing of fuel mixture and secondary air. The measurements indicate reasonably but not perfect rotational symmetry.

5.5.1 Flow field comparison

Figures 5.2 and 5.3 compare the CFD predictions of velocity and velocity fluctuation fields with the experimental measurements. A better overall

agreement between CFD predictions and measured data was obtained for setting 2, both for flow field and RMS values (figure 5.3). The LDA measurements in figures 5.2 and 5.3 display differences between the near and far side regions; for instance, the last two positions at the far wall sometimes do not yield negative velocities as the corresponding at the near wall. It is likely that these differences in data for the near and far side regions are due to imperfect symmetric conditions in the setup. However, the far-wall data are considered to be slightly less reliable, due to the thermal disturbances of the laser beam due to the long beam path inside the furnace.

The setting 1 flow field shows some deviations between measured data and calculations. In general the CFD predictions have a more parabolic velocity profile than measured and an outer recirculation zone is erroneously predicted to stretch too far down in the reactor. This ultimately results in overestimated velocities in the centre of the reactor. However, as the combustion results will show, this is in the post flame zone and has little impact on the combustion process.

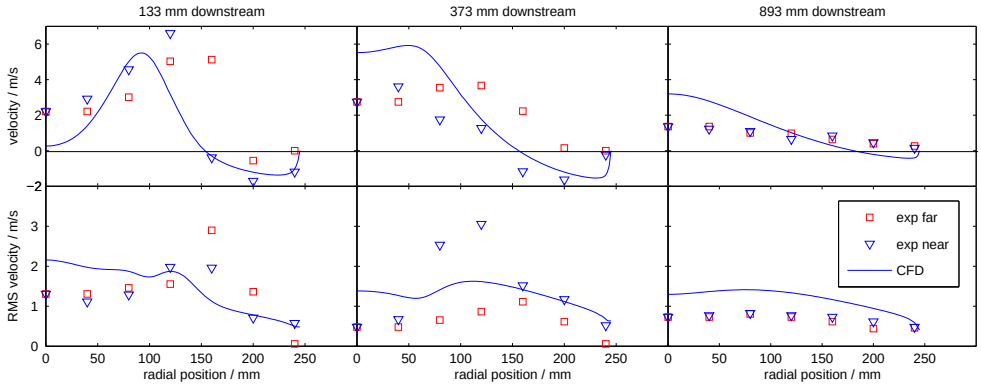

Figure 5.2: Comparison of axial velocity and RMS velocity between experimental data (symbols) and CFD predictions (lines) with high velocity secondary air (setting 1). CFD solution with the EDM combustion approach.

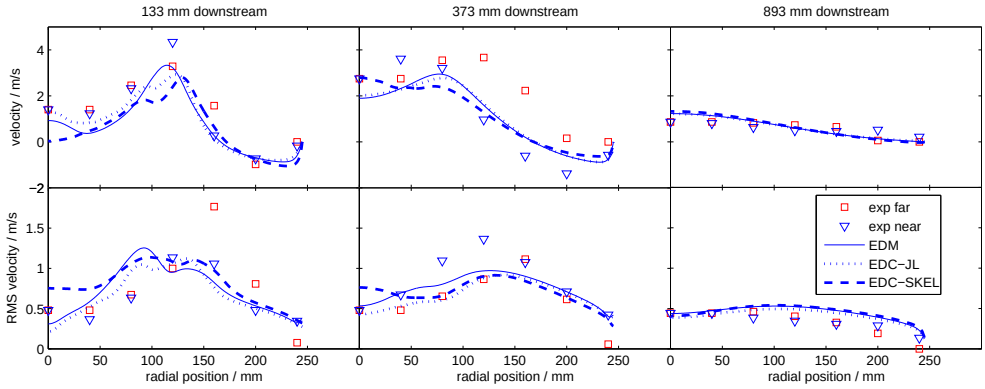

Figure 5.3: Comparison of axial velocity and RMS velocity between experimental data (symbols) and CFD predictions from the EDM approach (solid line), the EDC-JL mechanism (dotted) and the EDC-SKEL mechanism (dashed) with low velocity secondary air (setting 2).

5.5.2 Concentration and Temperature comparison

Figures 5.3, 5.4 and 5.5 compare CFD predictions and experimental data for setting 2. Figure 5.5 contains two experimental series, one labeled near side as to where the extraction probe is inserted and one labeled far side. Similar to the velocity profiles some disagreement for CO and O_2 is observed between the two measurement sides, especially in the top section of the reactor. This difference can mostly be attributed to the measurement technique. It is expected that inserting a probe and traversing through the combustion (flame) region might disturb the flame and draw combustible gases along the probe. For this reason, the near side measurements are expected to be more reliable. Regarding the temperature measurements in Figure 5.5, a reasonable agreement with modeling for both the average temperature level and trends is found, although the peak values are not in exact agreement. Peak values can be difficult to capture using a suction pyrometer, which inevitably will measure an average temperature in a region - here expected to have a diameter of 6 cm. Furthermore, the CFD modeling does not take soot effects into account. The cooled probes often showed traces of soot condensing on them. Radiation from soot particles in a flame usually lowers the flame temperature, which could explain the overprediction of temperature in the reaction zone.

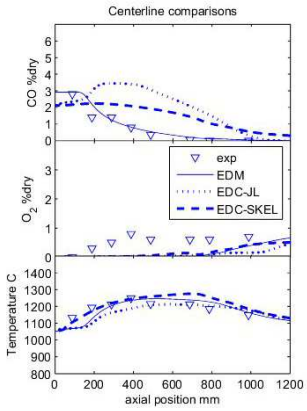

Figure 5.4: Comparison of temperature (°C) and concentrations between experimental data (symbols) and CFD predictions from the EDM approach (solid line), the EDC-JL mechanism (dotted) and the EDC-SKEL mechanism (dashed) at the centerline of the furnace, with low velocity secondary air (setting 2)

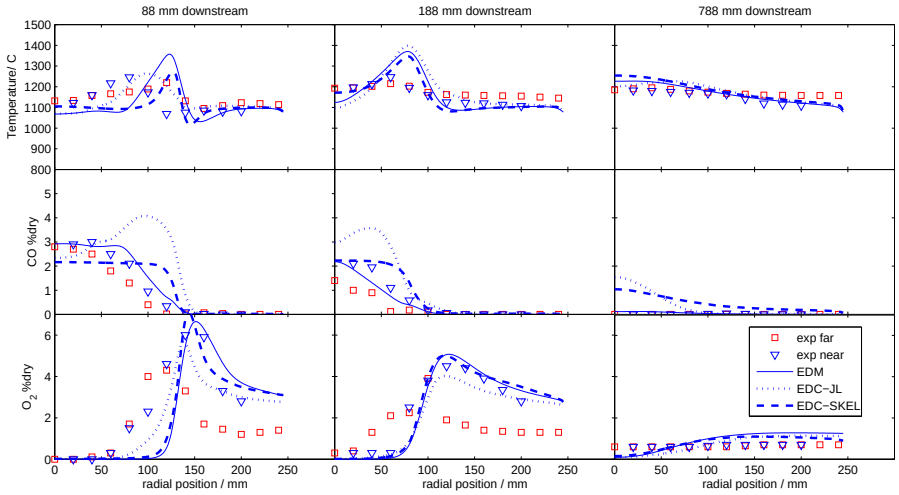

Figure 5.5: Comparison of temperature (°C) and concentrations between experimental data (symbols) and CFD predictions from the EDM approach(solid line), the EDC-JL mechanism (dotted) and the EDC-SKEL mechanism (dashed) with low velocity secondary air (setting 2)

Figures 5.4 and 5.5 show that for setting 2 the three combustion mechanisms provide fairly similar results, with the main difference being the predicted CO concentrations. Both the EDC models predict an initially increasing and higher CO concentration through the flame zone, which is not surprising since the EDC mechanisms include kinetic rate limitations (see Figure 5.4). The EDM solution disregards this kinetic difference and treats both reaction steps with only mixing-controlled rates. The experimental results are in better agreement with the EDM solution, however, which could indicate that mixing effects dominate over finite rate chemistry in this setup. In general there is a good agreement between the prediction from the two step Eddy Dissipation model and the experiments. The EDC model with the Jones Lindstedt mechanism implementation does not perform as well for CO (see Figures 5.4 and 5.5). This can be due to the reaction (JL2), which causes methane in the primary gas to form CO and H_2 before the contact with the secondary air. This reaction, which causes a slight increase in CO levels, is endothermic and may explain the slightly lower temperatures in the primary gas mixture for the EDC-JL mechanism. The skeletal mechanism in general performs similarly to the JL mechanism. It also overpredicts CO downstream and in the first two transverse positions but not with as high values as the JL mechanism.

Figures 5.6 and 5.7 show temperature and species concentration comparisons between CFD predictions and experimental data for setting 1. The experimental measurements from this setting showed that the combustion zone was positioned above the first measurement plane, so that almost all fuel is converted near the second stage inlet.

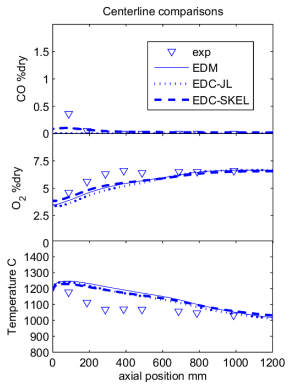

Figure 5.6: Comparison of temperature (°C) and concentrations between experimental data (symbols) and CFD predictions from the EDM approach (solid line), the EDC-JL mechanism (dotted) and the EDC-SKEL mechanism (dashed) at the centerline of the furnace, with high velocity secondary air (setting 1). EDC results are calculated on a frozen flow and turbulence field based on the EDM solution.

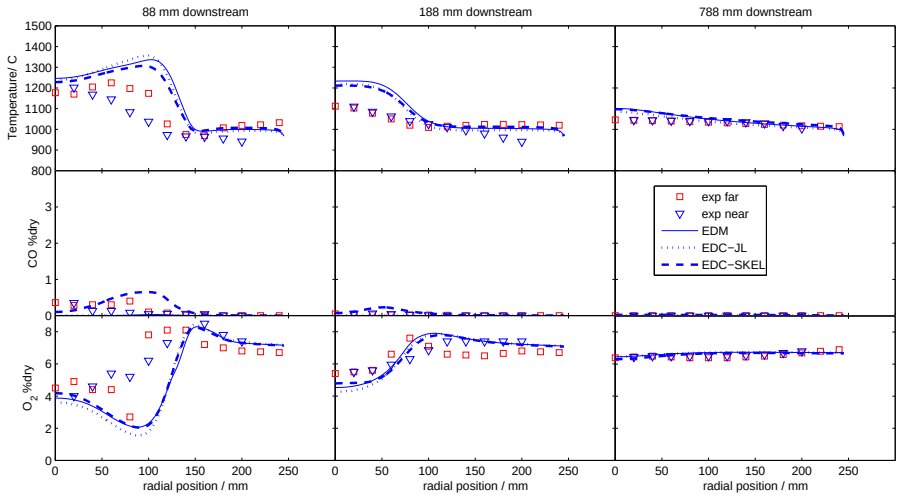

Figure 5.7: Comparison of temperature (°C) and concentrations between experimental data (symbols) and CFD predictions from the EDM approach(solid line), the EDC-JL mechanism (dotted) and the EDC-SKEL mechanism (dashed) with high velocity secondary air (setting 1). EDC results are calculated on a frozen flow and turbulence field based on the EDM solution.

The CFD models predict a central recirculation zone in the top of the freeboard section, which forces air and primary gas to meet just below the flow straightener. This is illustrated with the velocity vectors in Figure 5.8. This recirculation zone is not present in the setting 2 predictions, and it serves to explain the dramatic shift in reaction zone size. This means that all the setting 1 comparisons are limited to the postflame zone, and the kinetic models naturally predict similar results. The skeletal mechanism does however predict a low concentration of CO to be present at the first measurement plane, which does not seem to be in disagreement with the measurements.

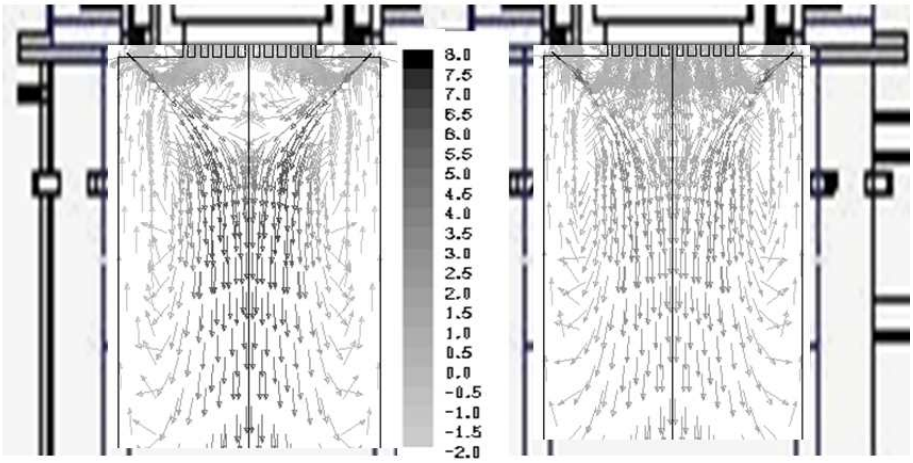

Figure 5.8: Velocity vectors coloured by axial velocity. Left: setting 1 Right: setting 2. Top half of freeboard section displayed (EDM cases)

The EDC approaches with the skeletal and JL mechanisms in general predict slower fuel conversion and hence lower temperatures near the flame front as Figure 5.9 illustrates. Here it is shown that beneath the secondary inlet jet for setting 1, the EDM approach predicts higher temperatures than the EDC approaches. If the mechanisms are not adapted to the same flow field, it was experienced that the choice of chemical mechanism could have a dramatic influence on the solution.

In Figures 5.11 and 5.12 the EDC calculations including full coupling with the flow calculations compared with the measurements for setting 1 are shown.

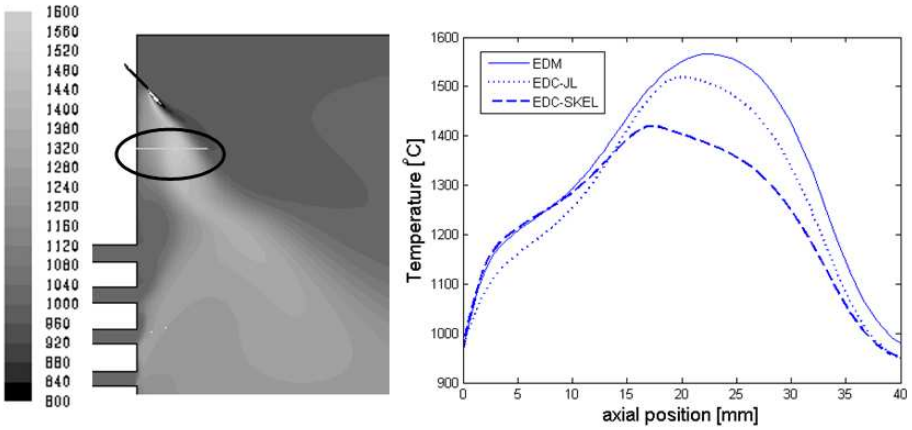

Figure 5.9: Left: Temperature contours for EDM - setting 1 in °C. Right: Comparison of temperature levels in highlighted plane on left contour plot for EDM, EDC-JL and EDC-SKEL in °C.

The slower conversion and lower temperatures beneath the secondary air inlet predicted by the EDC mechanisms would reduce the gas expansion and allow the secondary jet to bend toward the wall, as sketched in Figure 5.10. This results in a collapse of the internal recirculation zone that causes the location of the initial combustion zone to be positioned near the second stage inlet. The EDC finite rate mechanisms predict a combustion zone to stretch further down the furnace similarly to setting 2, with temperature and species field in disagreement with the measurements as indicated in Figure 5.11. The top section LDA measurements in Figure 5.12 also confirm that the EDM solution is in better agreement with the measurements.

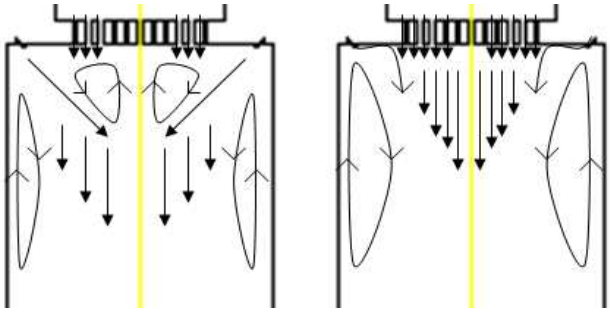

Figure 5.10: Illustration of flow field solutions for setting 1. Left: EDM with internal recirculation zone. Right: EDC with jet attachment and no internal recirculation zone.

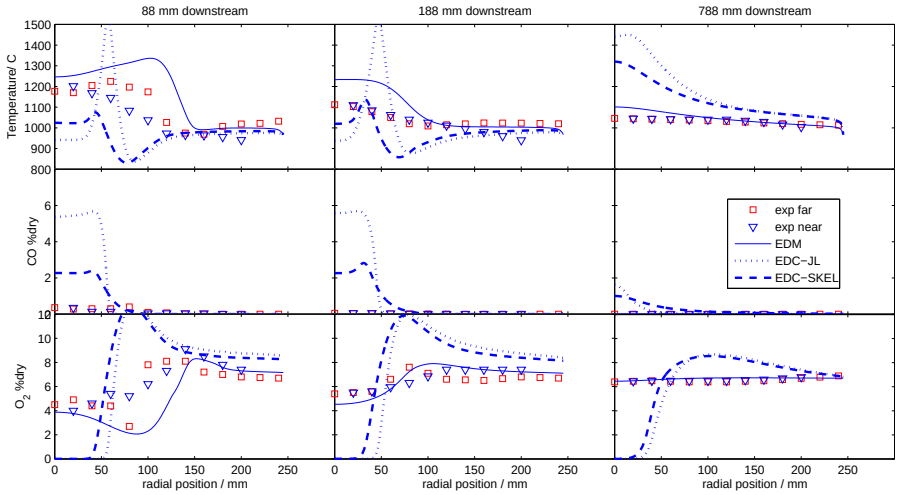

Figure 5.11: Comparison of temperature (°C) and concentrations between experimental data (symbols) and CFD predictions from the EDM approach(solid line), the EDC-JL mechanism (dotted) and the EDC-SKEL mechanism (dashed) with high velocity secondary air (setting 1).

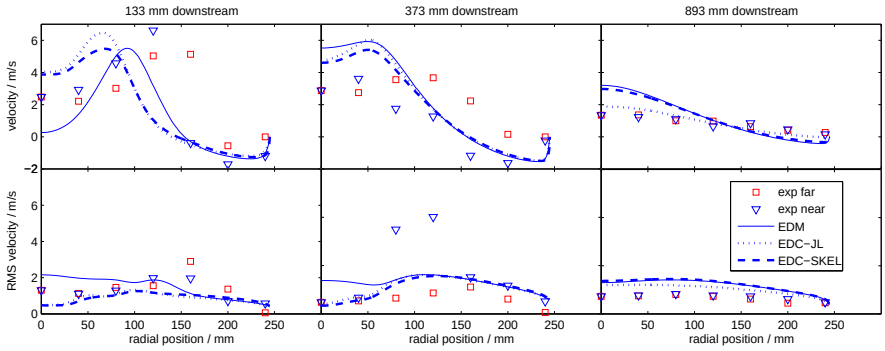

Figure 5.12: Comparison of axial velocity and RMS velocity between experimental data (symbols) and CFD predictions from the EDM approach (solid line), the EDC-JL mechanism (dotted) and the EDC-SKEL mechanism (dashed) with high velocity secondary air (setting 1)

One should be cautious to conclude that the EDM approach is superior to EDC, but the present results show that the sensitivity in the modeled system to combustion approach is substantial, and the system itself is quite sensitive to small changes related to the stability of the secondary air jet.
Setting 1 does not provide as good a validation case as setting 2, since the combustion zone is not mapped by the measurements. The CFD modeling does however provide an explanation as to why the combustion region is located upward in the setting 1 case.

5.6 Conclusion

Experimental data from a 50 kW axisymmetric, non-swirling natural gas fired combustion setup, imitating the conditions of the freeboard in a grate-fired boilers, are presented. Measurements, including local values of velocity, temperature, and gas concentrations, were obtained for two different experimental settings. Calculations with CFD showed a substantial sensitivity toward the combustion modeling approach, and the system itself was quite sensitive to small changes related to the stability of the secondary air jet. CFD modeling with the Eddy Dissipation Model for the gas combustion captured the main features of the combustion process and alternation in flow patterns between the two settings. The predictions were in reasonable agreement with observed values for flow and turbulence levels, temperature, and major species concentrations. More advanced combustion mechanisms were also tested, at a considerably increased computational expense, by using the Eddy Dissipation Concept (EDC) turbulence interaction model. However, the use of EDC with finite rate chemistry (The Jones-Lindstedt four-step global mechanism or the skeletal mechanism from Yang and Pope) resulted in a too slow fuel conversion. For the high secondary air velocity setting, this deficiency resulted in dramatic changes in the predicted species and temperature field. Only when the EDC calculations were superimposed on the flow-field from the EDM modeling, did the more advanced turbulence chem-

istry interaction model and finite rate chemistry provide satisfactory results. However, the advanced mechanisms may be more suitable for pollutant post-processing, as they predict a wider range of species.
Based on the results of the present work, the additional computational effort to implement the more detailed chemistry using the EDC approach may not yield improved computational accuracy. In the investigated system, the fuel conversion is dominated by the mixing process of fuel and air, and finite rate effects are negligible or within the uncertainties of the measurements. However, the Reynolds number in the system is quite low (Re $\approx$ 1000), and the assumptions of fully turbulent isotropic turbulence within the k-ϵ turbulence model is probably not as good as it would be in a fully turbulent large scale facility. This concern also goes for some of the constants within the turbulence chemistry interaction models.

5.7 Acknowledgments

The present work was funded by the Technical University of Denmark, DONG Energy, Vattenfall, Babcock &Wilcox Vølund, B&W Energy, The Danish Technical Research Council, and the Public Service Obligation programme under contract PSO 4792. The authors would like to acknowledge the helpful experimental assistance from senior researcher Sønnik Clausen.

5.8 References

[1] Sloan; D.G.; Smith.; P.J.; Smoot, L.D. Prog. Energ. Combust. Sci. 1986, 12, 163-250.

[2] Jensen, P.A.; Ereaut, P.R.; Clausen, S.; Rathmann, O. J. Inst. Energy 1994, 67, 37-46.

[3] Meier, W.; Keck, O.; Noll, B.; Kunz, O.; Stricker, W. Applied Physics B 2000, 71, 725-731 .

[4] Barlow, R.S.; Frank, J.H. Proc. Combust. Inst. 1998, 27, 1087-1095.

[5] Dally, B.; Masri, A.R., Barlow, R.S.; Fiechtner, G. Combust. Flame 1998, 114, 119-148.

[6] Masri, A.R.; Dibble, R.W.; Barlow, R.S. Prog. Energ. Combust. Sci. 1996, 22, 307-362.

[7] Klason, T.; Bai, X.S. Fuel 2007, 86, 1465-1474.

[8] Saario, A.; Oksanen, A. Energy Fuels 2008, 22, 297-305.

[9] Yin, C.; Rosendahl, L.; Kær, S.; Clausen, S.; Hvid, S.L.; Hille, T. Energy Fuels 2008, 22, 1380-1390.

[10] Diez, L.I.; Cortes, C.; Pallares, J. Fuel 2008, 87, 1259-1269.

[11] Miltner, M.; Makaruk, A.; Harasek, M.; Friedl, A. Clean Techn. Environ. Policy 2008, 10, 165-174.

[12] Yin, C.; Rosendahl, L.; Kær, S. Prog. Energ. Combust. Sci. 2008, 34, 725-754.

[13] Samec, N.; Kokalj, F.; Chen, J.-Y. Env. Eng. Sci. 2007, 24, 905-916.

[14] Brink, A.; Hupa, M.; Kurkela, E.; Suomalainen, M. Prog. Comput. Fluid Dyn. 2006, 6, 217-224.

[15] Fluent 6.3 users guide, Fluent inc., Centerra Resource Park, 10 Cavendish Court, Lebanon, NH 03766 (2005)

[16] Andersen, J.; Jensen, P.A.; Hvid, S.L.; Glarborg, P. Experimental and numerical investigation of gas phase freeboard combustion. Part II: Fuel-NO formation. Submitted for publication (2009)

[17] Glarborg, P.; Jensen, A.D.; Johnsson, J.E. Prog. Energ. Combust. Sci. 2003, 29, 89-113.

[18] Bird, R.B.; Stewart, W.E.; Lightfoot, E.N. Transport Phenomena, 2nd edition, John Wiley and Sons Inc. (2002)

[19] Vandoormaal, J.P.; Raithby, G.D. Num. Heat Transfer 1984, 7, 147-163.

[20] Hoch, J.; Jiji, L.M. J. Fluids Eng. 1981, 103, 154-161.

[21] Alekseenkov, S.V.; Markovich, D.M. J. Appl. Mech. Tech. Phys. 1997, 38, 417-422.

[22] Launder, B.E.; Spalding, D.B. Lectures in Mathematical Models of Turbulence, Academic Press, London, England (1972)

[23] Chui, E.H.; Raithby, G.D. Num. Heat Transfer Part B 1993, 23, 269-288.

[24] Magnussen, B.F.; Hjertager, B.H. Proc. Combust. Inst. 1976, 16, 719-729.

[25] Spalding, D.B. Proc. Combust. Inst. 1971, 13, 649-657.

[26] Gran, I.; Magnussen, B.F. Combust. Sci. Technol. 1996, 119, 171-190.

[27] Gran, I.; Magnussen, B.F. Combust. Sci. Technol. 1996, 119, 191-217.

[28] Jones, W.P.; Lindstedt, R.P. Combust. Flame 1988, 73, 233-249.

[29] Andersen, J.; Rasmussen, C.L.; Giselsson, T.; Glarborg, P. Energy Fuels 2009, 23, 1379-1389.

[30] Yang, B.; Pope, S.B. Combust. Flame 1998, 112, 16-32.

Chapter 6

NO_X formation and destruction

The long term scope of this study is to develop a CFD based method capable of predicting the NO_X chemistry in the freeboard section of grate fire boilers. The motivation for this is that NO_X emissions contribute to depletion of the ozone layer and cause acid rain, therefore NO_X emissions are limited by legislation in most parts of the world. The expression NO_X refers to any nitrogen oxide NO, NO_2, N_2O or N_XO_Y, with respect to combustion emissions NO is usually responsible for 90% of the NO_X emitted.
There are 3 main NO_X formation mechanisms, the following chapter will elaborate on these mechanisms:

- Thermal NO_X
- Prompt NO_X
- Fuel NO_X

6.1 Thermal NO

The thermal (or Zeldovich [1]) NO formation mechanism refers to the oxidation of atmospheric N_2. Since N_2 is a very stable molecule high temperatures

are needed for breaking the N-N triple bond, and thermal NO formation is only significant at high temperatures. The main elementary reaction steps for thermal NO formation are [2]:

$$O + N_2 \rightleftharpoons NO + N \tag{6.1}$$

$$N + O_2 \rightleftharpoons NO + O \tag{6.2}$$

and

$$N + OH \rightleftharpoons NO + H \tag{6.3}$$

The reactions (6.1)-(6.3) involve radicals O and OH which also play an important role in the fuel oxidation. So in general it is necessary to couple thermal NO reactions to the fuel oxidation sequence. Since the overall rate of NO formation is quite slow compared to the fuel oxidation decoupling of the NO formation equations can be performed, and the radical concentration can be estimated from assuming equilibrium values of temperature and concentrations. However superequilibrium radical concentrations are reported and can cause significant deviations in the predicted NO concentrations [2]. Alternative routes than the one stated in reactions (6.1) to (6.3) do exist for instance the N_2O/NO mechanism, which has some significance for temperatures lower than 1500°C [3, 2]:

$$O + N_2 + M \rightleftharpoons N_2O + M \tag{6.4}$$

$$N_2O + O \rightleftharpoons NO + NO \tag{6.5}$$

Another route to NO formation recently discovered by Bozzelli and Dean [4] is the NNH pathway (reactions 6.6 to 6.7). The NNH and N_2O pathways are reported to have importance at temperatures below 1500°C, while the thermal route is dominant above 1600°C [3].

$$N_2 + H \rightleftharpoons NNH \tag{6.6}$$

$$NNH + O \rightleftharpoons NO + NH \tag{6.7}$$

6.2 Prompt NO

Another pathway for the formation of NO is the prompt (or Fenimore [5]) mechanism. Fenimore discovered that some NO was rapidly produced in the flame zone of laminar premixed flames, long before any thermal NO could be formed and connected this discovery to attack by fuel radical (CH) on atmospheric nitrogen. The main elementary steps in the prompt NO mechanism, following the preceding formation of methane derived radicals, are proposed to be [2]:

$$CH + N_2 \rightleftharpoons HCN + N \tag{6.8}$$

$$CH_2 + N_2 \rightleftharpoons HCN + NH \tag{6.9}$$

$$CH_2 + N_2 \rightleftharpoons H_2CN + N \tag{6.10}$$

and

$$C + N_2 \rightleftharpoons CN + N \tag{6.11}$$

The formation product HCN and N from reaction 6.8 was originally proposed by Fenimore [5] However both theoretical calculations and experimental evidence [6] have concluded that NCN can act as the intermediate adduct, which sequentially reacts to form HCN and eventually NO [7].

$$CH + N_2 \rightleftharpoons NCN + H \tag{6.12}$$

However El Bakali and coworkers came to the conclusion that it is mainly the HCN oxidation sequence that is responsible for the NO formation [7].
Once HCN is formed it may follow the chain sequence for oxidation to NO described in figure 6.1.
In very fuel rich regions the chemistry becomes more complex, and NO may instead be reduced by CH radicals, thereby reducing the NO concentration instead through reburning processes (see chapter 6.4.1).

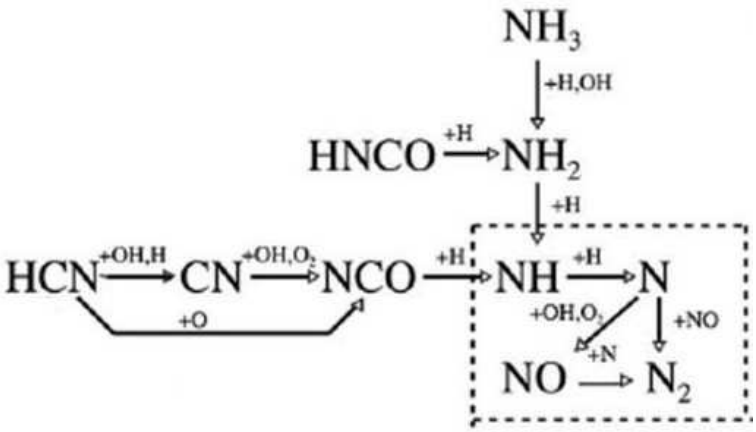

Figure 6.1: Oxidation mechanism for HCN and NH_3 [8].

6.3 Fuel NO

Many solid fuels contain significant amounts of nitrogen, which will be released during the different phases of the combustion process; devolatilization and char burnout. It is of importance for the NOx formation whether the fuel nitrogen is released during devolatilization or char burnout. For some biomass fuels significant amounts of NH_3 may be released during devolatilization [8]. For coal and higher ranked fuels, the fuel bound nitrogen is primarily released as HCN. The reason for this difference is that nitrogen in coals are typically bound in aromatic carbon structures, whereas nitrogen in biomass is more likely to be found in some sort of amine or amide structure [9]. When the fuel nitrogen is released it will participate in gas phase reactions to form NO as indicated in figure 6.1. To stress how complex the nitrogen chemistry is, ammonia is actually also used to reduce NO emission using the SNCR process (see chapter 6.4.2).

6.4 NO_X abatement strategies

In order to reduce NO_X emissions from combustion systems different strategies are used. The reaction chemical methods such as reburning and Selective Non-Catalytical Removal (SNCR) can remove already formed NO. This can also be done by help from a catalyst (usually Vanadium based) this process is called Selective Catalytic Removal (SCR) and takes place at lower temperatures. The SCR catalyst are normally very efficient and can reduce NO emission with more than 90% [10], but the process is also significantly more expensive than other abatement strategies.
Other strategies used to decrease NO_X emissions are air staging; in order to decrease the oxygen content in the hot regions of a furnace and thereby decrease thermal and fuel NO formation, secondary air is introduced further downstream in the freeboard section to oxidize the remaining combustion gases. Burner constructions such as swirl burners are designed to decrease NO formation. The swirling air will cause a flow pattern, that returns the combusted gas to the near burner region, this causes the primary combustion to take place in region with less oxygen and lower temperatures, which reduces the NO formed. This effect can also be obtained by recirculating flue gas with the oxidizing air.

6.4.1 NO_X reburning

Reburning is a technique used for NO_X emission reduction. The main idea is to introduce a secondary fuel downstream of the primary combustion zone creating a fuel rich environment where some of the NO from the primary zone is converted to N_2, HCN and NH_3 by reaction with hydrocarbon radicals [11]. Typical NO reduction levels of 35-65% are reported[12].
The mechanism for NO reduction due to reburning is initiated mainly by reaction between CH_i radicals and NO:

$$CH_i + NO \rightleftharpoons HCN + ... \tag{6.13}$$

After HCN is formed it decays through $NCO \rightarrow NH \rightarrow N \rightarrow N_2$ as illustrated in figure 6.1 [12].

6.4.2 Selective Non-Catalytic Removal of NO_X (SNCR)

The SNCR process is a process where an amine, typically ammonia or urea ($(NH_2)_2CO$) is injected into the combustion flue gas. The process works only in a narrow temperature range from 1100 - 1400K as experimental (plug flow) data from figure 6.2 illustrates.

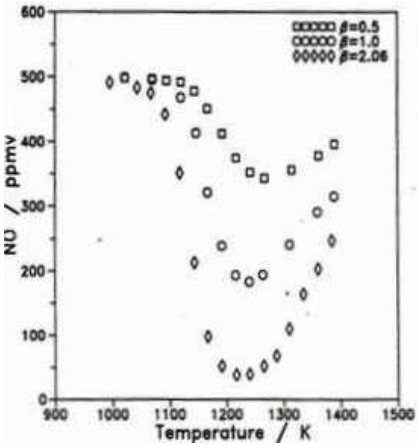

Figure 6.2: NO reduction by ammonia injection in a plug flow reactor[13].

For the SNCR process to work, that it must be implemented in an oxygen rich environment. The process is initiated by a radical attack on the reducing agent to form the amidogen radical NH_2 The most important kinetic aspect of the SNCR process is the reaction between NH_2 and NO [2, 14]:

$$NH_2 + NO \rightleftharpoons NNH + OH \tag{6.14}$$

$$NH_2 + NO \rightleftharpoons N_2 + H_2O \tag{6.15}$$

Different additives such as hydrogen peroxide can shift the window for the SNCR process to lower temperatures due to generation of chain carrying radicals.

6.5 NO modeling in this project

Although a lot of effort has been put in modeling and understanding NO formation and destruction on a theoretical and experimental lab scale level it still remains a challenge to quantitatively predict NO emissions from large combustion systems. This is due to local changes in temperature and oxygen concentration, which largely affects NO emissions. Figure 6.3 provides an idea about in which combustion regions the different NO mechanisms dominate. In the experimental setup, the main source of NO_X is fuel NO from the added ammonia. Fuel NO being the primary NO source is equivalent to, what is found in a biomass fired power plant [15].

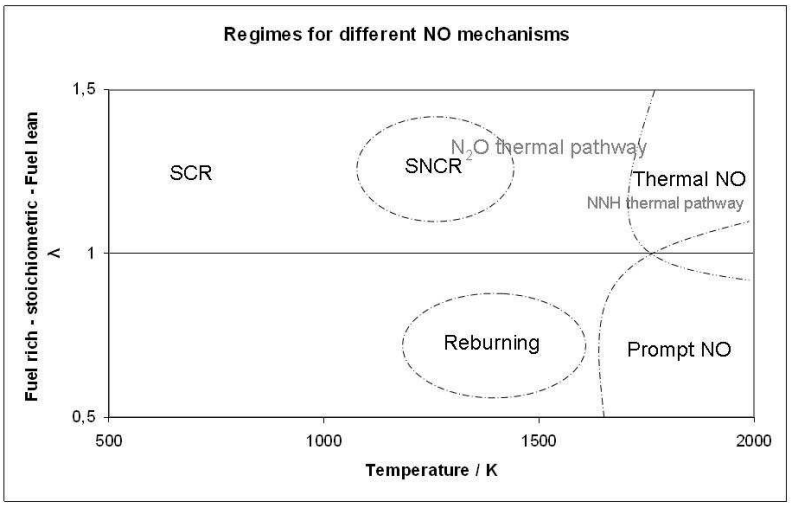

Figure 6.3: Overview of the stoichiometry and temperature where the described mechanisms play a dominating role

6.5.1 Optimal conditions for minimizing fuel NO

The intention of accurately being able to quantify the fate of ammonia released to the freeboard is especially interesting, due to the selectivity of the nitrogen chemistry.

In order to determine the optimal combustion condition with respect to minimization of NO formation a series of isothermal plug flow reactor calculations have been performed using Senkin [16]. A residence time of 1 sec is used and the temperature and combustion stoichiometry is varied in order to determine the optimal window for minimizing fuel NO.

The detailed chemical kinetic mechanism adopted to perform the calculations consisted of oxidation subsets for CH_4 and NH_3, together with a subset describing hydrocarbon/nitrogen interactions. The mechanism was drawn mostly from recent work on oxidation of C1/C2-hydrocarbons [17, 18, 19, 20] NH3 [21] and HCN [22], as well as interactions of these components [17, 23]. In the calculations, the N_2 concentration in the air is modeled as Ar in order to solely quantify fuel N conversion.

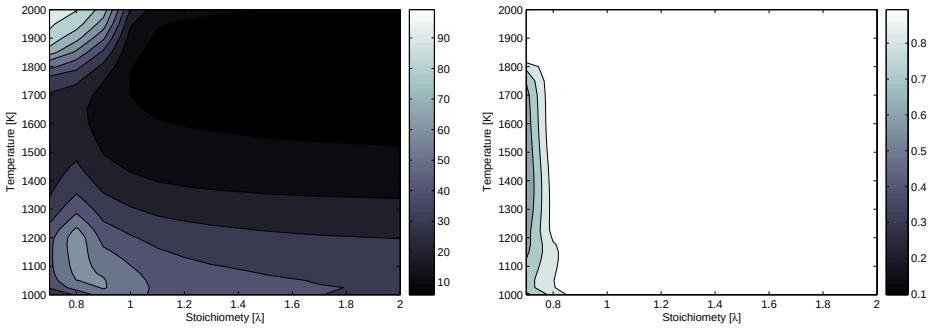

Figure 6.4: Left: Contour plot of the percentage of NH_3 converted to N_2, results from 1 sec. plug flow reactor calculations, with 1000 ppm NH_3 in a methane-air mixture. Right: Contour plot of the conversion of NH_3 to either NOx or N_2. X axis: Air excess ratio λ, Y axis: Temperature in K

Figures 6.4 and 6.5 (left) shows the percentage of NH_3 converted to N_2 at different stoichiometries and temperatures under combustion and post-

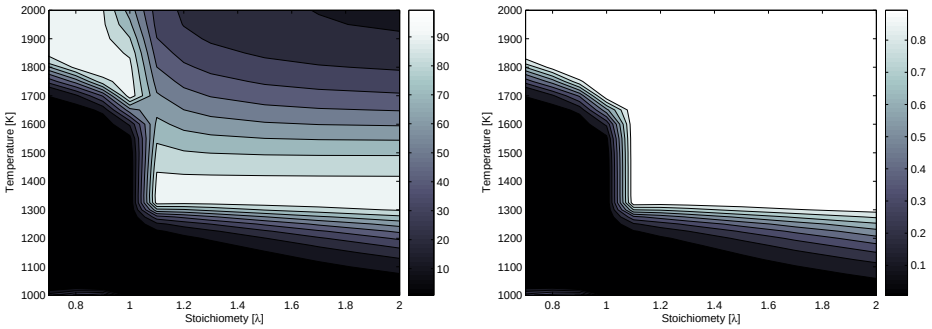

Figure 6.5: Left: Contour plot of the percentage of NH_3 converted to N_2, results from 1 sec. plug flow reactor calculations, with 1000 ppm NH_3 in a mixture of the flue gas from a 1 sec. PFR methane combustion. Right: Contour plot of the conversion of NH_3 to either NOx or N_2. X axis: Air excess ratio λ, Y axis: Temperature in K

combustion conditions respectively. Figure 6.4 (right) indicate, that at very fuel rich conditions, ammonia is not converted to stable emission compounds as NO and N_2 during combustion. At lower temperatures than 1000 K NH_3 will not be converted (the methane is not predicted to ignite) and at fuel rich conditions cyano compounds are predicted to appear.

Figure 6.5 (right) shows that the conversion of NH_3 added to the flue gas composition of a 1 sec PFR calculation does not oxidize at fuel rich condition due to the unavailability of oxidizer. Also at temperatures below 1300 K at fuel lean conditions the mechanism does not predict the mixture to react within 1 sec of residence time.

The bright areas indicate conditions, where NH_3 oxidation mainly will yield N_2. On Figure 6.5 the SNCR window appears as the bright bond in the fuel lean region of the left contour plot. A brighter area can also be located during combustion at lower temperatures in Figure 6.4 (left).

When comparing the two contour plots in figures 6.4 and 6.5 it is indicated that the SNCR process is more efficient for NH_3 in a flue gas atmosphere, than in a real combustion atmosphere. Alzueta et al. [11] investigated the hybrid

reburning-SNCR technique in a flow reactor. They found that the presence of CO shifted the SNCR window to lower temperatures (850-1000K). This decrease in temperature window is observed in figure 6.4, but apparently more of the NH_3 oxidizes to NO under combustion conditions according to these calculations. This can be explained by the recent findings of Javed et al. [14] that the presence of even H_2 impairs the NO reduction capacity of NH_3. The optimal window for oxidizing NH_3 in a combustion environment seems to be at fuel rich conditions and low temperatures between 1000 and 1200 K, in this region the reburning reactions are expected to help convert formed NO to N_2. At these conditions only 30% of the ammonia is converted to NO. This region of optimal NO reduction is in agreement with, what primary abatement strategies such as air staging and flue gas recirculation strive to achieve; low temperatures and a fuel rich primary combustion zone.

The quantity of fuel bound nitrogen in solid fuels is quite large compared to the emission regulations as discussed initially on page 4 roughly less than 10% of the fuel bound N may be conversed to NO, if secondary abatement strategies are to be avoided. The ammonia conversion predicted during combustion in Figure 6.4 shows that homogeneous reactions alone does not limit fuel-N conversion to 10%. The calculations predict 30-40% of fuel N conversion to NO during optimal combustion conditions. Experimental results with solid fuel combustion can however show lower conversion of fuel-N to NO [24, 25, 8, 26]. This further reduction of NO can be explained by gas-solid reactions, where NO is reduced to N_2 on solid carbon surfaces such as char and soot [8]. This reduction of NO emissions based on gas-solid interactions increases with particle size, coarser particles can however decrease fuel conversion.

6.5.2 Ammonia oxidation mechanisms

Several comprehensive ammonia oxidation mechanisms are available in the literature e.g. [17, 21]. However it is often chosen in CFD modeling to append a global mechanism to reduce the computational load. Table 6.1 summarizes some of the global mechanisms proposed in the literature.

Table 6.1: Ammonia oxidation mechanisms - units A:[mol m^{-3} s^{-1}] E_a/R: [K].

Reference	Reactions	A	β	-Ea/R	reaction orders
De Soete *	NH_3 + O_2 → NO + H_2O +1/2 H_2	4.0E6	0	16.1E3	$X_{NH_3}X_{O_2}^a$
1975 [27]	NH_3 + NO→ N_2 + H_2O +1/2 H_2	1.8E8	0	13.6E3	$X_{NH_3}X_{NO}$
Mitchell and Tarbell	NH_3 + NO→ N_2 + H_2O +1/2 H_2	6.22E14	0	27.68E3	$[NH_3][NO] \cdot RT/P$
1982 [28]	NH_3 + O_2 → NO + H_2O +1/2 H_2	3.48E20	0	50.33E3	$[NH_3][O_2]$
**	r_{den}=P/RT + 6.9E-6 exp(-21.13E3/T)·$[O_2]$				
Duo et al.	NH_3 + 5/4 O_2 → NO + 3/2 H_2O	2.21E14	0	75.79E3	$[NH_3]$
1993 [29]	NH_3 + NO + 0.25 O_2→ N_2 + 3/2 H_2O	1.80E8	0	27.00E3	$[NH_3][NO]$
Jensen et al.	NH_3 + 5/4 O_2 → NO + 3/2 H_2O	5.07E14	0	35.23E3	$[NH_3][O_2]$
1995 [30]	NH_3 + NO + 0.25 O_2→ N_2 + 3/2 H_2O	1.11E12	0	27.68E3	$([NH_3][NO][O_2])^{0.5}$
Brouwer et al.	NH_3 + O_2 → NO + H_2O + H	3.5E-1	7.65	63.06E3	$[NH_3][O_2]$
1996 [31]	NH_3 + NO→ N_2 + H_2O + H	4.24E2	5.3	42.07E3	$[NH_3][NO]$
***	S(CO)=17.5·ln(X_{CO})-68				
Brink et al.	NH_3 + O_2 → NO + H_2O +1/2 H_2	1.21E2	2	8.0E3	$[NH_3][O_2]^{0.5}[H_2]^{0.5}$
2001 [32]	NH_3 + NO→ N_2 + H_2O +1/2 H_2	8.73E11	-1	8.0E3	$[NH_3][NO]$

* The reaction order for the mechanism proposed by De Soete [27] is given in mole fraction, not in concentration as the other models. The oxygen reaction order, a,is uniquely related to the oxygen mole fraction - for the specific correlation see [27, 33]

** The rate equation for the second reaction in Mitchell and Tarbell [28] is expressed as:

$$r = \frac{A \cdot exp\left(\frac{-E_a}{RT}\right)[NH_3][O_2]}{r_{den}}$$

*** S(CO) is an empirical adjustment of the temperature to adjust for the effect of CO on the radical concentration. X_{CO} is the CO concentration in ppm, in Brouwer et al. [31] the rate expressions take the form:

$$r = A \cdot (T + S(CO))^{\beta} exp\left(\frac{-E_a}{R(T - S(CO)}\right)$$

De Soete was one of the first to propose a global reaction mechanism for NO_X formation, the mechanism is based on experimental measurements from ammonia doped CH_4/O_2/He flat premixed flames at stoichiometric ratios from 0.6 to 1.5 and temperatures of 1800-2400K. The mechanism of DeSoete is the default fuel NO mechanism in Fluent [33] for the case of gaseous fuels with ammonia or HCN as the intermediate N compound.

The mechanism by Mitchell and Tarbell [28] is developed based on experimental data from flow reactor experiments and jet stirred reactor experiments at stoichiometric conditions from $0.9< \lambda < 1.5$ and temperatures from 700-1930 K. The reactions are part of a larger mechanism for pulverized coal combustion.

The mechanism developed by Duo et al. [29] is fitted to experimental data for SNCR processes in a flow reactor with 4 % O_2 at temperatures 1140-1335 K.

Jensen et al. [30] modified the rate expression from Duo et al. making the mechanism suitable for varying air excess ratios in the temperature window 923-1373 K, the rate constants expressed in table 6.1 from Jensen et al. is with the lower activation energies valid for combustion conditions [30].

The mechanism of Brouwer et al. [31] actually also consists of subsets for urea and HNCO, but in table 6.1 only the NH_3 oxidation reactions are presented. The mechanism is developed based on a detailed mechanism and is

validated against experimental data for SNCR conditions, i.e. fuel lean conditions in the temperature window 1100-1400K. The mechanism is capable of taking into account the change in selectivity towards NO formation with increasing CO concentration [31].

Brink et al. [32] developed their model based on CSTR comparisons with a detailed mechanism. The mechanism was evaluated in the temperature window 900-1900K under flame like (high initial fuel, CO and H_2, air content with 1000 ppm NH_3) and flue-gas like combustion conditions (low fuel content, 1000 ppm NH_3 or 500 ppm NO and 500 ppm NH_3). The mechanism was compared to that of Mitchell and Tarbell [28] , and it is claimed that the mechanism of Brink et al. is superior at flame like conditions, whereas the mechanism of Mitchell and Tarbell performs better in flue gas (or SNCR) like conditions [32].

Norstrom et al. [34] compared the mechanisms of Mitchell and Tarbell, Brouwer et al., Jensen et al. and Duo et al. with a detailed mechanism. The mechanisms were tested at CSTR conditions with a residence time of 0.1-100ms for both fuel rich and fuel lean conditions in the temperature window 800-1500°C. The simple mechanisms did in general not compare well with the detailed mechanism, especially under fuel rich conditions. None of the simple mechanisms was labeled as suitable as a general mechanism to model the nitrogen chemistry in a CFD simulation of a biomass furnace [34].
Pedersen et al.[35] also compared global fuel NOx models and reached a similar conclusion that outside their region of validation, the global mechanisms

should be used with care.

Instead Pedersen et al. reduced the Nitrogen chemistry from a detailed mechanism intended for coal combustion modeling, so that only HCN, NH_3 and. The mechanism is based on steady state assumptions for all important radical species but H, OH and O. This means that input data required are H, OH and O as well as major combustion species as CO, CO_2 H_2, H_2O and N_2. The reduced nitrogen mechanism includes thermal NO formation, but not hydrocarbon-N interactions as reburning and prompt NO, it is reported not to be applicable for SNCR conditions [35].

6.6 CFD modeling of NOx formation

CFD modeling is often applied to large scale industrial furnaces with the intension of optimizing or retrofitting fuel air distributions. When predicting pulverized fuel systems a lot of effort is put into the multiphase and devolitalization modeling. For grate fired systems the boundary condition at the grate is a crucial parameter, that can be difficult to handle satisfactorily. Prediction of NO formation and destruction is challenging and the nitrogen chemistry is quite complex, as described in the preceding chapters. Nevertheless several researchers have conducted modeling of NO_X formation and reduction with successful results. In general the validation data available from industrial combustion facilities is limited to exit concentrations, and maybe a few in furnace measurements close to the walls. CFD modeling of NO_X formation and reduction from lab and pilot scale flames and furnaces have also been reported and most of the published work is summarized in

Table 6.2.

When using CFD modeling to predict NO_X formation a Post-Processing approach is often taken. The post processing approach implies that the nitrogen chemistry does not affect the overall flow pattern and temperature. This is a reasonable assumption since only a small fraction of the overall gas flow is involved. The solution procedure is then to solve to convergence of the main scalars being: velocity, temperature and concentration of major species. NO_X is afterwards modeled as a post-processing task. However, low concentrations of trace species including NO have been seen to affect emissions and combustion rates [36]. It can however be dangerous to decouple the combustion process and especially the fuel-N formation, since fuel-N oxidation is competing with the major fuel combustion for the available O_2. This could imply that even though the Nitrogen chemistry does not affect the main combustion process in a significant extent due to the low concentrations, the availability of excess O_2 for the Ammonia oxidation mechanism can be largely affected by letting the combustion mechanism consume O_2 initially before post-processing a fuel-N mechanism.

The following chapters will describe some of the work carried out in the area of CFD modeling to elaborate on Table 6.2.

Post-processing of detailed chemistry an approach taken by Rasmussen et al. when modeling soot formation.[37] The main idea behind this method involved a pre-processing step, where three types of information were ex-

tracted from the CFD solution: (1) the applied boundary conditions, type and the relative position of all cells, (2) the gross mass transfer coefficients across all cell surfaces, (3) the cell centered values of T, P, Y_i, k, ϵ and FA (a fluid age). After this each cell was treated as a perfectly stirred reactor, however the volume of the reactor did not necessarily equal the volume of the cell. A part of the cell may be left inert if the oxygen concentration is significant. The reactor volume was instead estimated from the mass fraction of fine turbulent structures in the cell - the same idea as for the Eddy Dissipation Concept, the remaining part of the cell was treated as an inert volume. Figure 6.6 displays the conversion from cell to PSR reactor. [37]

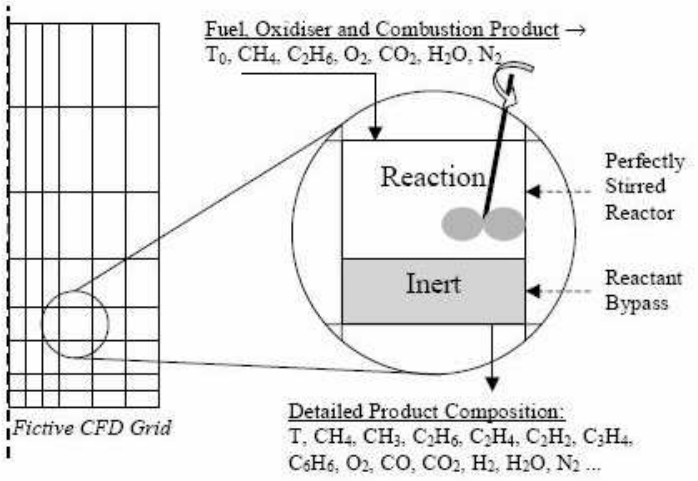

Figure 6.6: Schematic illustration of the PSR approach used to model each cell by Rasmussen et al. [37]

A similar approach has been used by Stefanidis et al. [38] to succesfully model a steam cracking furnace and by Widmann et al. [39] in the modelling af a 440 kW grate fired biomass pilot plant. Widmann et al. applied the Eddy Dissipation Model for calculation of the basic gas phase species. Afterwards

the NOx chemistry was modeled in a post-processing mode using detailed chemistry with the Eddy Dissipation Concept.[39]

Ehrhardt and coworkers [40] were among the first to define a network of ideal reactors based on an output of a simple decoupled CFD scalar field. They then divided the computational volume into areas of ideal plug flow reactors, and calculated an applied detailed kinetic mechanism to the plug flow network. The approach used by Ehrhardt and coworkers is illustrated in figure 6.7.

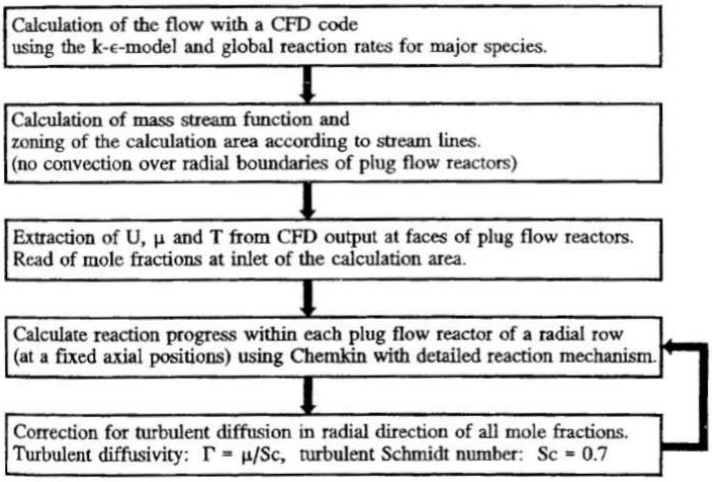

Figure 6.7: Scheme of the modeling concept used by Ehrhardt et al.[40]

Inspired by the zone model, a joint Italian group from Milano and Pisa developed a new ideal reactor network modeling concept named SFIRN (Simplified Fluidynamic by Reactor Network) [41]. The SFIRN approach is based on a two step procedure. Starting from the complex flow, temperature and stoichiometry fields computed from 3D CFD simulation a simplification is made, where the furnace is divided into a network of ideal reactors; either plug flow or perfectly stirred reactors. This is exemplified in figure 6.8.

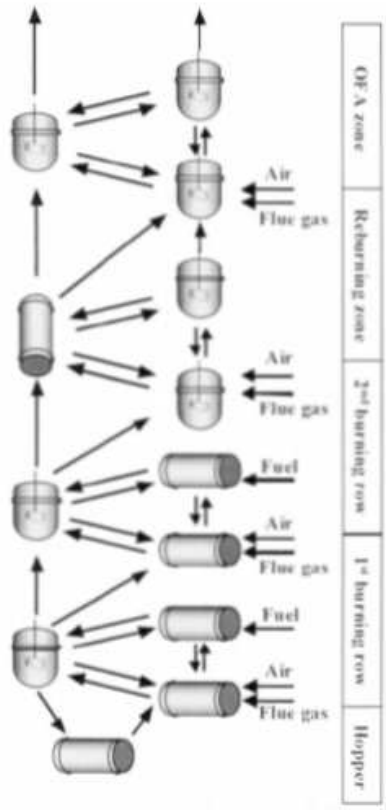

Figure 6.8: Ideal reactor network representing a 75 MWe furnace. [41]

The reactor is considered plug flow when a prevalent streamline is present in the cell region covered by the reactor, otherwise it is assumed as PSR. Figure 6.9 illustrates how the velocity vectors decide the ideal reactor configuration. The temperature in the isothermal ideal reactors is evaluated as an average of the cell temperatures using a proper weight of the NOx formation contribution of each cell.

The authors report that the definition of number, type and connections of the ideal reactors together with their operating conditions is the critical step of the procedure. The correspondence of the ideal reactor network flow field with the real flow field is verified by comparing residence time distributions

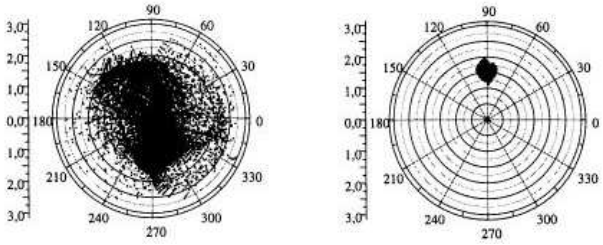

Figure 6.9: Polar and sagittal angles of velocity vectors right: PFR left: PSR [41]

between the CFD solution and the network solution.

This SFIRN procedure has lead to several papers reporting successful modeling of large scale furnaces [42, 41, 43, 44] Also the modeling of a thoroughly investigated pilot flame (TECFLAM) for CFD validation has been performed with the SFIRN approach. [45]

Niksa and Liu [46] also post-processed detailed reaction mechanisms to CFD flow field solutions from the modeling of pulverized coal flames in a simple flow reactor. The approach was basically identical to that used in the references above; based on the CFD simulation the computational domain was divided into regions and characterized with one-dimensional average profiles of temperature and residence time and a residence time distribution, which were used to specify a reactor network for the entire flow, hence major species concentrations were not fixed by the rudimentary CFD pre-step. Finally the detailed chemistry was applied across all reactors in the network (tank stirred reactors were used). However the chemistry model in this work was quite extensive since it takes into consideration devolitalization, carbon burnout, gas phase reactions and soot effects. [46] This approach does not succeed in capturing all underlying trends from the models used, for instance the CO concentration is underpredicted, while the N-conversion was nicely predicted.

The approach is an interesting attempt to try to capture many interacting effects (as N-soot effects) using the same modeling scheme.
Widmann et al. [39] took a slightly different approach in the modeling af a 440 kW grate fired biomass pilot plant. The researchers applied an ordinary Eddy Dissipation Model for calculation of the basic gas phase species, afterwards NOx chemistry was modeled in a post-processing mode using detailed chemistry with the Eddy Dissipation Concept. It resulted in a quantitative prediction of the NO_X emission.[39]
Even though impressive predictions of NO formation has been obtained using the post-processing of detailed chemistry approach, simple mechanisms are often being applied with succes as well.

Recently Saario and Oksanen [47] performed a CFD analysis of the freeboard and SNCR processes above a 40 MW bubbling biomass and sludge bed. Evaluation of the simple NH_3 oxidation mechanisms of Duo et al. [29], Brouwer et al.[31], Mitchell and Tarbell [28] and Brink et al. [32] was performed using a post-process approach. The authors stress that the mechanisms are not valid for condition beyond where they are developed, and no mechanism was found suitable for both the near bed combustion conditions and the SNCR conditions. The authors finally chose to apply the mechanism by Brink et al. [32] in the near bed region and the mechanism by Duo et al. [29] in the SNCR region.[47]

Klason and Bai [48] reported very good agreement between measured and predicted NO emissions from a 20 MW grate fired wood pellet furnace, de-

spite using global three step mechanisms for fuel-NO (Brink et al. [32]) and thermal NO. The authors apply a presumed PDF on the temperature for modeling thermal NO, while standard Eddy Dissipation Concept modeling was applied for the fuel NO. They predict around 60% of the NO formed to the thermal and thermal-N_2O pathways.

Ma et al. [49] modeled a 1 MW pulverized biomass test facility. Global mechanisms were applied for fuel NO in both a HCN and NH_3 pathway (DeSoete [27]. The authors post-processed the NO chemistry on a solution based on Eddy Dissipation modeling. The HCN pathway yields underestimated the NO emission and the NH_3 pathway overestimated the NO emission, so a properly chosen distribution of N - intermediates being HCN and NH_3 respectively resulted in an accurate prediction of the NO emission.

Yang et al. [50] modeled a 38MWe grate fired straw furnace. They also post processed the global De Soete mechanism on a eddy dissipiation combustion solution and obtained impressive agreement between predicted and measured NO emissions.

Several researchers have successfully modeled NO emissions from pulverized coal combustion. Xu et al. [51] and Diez et al. [52] used Eddy Dissipation gas phase chemistry modeling along with post processing of a simple fuel NO mechanism. Le Bris et al. [53] and Visona et al. [54] also used global NO chemistry, but post-processed on a mixture-fraction - equilibrium CFD solution. As did Sheng et al. [55] in the modeling of a pulverized coal swirl burner.

Brink et al. [56] used the EDC approach along with a skeletal combustion mechanism and detailed fuel NO mechanism to model the NO_X formation from combustion of a gasifier gas in a pilot combustor. They argued for not applying a post-process approach since a simpler model would not accurately predict the temperature in the fine structures and the skeletal mechanism required solution and the skeletal mechanism applied required solving in a fully coupled way. Also this approach resulted in a very accurate prediction of the NO emission at two different air excess levels.[56] Miltner et al. [57] also used the EDC approach without post-processing but with global gas phase chemistry to model a biomass pilot plant. The authors did not present their NO predictions but stated that NO emissions was underpredicted probably due to insufficient homogeneous NO modeling.[57]

Reference	Combustion facility	Turbulence model	Turbulence - Chemistry approach	NOx mechanism	Post-processing	NO Result/ conclusions
[48]	20 MW grate fired wood pellet furnace	Standard k-ϵ	EDC	global HCN-NH3 Thermal NO,N2O	No	Fairly good agreement mainly thermal NO
[49]	1MW biomass test facility	RNG k-ϵ	EDM	Global mechs (De Soete [27])	No	Reasonable agreement with exit conc.- little validation
[50]	38MW straw grate boiler	RNG k-ϵ	EDM	Global mechs (De Soete [27])	No	Reasonable agreement with exit conc.- little validation
[39]	440 kW grate fired biomass pilot plant	Realisable k-ϵ	EDM	Detailed (Kilpinen92)	Yes - EDC for postprocess	Reasonable agreement mainly Fuel NO
[56]	gasifier product gas pilot combustor	Standard k-ϵ	EDC skeletal CO mech.	Detailed - NH3 ox. mechanism	No	Very good agreement
[51]	350 MWe coal utility boiler	k-ϵ model	EDM	Global (DeSoete) fuel NO	Yes	Conclusion leakage important reasonable NO results
[47]	40 MW BFB biomass sludge boiler	Modified k-ϵ	EDM postproces: EDC	Various simple NH3 ox models	Yes	Global models only valid in derived areas - reasonable agreement
[52]	600 MW coal utility boiler	Standard k-ϵ	Mixed is burnt (EDM)	Global - DeSoete Fuel NO	Yes	Reasonable agreement with exit conc.- little validation
[53]	600 MW coal power plant	Standard k-ϵ PDF - Equilibrium	Mixture fraction	Global mechs (De Soete)	Yes	Reasonable agreement with exit conc.- little validation
[58]	350 MWe tangentially fired coal plant	? not stated	2 part Mixture fraction equilibrium	not stated	not stated	Qualitative agreement
[55]	150 kW down fired p. coal swirl burner	Standard k-ϵ	2 part mixture fraction equilibrium and PDF	Global (De Soete)	yes	Impressive agreement with exit conc.
[59]	4 MWe gasifier gas turbine combustor	RSM/ Standard k-ϵ	Mixture fraction Laminar Flamelet	Global (Mitchell and Tarbell)	Yes	Reasonable agreement, trend not always captured, little validation
[57]	2 MW biomass pilot plant	SST k-ω	EDC	Simple two step (Brink 2001)	no	NO emissions underestimated
[54]	2.5 MW air staged coal burner	Standard k-ϵ	Mixture fraction PDF-Equilibrium?	Simple (DeSoete [27])	Yes	Quantitative agreement
[60]	500 MW oil boiler	Reynolds Stress Model	Mixture fraction Flamelet	Simple 2 step HCN ox. and thermal NO	Yes	Agreement with exit conc. Predicts fine trends for air excess and load variations
[40]	reburning from a 335 kW natural gas diffusion flame	Standard k-ϵ	EDM	Detailed	Yes Zone Model	In general very good
[42, 43]	320 MWe oil and steam opposite wall fired furnace	not stated	not stated	Detailed	Yes Ideal reactor network	Quantitative agreement with exit conc.
[41]	75MWe oil and gas fired furnace	not stated	not stated	Detailed	Yes Ideal reactor network	Quantitative agreement with exit conc.
[44, 43]	5 and 10MW glass melting natural gas fired	zero equation model -no influence of turbulence	only kinetics	Detailed	Yes Ideal reactor network	Quantitative agreement with exit conc.
[45]	300kW swirling natural gas flame	Standard k-ϵ	EDM/ Finite Rate	Detailed Ideal Reactor Network	Yes	Quantitative agreement predicts trends in validated flame mainly thermal NO
[46, 61]	Pulverized Fuel flow reactor (lab scale)	not stated	not stated	Detailed Ideal Reactor Network	Yes for various coal types	reasonable agreement
[38]	Naphta-methane steam cracking furnace	RNG k-ϵ	EDM and EDC	EDM=simple EDC=detailed	No	No validation measurements concludes EDC superior
[62]	Lab reburn flow reactor	Standard k-ϵ	EDC	reduced mechanism	No	Impressive agreement only reburning

It appears from Table 6.2 that no method is recognized as a superior and ideal approach to NO_X modeling. Most of the published work contain examples of successful predictions of NO_X emissions, while only few works have been published where the NO_X modeling fails, even though these approaches also can be very valuable for future modelers. What makes CFD integrated NO_X modeling even more obscure is that many other parts of the modeling process, such as turbulence and radiation modeling can have a large influence on the NO emission predicted. This means that it is possible to obtain a good NO prediction with an invalid NO_X modeling approach as long as some of the other modeling aspects compensates for the error. Nevertheless it does seem possible to gain valuable insight in a combustion systems NO_X chemistry behavior through CFD analysis.

6.7 References

[1] Ya.B. Zeldovich, P.Ya. Sadovnikov, P. Ya, and D.A. Frank-Kamenetskii. Oxidation of nitrogen in combustion translated by M. Shelef, 1947.

[2] J.A. Miller and C.T. Bowman. *Prog. Energy Combust. Sci.*, 15:287–338, 1989.

[3] G. Löffler, R. Sieber, M. Harasek, H. Hofbauer, R. Hauss, and J. Landauf. *Fuel*, 85:513–523, 2006.

[4] J.W. Bozzelli and A.M. Dean. *Int. J. of Chem. Kin.*, 27:1097–1109, 1995.

[5] C. P. Fenimore. *Proc. Combust. Inst.*, pages 373–380, 1971.

[6] G.P. Smith. *Chem. Phys. Lett.*, 367:541–548, 2003.

[7] A. El Bakali, L. Pillier, P. Desgroux, B. Lefort, L. Gasnot, J.F. Pauwels, and I. da Costa. *Fuel*, 85:896–909, 2006.

[8] P. Glarborg, A.D. Jensen, and J.E. Johnsson. *Prog. Energy. Combust. Sci.*, 29:89–113, 2003.

[9] F. Tian, J. Yu, L.J. McKenzie, J. Hayashi, and C. Li. *Energy Fuels*, 21:517–521, 2007.

[10] R.M. Heck. *Catalysis Today*, 53:519—-523, 1999.

[11] M.U. Alzueta, H. Rojel, P.G. Kristensen, P. Glarborg, and K. Dam-Johansen. *Energy and Fuels*, 11:716–723, 1997.

[12] L.D. Smoot, S.C. Hill, and H. Xu. *Prog. Energy Combust. Sci.*, 24:385–408, 1998.

[13] Duo Wenli. *Kinetic Studies of Reactions Involved in Selective Non-Catalytic Reduction in Nitric Oxide*. PhD thesis, Department of Chemical Engineering, Technical University of Denmark, Kgs. Lyngby, 1990.

[14] M.T. Javed, W. Nimmo, and B.M. Gibbs. *Chemosphere*, 70:1059–1067, 2008.

[15] G. Stubenberger, R. Scharler, S. Zahirovic, and I. Obernberger. *Fuel*, 87:783–806, 2008.

[16] A.E. Lutz, R.J. Kee, and J.A. Miller. *Senkin: A Fortran Program for Predicting Homogeneous Gas Phase Chemical Kinetics With Sensitivity Analysis*. Sandia Report SAND87–8248·UC–401, Sandia National Laboratories, Livermore, CA, USA, 1990.

[17] P. Glarborg, M.U. Alzueta, K. Dam-Johansen, and J.A. Miller. *Combust. Flame*, 115:1–27, 1998.

[18] J.G. Jacobsen C.L. Rasmussen and P. Glarborg. *Int. J. Chem. Kin*, 40:778–807, 2008.

[19] P. Glarborg and L.B. Bentzen. *Energy Fuels*, 22:291–296, 2008.

[20] P.J. Gimenez, C.L. Rasmussen, M.U. Alzueta, P. Marshall, and P. Glarborg. *Proc. Combust. Inst.*, 32:367–375, 2009.

[21] P. Kilpinene Ø. Skreiberg and P. Glarborg. *Combust. Flame*, 136:501–536, 2004.

[22] P. Dagaut, P. Glarborg, and M.U. Alzueta. *Prog. Energy Combust. Sci.*, 34:1–46, 2008.

[23] C.L. Rasmussen, A.E. Rasmussen, and P. Glarborg. *Combust. Flame*, 154:529–545, 2008.

[24] R.P. van der Lans, L.T. Pedersen, A. Jensen, P. Glarborg, and K. Dam-Johansen. *Biomass and Bioenergy*, 19:199—-208, 2000.

[25] R. Salzmann and T. Nussbaumer. *Energy Fuels*, 15:575—-582, 2001.

[26] G. Di Nola and H Spliethoff. *Clean Air*, 8:199—-220, 2007.

[27] G.G De Soete. *Proc. Combust. Inst.*, 15:1093–1102, 1975.

[28] J.W. Mitchell and J.M. Tarbell. *AIChe Journal*, 28:302–311, 1982.

[29] W. Duo, K. Dam-Johansen, and K. Østergaard. *The Canadian Journal of Chemical Engineering*, 70:1014–1020, 1993.

[30] A. Jensen, J.E. Johnsson, J. Andries, K. Laughlin, G. Read, M. Mayer, H. Baumann, and B. Bonn. *Fuel*, 74:1555–1569, 1995.

[31] J. Brouwer, M.P. Heap, D.W. Pershing, and P.J. Smith. *Proc. Combust. Inst.*, 26:2117–2124, 1996.

[32] A. Brink, P. Kilpinen, and M. Huppa. *Energy Fuels*, 15:1094–1099, 2001.

[33] Fluent inc., Centerra Resource Park, 10 Cavendish Court, Lebanon, NH 03766. *Fluent 6.2 users guide*, 2005.

[34] T. Norstrom, P. Kilpinen, A. Brink, E. Vakkilainen, and M. Huppa. *Energy Fuels*, 14:947–952, 2000.

[35] L.S. Pedersen, P. Glarborg, and K. Dam-Johansen. *Combust. Sci. Technol.*, 131:193–196, 1998.

[36] P. Glarborg. *Proc. Combust. Inst.*, 31:77–98, 2007.

[37] M.S. Skjøth-Rasmussen, O. Holm-Christensen, M. Østberg, T.S. Christensen, T. Johannesen, A.D. Jensen, P. Glarborg, and H. Livbjerg. *Computers and Chemical Engineering*, 28:973–990, 2004.

[38] G.D. Stefanidis, B. Merci, G.J. Heynderickx, and G.B. Marin. *Computers and Chemical Engineering*, 30:635–649, 2006.

[39] E. Widmann, R. Scharler, G. Stubenberger, and I. Obernberger. *2nd world conference on biomass for energy, industry and climate protection*, 2, 2004.

[40] K. Ehrhardt, M. Toqan, P. Jansohn, J.D. Teare, J.M. Beer, G. Sybon, and W. Leuckel. *Combust. Sci. Technol.*, 131:131–146, 1998.

[41] T. Faravelli, L. Bua, A. Frassoldati, A. Antifora, L. Tognotti, and E. Ranzi. *Computers and Chemical Engineering*, 25:613–618, 2001.

[42] D. Benedetto, S. Pasini, M. Falcitelli, C. La Marca, and L. Tognotti. *Combust. Sci. Technol.*, 153:279–294, 2000.

[43] M. Falcitelli, S. Pasini, and L. Tognotti. *Computers and Chemical Engineering*, 26:1171–1183, 2002.

[44] M. Falcitelli, S. Pasini, N. Rossi, and L. Tognotti. *Applied Thermal Engineering*, 22:971–979, 2002.

[45] A. Frassoldati, S. Frigerio, E. Colombo, F. Inzoli, and T. Faravalli. *Chem. Eng. Sci.*, 60:2851–2869, 2005.

[46] S. Niksa and G.-S. Liu. *Proc. Combust. Inst.*, 29:2259–2265, 2002.

[47] A. Saario and A. Oksanen. *Energy Fuels*, 22:297–305, 2008.

[48] T. Klason and X.S. Bai. *Fuel*, 86:1465–1474, 2007.

[49] L. Ma, J.M. Jones, M. Pourkashanian, and A. Williams. *Fuel*, 86:1959–1965, 2007.

[50] Y.B. Yang, R. Newman, V. Sharifi, J. Swithenbank, and J Ariss. *Fuel*, 86:129—-142, 2007.

[51] M. Xu, J.L.T. Azevedo, and M.G. Carvalho. *Fuel*, 79:1611–1619, 2000.

[52] L.I. Diez, C. Cortes, and J. Pallares. *Fuel*, 87:1259–1269, 2008.

[53] T. Le Bris, F. Cadavid, S. Caillat, S. Pietrzyk, J. Blondin, and B. Baudoin. *Fuel*, 86:2213–2219, 2007.

[54] S.P. Visona and B.R. Stanmore. *Chem. Eng. Sci.*, 53:2013–2027, 1998.

[55] C. Sheng, B. Moghtaderi, R. Gupta, and T.F. Wall. *Fuel*, 83:1543–1552, 2004.

[56] A. Brink, M. Huppa, E. Kurkela, and M. Suomalainen. *Prog. Comp. Fluid Dynamics*, 6:217–225, 2006.

[57] M. Miltner, A. Makaruk, M. Harasek, and A. Friedl. *Clean Techn. Environ. Policy*, 10:165–174, 2008.

[58] R.I. Backreedy, J.M. Jonesa, L. Maa, M. Pourkashaniana, A. Williams, A. Arenillasb, B. Ariasb, J.J. Pisb, and F. Rubiera. *Fuel*, 84:2196–2203, 2005.

[59] B. Adouane, P. Hoppesteyn, W. de Jong, M. van der Wel, K.R.G. Hein, and H. Spliethoff. *Fuel*, 83:1543–1552, 2004.

[60] C. Hochenhauer and G. Brandstetter. *Chem. Eng. Sci.*, 53:2013–2027, 1998.

[61] S. Niksa and G.-S. Liu. *Fuel*, 81:2371–2385, 2002.

[62] F. Liesa, M.U. Alzueta, A. Millera, and R. Bilbao. *Energy Fuels*, 19:833–841, 2005.

Chapter 7

NO modeling results

This chapter includes a paper which is published in the journal "Energy and Fuels". It contains the main results for CFD modeling of NO formation and comparison with experimental measurements. The modeling results are based on the results in chapter 5. The paper also includes a description of the experimental setup, which is omitted here (chapter 2 describes the experimental setup in detail. Examples of the user defined functions along with a brief implementation guideline can be found in appendix D

Experimental and numerical investigation of gas phase freeboard combustion. Part II: Fuel-NO formation

Jimmy Andersen[1], Peter Arendt Jensen*, Søren Lovmand Hvid[2], and Peter Glarborg[1,*]

1: Department of Chemical and Biochemical Engineering
Technical University of Denmark, DK-2800 Kgs. Lyngby, Denmark

2: DONG Energy, Kraftværksvej, DK-7000 Fredericia, Denmark

*: Corresponding author: pgl@kt.dtu.dk

7.1 abstract

In part I of the present work, experimental data and CFD modeling predictions for velocity field, temperatures, and major species were compared for a 50 kW axisymmetric, non-swirling natural gas fired combustion setup, constructed to simulate the conditions in the freeboard of a grate fired boiler. Here, in part II, the ability of CFD to predict volatile-N oxidation to NO and N_2 is evaluated. Trace amounts of ammonia were added to the natural gas and local measurements of NH_3 and NO in the reactor were compared to modeling predictions. Different modeling approaches, including global schemes and analytically reduced mechanisms, were tested in the CFD calculations. In addition, the simplified schemes were compared to reference calculations with a detailed mechanism under isothermal plug flow reactor conditions.

While none of the global ammonia schemes were able to provide satisfactory predictions over a wider range of conditions, an analytically reduced nitrogen scheme generally provided a satisfactory agreement with the detailed mechanism. Application of the selected schemes in a CFD analysis showed that both the standard Fluent post-processing approach with the De Soete global scheme and the combination of a skeletal combustion mechanism with the analytically reduced N-scheme provided a reasonable agreement with the experimental data. Most of the tested ammonia oxidation schemes were able to qualitatively predict the trends in NO formation going from one operational case to the other, but the main combustion solution on which the ammonia oxidation was based, proved to have a large impact on the quantitative NO prediction.

Keywords: Combustion, CFD, validation, freeboard, ammonia oxidation, fuel-NO

7.2 Introduction

The formation of NO from fuel nitrogen sources is a common concern in combustion. Most solid fuels contain significant amounts of nitrogen, which will be released during devolatilization and char burnout. For biomass fuels significant amounts of NH_3 may be released during devolatilization [1], while for coal and higher ranked fuels, the fuel bound nitrogen is primarily released as HCN. The reason for this difference is that nitrogen in coals are typically bound in aromatic carbon structures, whereas nitrogen in biomass is more likely to be found in amine or amide structures [2]. When the fuel nitrogen constituents are released they will participate in gas phase reactions to form either NO or N_2. The selectivity of the oxidation process implies that with proper combustion conditions during the fuel-N conversion, it is possible to minimize the NO formation.

Although significant efforts have been aimed at modeling and understanding NO formation and destruction, it remains a challenge to quantitatively predict NO emissions from large combustion systems. This is due to local changes in temperature and oxygen concentration, which affect the nitrogen chemistry selectivity, as well as the complexities of modeling turbulence/-chemistry interactions.

Modeling the oxidation of ammonia is an important task in order to quantify the amount of fuel-NO formed in solid fuel fired systems. Several comprehensive mechanisms that include ammonia oxidation are available in the literature, e.g. [3, 4, 5, 6]. However it is often chosen in CFD modeling to use a global mechanism to reduce the computational load. Table 6.1 summarizes some of the global mechanisms available in the literature (see page 86.

Global schemes developed to predict volatile-N oxidation in combustion include those of De Soete [7], Mitchell and Tarbell [8], and Brink et al. [9]. De Soete [7] (DS) was among the first to propose a global reaction mechanism for NO formation. The mechanism was based on measurements from ammonia doped CH_4/O_2/He flat premixed flames at excess air ratios (λ) from 0.67 to 1.7 and temperatures of 1800-2400 K. The DS mechanism is the default volatile-NO mechanism in Fluent [13] for NH_3 or HCN as the intermediate N compound.

The mechanism by Mitchell and Tarbell [8] (MT) was developed based on experimental data from flow reactor experiments and jet stirred reactor experiments at stoichiometries of $0.9< \lambda <1.5$ and temperatures in the range 700-1930 K. The reactions were part of a larger mechanism for modeling of pulverized coal combustion.

Brink et al. [9] developed an ammonia oxidation mechanism based on perfectly-stirred reactor (CSTR) comparisons with a detailed mechanism. The mechanism was evaluated in the temperature window 900-1900K under flame like (high initial fuel, CO, H_2 and air content with 1000 ppm NH_3) and flue-gas like combustion conditions (low fuel content, 1000 ppm NH_3 or 500 ppm NO / 500 ppm NH_3). The mechanism was found to be superior to that of Mitchell and Tarbell [8] at flame like conditions, whereas the MT mechanism performed better in flue gas like conditions [9].

In addition to these mechanisms, simplified schemes have been developed to describe selective non-catalytic reduction (SNCR) of NO by NH_3 or other additives. The mechanism by Duo et al. [10] was limited to conditions with 4% O_2 at temperatures of 1140-1335 K. Jensen et al. [11] modified this scheme

to allow for varying excess air ratios in the temperature window 923-1373 K. The mechanism of Brouwer et al. [12], developed for the temperature window 1100-1400 K, consisted of subsets for urea and HNCO in addition to NH_3, but in Table 6.1 only the NH_3 scheme is listed. It is capable of taking into account the change in selectivity towards NO formation with increasing CO concentration [12].

Pedersen et al. [14] and Norström et al. [15] compared selected global schemes with reference calculations with detailed reaction mechanisms under CSTR conditions over a range of conditions. In both studies, it was concluded that the global schemes did not compare well with the reference calculations, especially under fuel-rich conditions, and that they should be used with care outside their region of validation. Despite these short-comings, several CFD modeling studies have applied the simple global schemes with some success. [16, 17, 18, 19, 20, 21, 22, 23] More elaborate schemes for nitrogen chemistry, based on analytical reduction of detailed mechanisms, have been proposed, e.g. [14, 24]. Even though the analytically reduced schemes provide a better description of NO formation, their use has so far been limited since they are computationally more demanding and rely on input estimates of combustion intermediates.

The objective of the present work is to supply validation data for modeling the volatile-N oxidation taking place in the freeboard section of a grate fired boiler. To provide well-defined boundary and reaction conditions, the freeboard section is approximated by a 50 kW axisymmetric non-swirling natural gas fired combustion setup (described in part I of the present work [25]). Measuring data for local concentrations of NH_3 and NO have been

obtained and compared to CFD modeling predictions, using the commercial CFD code FLUENT 6.3 [13]. The work addresses the validity of the commonly applied post-processing approach of nitrogen chemistry. It also tests the performance of selected global and analytically reduced ammonia oxidation schemes against calculations with a detailed reaction mechanism under plug-flow conditions.

7.3 Mechanism comparison

In this section several ammonia oxidation mechanisms are tested against a detailed chemical kinetic model (DCKM). The chosen detailed mechanism [6, 26] consisted of oxidation subsets for CH_4 and NH_3, together with subsets describing hydrocarbon/nitrogen interactions and thermal NO formation. In order for the global schemes tested in this section to be comparable with the full mechanism, they were all extended with a mechanism for thermal NO formation (see Table 7.1).

Table 7.1: The Thermal NO reaction mechanism with forward and reverse rate constants [27] (units in m, s, mol, K). A quasi steady state assumption of the N radical concentration is applied, which yields the following expression for the thermal NO rate: $\frac{dNO}{dt} = 2k_{f,1}[O][N_2]\left(1 - \frac{k_{r,1}k_{r,2}[NO]^2}{k_{f,1}[N_2]k_{f,2}[O_2]}\right) / \left(1 + \frac{k_{r,1}[NO]}{k_{f,2}[O_2]+k_{f,3}[OH]}\right)$. The O and OH radical concentrations are determined from a partial equilibrium approach [13, 28].

#	Reaction	k_f	k_r
1	$O + N_2 \rightarrow NO + N$	1.8E08 exp(-38370/T)	3.8E07 exp(-425/T)
2	$N + O_2 \rightarrow NO + O$	1.8E04 exp(-4680/T)	3.8E03 exp(-20820/T)
3	$N + OH \rightarrow H + NO$	7.1E07 exp(-450/T)	1.7E08 exp(-24560/T)

Isothermal plug flow reactor modeling was applied to test the performance of the global ammonia oxidation mechanisms of De Soete [7] (DS), Mitchell and Tarbell [8] (MT), and Brink et al. [9] (Brink) - see Table 6.1. These schemes were chosen because they were developed for combustion conditions and expected to apply over a wider range of conditions than the SNCR schemes. In Figures 7.1 to 7.2 the global ammonia oxidation schemes are solved in conjunction with the four step combustion mechanism of Jones and Lindstedt [29] (JL). The results of a DCKM calculation are also included in

the figures. The predicted O_2 decline (the top section of the figures) indicates that the JL mechanism ignites earlier than the DCKM in all cases. This can be attributed to the requirement of a time for building up a radical pool in the detailed mechanism. The DS and MT mechanisms only require presence of O_2 to initiate the oxidation of NH_3; for this reason they are not dependent on formation of intermediate combustion species. Figure 7.1 shows that the DS mechanism is very slow compared to the other mechanisms, whereas the MT and Brink mechanisms predict ammonia oxidation to be faster than the fuel oxidation. At long residence times the MT and DS mechanisms reach reasonable agreement with the DCKM, whereas the Brink mechanism slightly overpredicts the NO formed in this case.

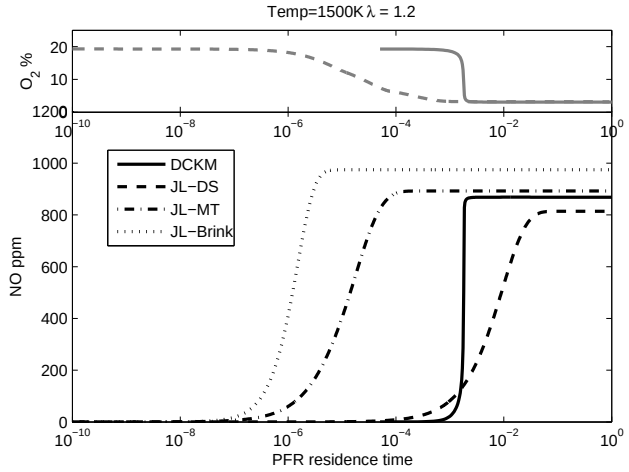

Figure 7.1: PFR comparison of NO concentrations from ammonia oxidation during methane combustion at 1500 K, fuel-lean stoichiometry ($\lambda = 1.2$) - 1000 ppm NH_3 in inlet. The upper part of the figure displays the O_2 concentrations predicted from the related combustion mechanisms.

Under reducing conditions (Figure 7.3), the DS mechanism barely starts to

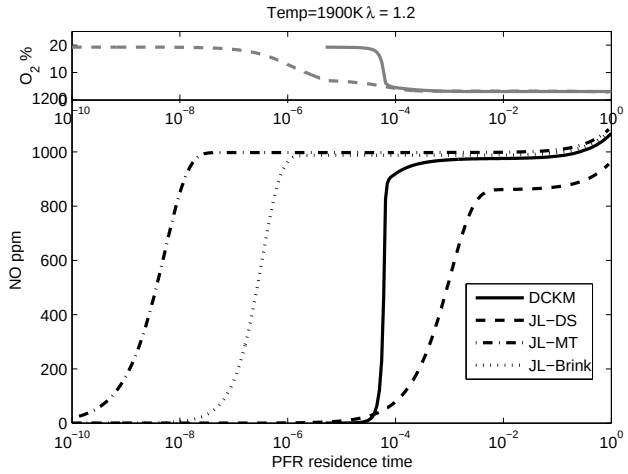

Figure 7.2: PFR comparison of NO concentrations from ammonia oxidation during methane combustion at 1900 K, fuel-lean stoichiometry ($\lambda = 1.2$) - 1000 ppm NH_3 in inlet. The upper part of the figure displays the O_2 concentrations predicted from the related combustion mechanisms.

form NO before the fuel has consumed all available O_2, thereby preventing further ammonia oxidation. This indicates that under fuel-rich conditions the DS mechanism is not applicable. Figure 7.2 shows that at high temperatures and oxidizing conditions the ammonia selectivity towards NO is almost 100%. The NO concentrations exceed 1000 ppm due to thermal NO formed at long residence times and high temperatures. The calculations display good agreement between the simple and detailed mechanism for the thermal NO formation.

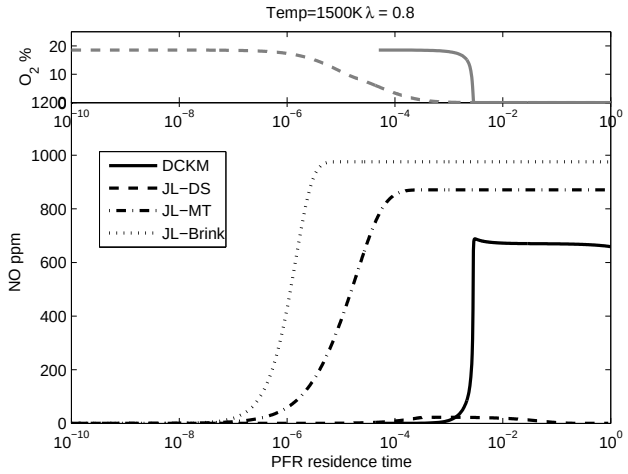

Figure 7.3: PFR comparison of NO concentrations from ammonia oxidation during methane combustion at 1500 K, fuel-rich stoichiometry ($\lambda = 0.8$) - 1000 ppm NH_3 in inlet. The upper part of the figure displays the O_2 concentrations predicted from the related combustion mechanisms.

An alternative to the global schemes for N-chemistry would be to use an analytically reduced scheme, such as that developed by Pedersen et al. [14] (LSP). The LSP scheme is based on steady-state assumptions for all important radical species but H, OH and O. It describes volatile-N oxidation (HCN, NH_3) and thermal NO formation, but not hydrocarbon-N interactions such as reburning and prompt NO. The required estimates for the O/H radical concentrations are not available from the combustion schemes typically applied in CFD. As a full detailed mechanism would be too comprehensive to use in CFD, we test the applicability of the 16 species, 41 reactions skeletal combustion mechanism by Yang and Pope [30] (SKEL).

In Figures 7.4-7.6, predictions of the LSP scheme in conjunction with SKEL and DCKM, respectively, are compared with calculations with the full mechanism under plug-flow reactor conditions. In the DCKM-LSP calculation, the DCKM nitrogen chemistry is replaced with that of LSP. SKEL provides a good prediction of the oxygen consumption rate under all three conditions. At the high temperature, lean conditions (Figure 7.6), the ignition timing is a bit shifted between the DCKM and SKEL mechanisms, but after ignition the profiles quickly match up. Regarding the NO formation, the predictions of the LSP scheme, both with SKEL (SKEL-LSP) and with DCKM (DCKM-LSP) compare well with those of the detailed mechanism. The thermal NO formation, which is important at long residence times, is also well captured by the LSP nitrogen mechanism (Figure 7.6). The DS global NO mechanism was also appended to the DCKM, but with a similar result as above; a too slow ammonia oxidation is predicted and in the fuel-rich case the ammonia is not converted to NO due to depletion of O_2.

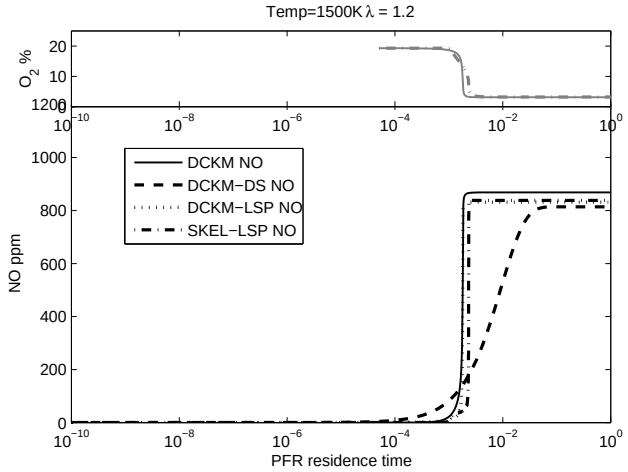

Figure 7.4: PFR comparison of NO concentrations from ammonia oxidation during methane combustion at 1500 K, fuel-lean stoichiometry ($\lambda = 1.2$) - 1000 ppm NH_3 in inlet, detailed mechanisms. The upper part of the figure displays the O_2 concentrations predicted from the related combustion mechanisms.

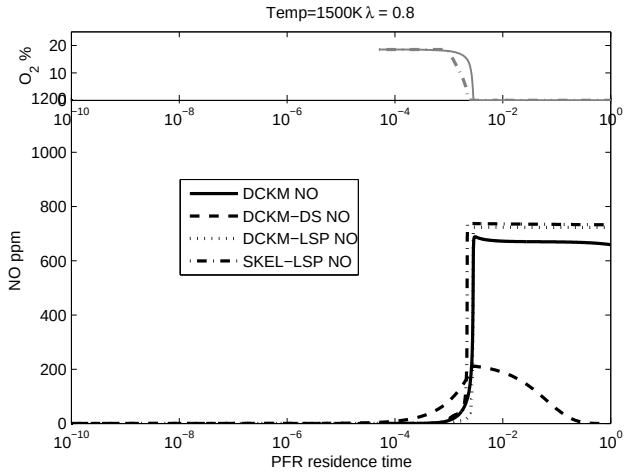

Figure 7.5: PFR comparison of NO concentrations from ammonia oxidation during methane combustion at 1500 K, fuel-lean stoichiometry ($\lambda = 0.8$) - 1000 ppm NH_3 in inlet, detailed mechanisms. The upper part of the figure displays the O_2 concentrations predicted from the related combustion mechanisms.

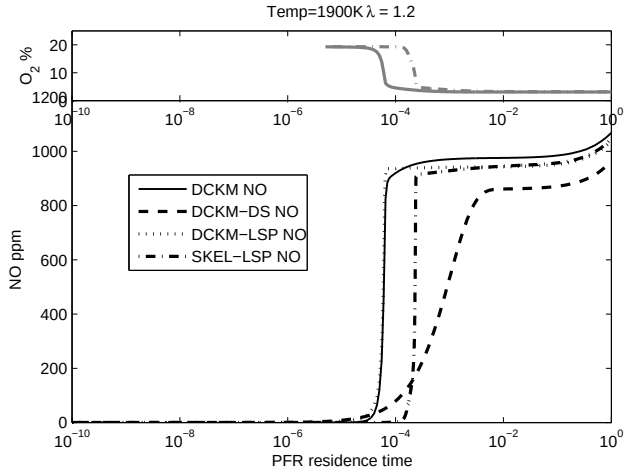

Figure 7.6: PFR comparison of NO concentrations from ammonia oxidation during methane combustion at 1900 K, fuel-lean stoichiometry ($\lambda = 1.2$) - 1000 ppm NH_3 in inlet, detailed mechanisms. The upper part of the figure displays the O_2 concentrations predicted from the related combustion mechanisms.

7.4 Experimental work

See chapter 2 on page 7.

7.5 CFD Modeling approach

The CFD solutions from the accompanying paper [25] were adopted in this work. The solutions were obtained using three combustion models: a two-step eddy dissipation approach (EDM), the four-step global mechanism by Jones and Lindstedt [29] (JL), and the skeletal mechanism [30] (SKEL). The solutions chosen for NO post-processing for the setting with maximal secondary air (setting 1) were the ones with frozen flow and turbulence fields from the EDM solution, where a reasonable agreement with local measurements were obtained. This means that the flow field for setting 1 was determined from the EDM solution, while gas concentrations and temperature were calculated with the JL or SKEL models within the Eddy Dissipation Concept (EDC) framework. The selected ammonia oxidation schemes were applied within the EDC framework and solved along with the species equations for the combustion species as well. The calculations were conducted in a semi-postprocessing mode, since all species but NO and NH_3 were heavily underrelaxed (practically frozen). Transport equations for the temperature and flow field were disabled.

For comparison, the standard Fluent NO_x approach was used. Here the DS fuel-N mechanism was enabled in a strict post-processing step. This approach implies that the nitrogen chemistry does not affect the overall flow pattern and temperature. Even though trace species including NO have been seen

to affect emissions and combustion rates [34], the assumption is justifiable since only a small fraction of the overall gas flow is involved in the active nitrogen chemistry. The solution procedure was then to solve initially the main scalars, i.e., velocity, temperature, and concentration of major species, and then NO was modeled as a post-processing task. Turbulent fluctuations were accounted for by applying probability density functions for temperature and O_2 concentration [13]. Also the LSP [14] scheme was tested in post-processing approach, using SKEL to describe the combustion.

7.6 Results and Discussion

Figures 7.7 and 7.8 show contour plots of measured and predicted NH_3 and NO concentrations for the conditions of setting 2. This setting allowed more detailed comparisons between experimental data and modeling predictions due to the prolonged flame compared to setting 1. The figure illustrates that the SKEL-LSP mechanism is the only model that provides a satisfactory prediction of the length of the NH_3-rich zone. The DS scheme predicts a considerably longer NH_3 oxidation zone than observed, while the MT scheme underpredicts the length of the zone. These trends are consistent with the PFR calculations that show the MT and Brink schemes to predict a faster NH_3 oxidation than the DS scheme.

The SKEL-LSP mechanism predicts reasonably well the NO levels in the fuel-rich regions of the flame (Figure 7.8). The global schemes predict no NO until sufficient oxygen is available to initiate the oxidation, even though some NO is present in the inlet gas. In the absence of oxygen, the only available reaction pathway of the global schemes involves reaction of NO with NH_3 to form

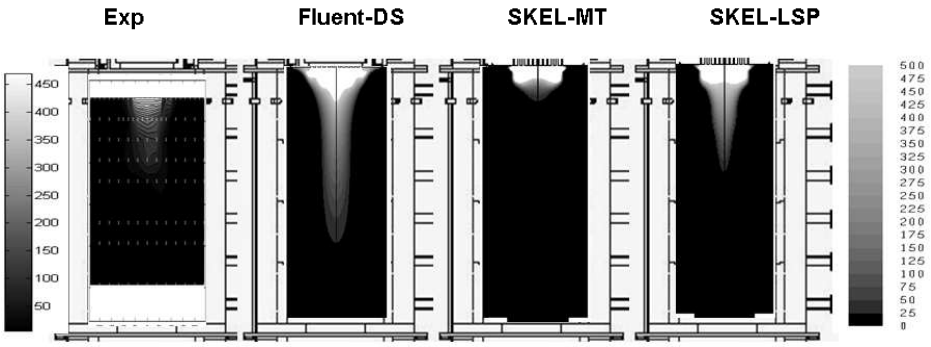

Figure 7.7: Contour plots of NH_3 concentrations (ppm) for the setting with low secondary air flow (setting 2). From left: Experimental, Fluent-DS, SKEL-MT, SKEL-LSP.

N_2. The exit NO concentration in the setting 2 case (measured 170 ppm) is slightly underpredicted by the Fluent-DS approach (149 ppm) and the SKEL-MT approach (129 ppm), while the SKEL-LSP approach overpredicts the formation (252 ppm). Figure 7.9 shows comparison of measured and calculated concentration profiles of NO and NH_3 for the setting 2 flame. None of the tested schemes provide a quantitative match with the experimental data in the traverse and axial locations compared. The Fluent-DS and SKEL-MT schemes show better agreement with the measured NO, except in the fuel-rich regions. The LSP mechanism does, however, capture the ammonia conversion zone better.

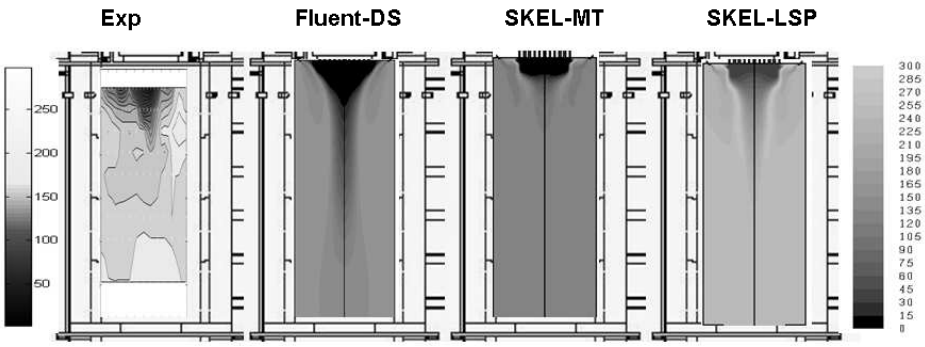

Figure 7.8: Contour plots of NO concentrations (ppm dry) for the setting with low secondary air flow (setting 2). From left: Experimental, Fluent-DS, SKEL-MT, SKEL-LSP.

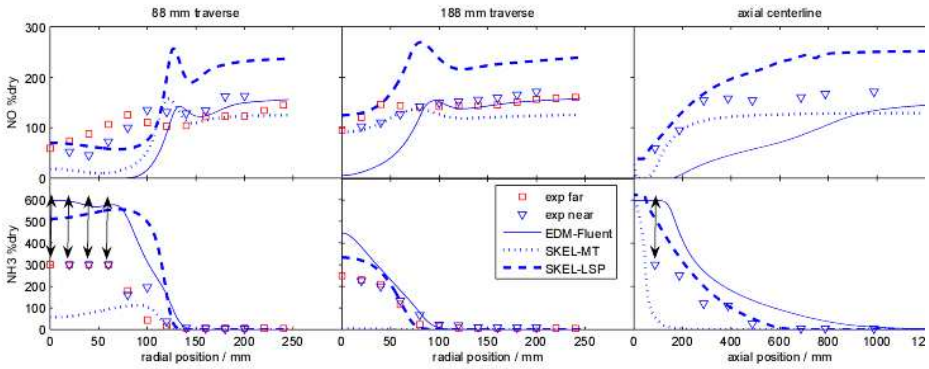

Figure 7.9: Comparison of measurement data and CFD predictions for NO and NH_3 at various positions in the setup. Setting 2 (low secondary air). Arrows indicate NH_3 range in measurement location, where the analyzer could not measure due to cross sensitivity. Near and far side labels refer to the location of the extraction probe insertion.

Figure 7.10 shows contour plots for the NO concentration for the conditions of setting 1. Here, the high secondary air flow results in a short flame, where most of the reaction is completed prior to the first measurement port. All the tested schemes are in qualitative agreement with the observations. The peak NO concentrations are observed just below the entrance to the freeboard section. Further downstream the formed NO is diluted with the added secondary air. The exit NO level predicted by the different ammonia mechanisms differ substantially, from 150 ppm by the Fluent-DS approach and 231 ppm from the SKEL-LSP approach, to 110 ppm with the SKEL-MT mechanism. The measured value was 207 ppm. Ammonia contours for this setting are not displayed, since practically all NH_3 is oxidized near the reactor inlet along with the fuel. This was predicted by all the mechanisms. Figure 7.11 displays NO and NH_3 concentration comparisons for the selected mechanisms. It appears that for this setting, the mechanisms agree on the trend and a fast conversion of the NH_3 and only the quantitative prediction of NO differs. In both settings, the oxidation of ammonia occurs along with the main combustion process, as observed experimentally.

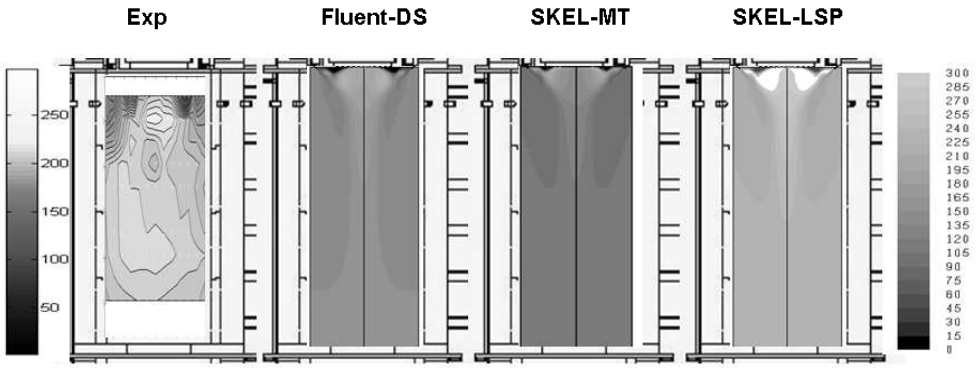

Figure 7.10: Contour plots of NO concentrations (ppm dry) for the setting with high secondary air flow (setting 1). From left: Experimental, Fluent-DS, SKEL-MT, SKEL-LSP.

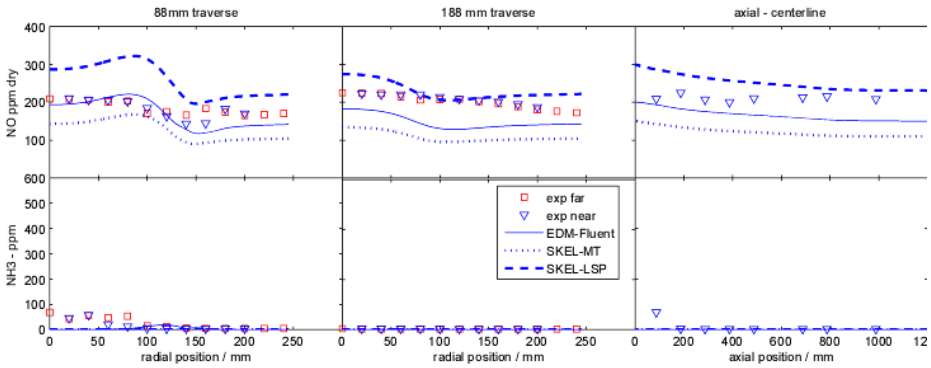

Figure 7.11: Comparison of measurement data and CFD predictions for NO and NH_3 at various positions in the setup. Setting 1 (max secondary air). Near and far side labels refer to the location of the extraction probe insertion.

Table 7.2 summarizes the exit NO concentrations measured and predicted by the different combinations of combustion and ammonia oxidation models. The values are reported in % of added fuel-N converted to NO. This measure is used to account for the difference in dilution with secondary air in the two settings analyzed. The table shows that the SKEL-LSP approach and the Fluent-DS approach obtain the best agreements with the measured conversion ratios. Except for JL-MT and JL-Brink, all mechanisms are able to qualitatively predict that NO emissions should increase when applying high secondary air (setting 1). The DS scheme overpredicted NO emissions, when integrated in the EDC turbulence interaction framework, but in the pure post-process approach offered by Fluent it produces usable results. The temperature in the reactor does not at any measurement position exceed 1600 K, so thermal NO is not expected to contribute to NO formation in this specific test-case. This was confirmed by enabling and disabling the thermal NO mechanism in Fluent and in the LSP mechanism, the thermal NO formed in the reactor was predicted to less than 5 ppm.

Table 7.2: Calculated NO emissions with different combinations of combustion models and ammonia oxidation schemes. Results are represented as % of added fuel-N converted to NO.

SET1	Fluent-DS	Fluent-LSP	MT	DS	Brink	LSP	Exp.
EDM	48.2						
JL	45.7		29.6	88.1	23.5		**66.6**
SKEL	44.7	40.2	35.4	93.9	36.3	74.3	
SET2	Fluent-DS	Fluent-LSP	MT	DS	Brink	LSP	Exp.
EDM	36.1						
JL	20.9		38.0	81.0	37.0		**40.9**
SKEL	38.0	32.9	31.0	72.1	21.9	60.6	

The results of Table 7.2 indicate that the combustion solution has a major

impact on the NO formation predicted by the global mechanisms. Perhaps more surprisingly, it also has a major impact whether the nitrogen chemistry is solved in conjunction with the combustion or using a post-processing approach. Comparing the two DS predictions, it is seen that the Fluent NO post-processing approach yields a lower conversion of ammonia to NO than the EDC approach. The same trend is observed for the LSP predictions. Figure 7.12 displays the difference between the two approaches for the LSP nitrogen mechanism in setting 2.

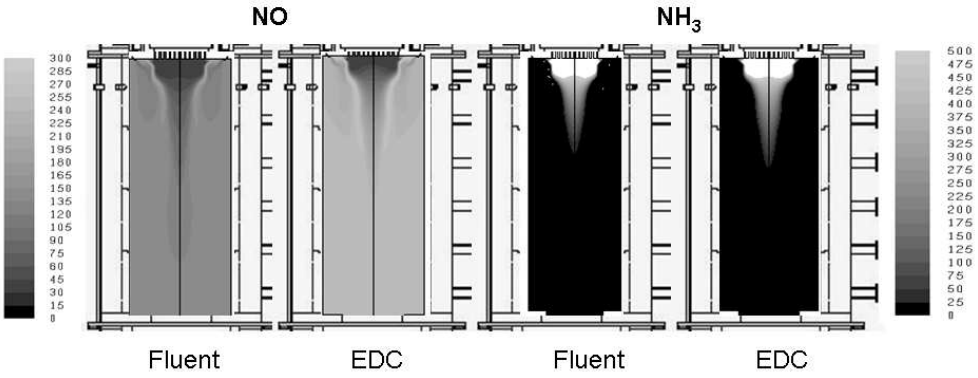

Figure 7.12: Contour plots of NO concentrations (ppm dry) and NH_3 concentrations (ppm) for setting 2 (low secondary air) flow, using the SKEL mechanism for combustion and the LSP scheme for NO formation. The calculations are conducted with SKEL/LSP run in conjunction (EDC) and with LSP run in a post-processing mode (Fluent).

The observed differences indicate that the decoupling of the fuel-NO formation from the combustion process may introduce errors. The fuel is competing with the volatile-N for the available O_2. Even though the nitrogen chemistry does not affect the main combustion process to a significant extent due to the low concentrations, the availability of excess O_2 for the volatile-N oxi-

dation is limited by consumption of O_2 by the main combustion process. In the post-processing approach, the level of O_2 may be reduced compared to the situation with simultaneous oxidation of fuel and volatile-N. Thereby the selectivity is shifted towards N_2 instead of NO. The difference will depend on the grid resolution, being smaller on a finer grid.

7.7 Conclusion

In a CFD analysis of a 50 kW combustion setup operating at two different settings, the global ammonia oxidation schemes by De Soete, Mitchell & Tarbell, and Brink et al., and the analytically reduced volatile-NO mechanism by Pedersen et al. [14] were appended to combustion solutions obtained by the two-step Eddy Dissipation Model (EDM), the four-step combustion mechanism by Jones and Lindstedt, and the skeletal mechanism by Yang and Pope. The combination of the skeletal combustion mechanism and the reduced nitrogen chemistry provided satisfactory agreement with experimental data in both settings analyzed. However, also the standard Fluent approach by post-processing with the DS mechanism provided a reasonable agreement with the experimental data. Most of the tested ammonia oxidation schemes were able to qualitatively predict the trends in NO for the different operating conditions. However, the predicted NO formation was sensitive to the main combustion solution on which the ammonia oxidation is based, where the agreement with experimental data did not always improve with more advanced chemical mechanisms. It also had a significant impact whether the nitrogen chemistry was solved in conjunction with the combustion or using a post-processing approach. In general the Fluent NO post-processing ap-

proach predicted a lower conversion of ammonia to NO than integrating the NO scheme in the EDC framework.

The trends observed in the CFD modeling were consistent with tests of the NH_3 oxidation schemes by ideal plug flow reactor modeling. None of the global ammonia schemes matched reference calculations with a detailed mechanism (DCKM) at all conditions, while the analytically reduced nitrogen mechanism provided a satisfactory prediction of NO. The DS mechanism consistently predicted NH_3 consumption to be slower than the fuel oxidation, contrary to the detailed reference calculations. In fuel-lean conditions, the DS scheme approach the similar output levels as the DCKM; however, under fuel-rich conditions the scheme fail to capture the ammonia conversion.

7.8 Acknowledgments

The present work was funded by the Technical University of Denmark, DONG Energy, Vattenfall, Babcock & Wilcox Vølund, B&W Energy, The Danish Technical Research Council, and the Public Service Obligation programme under contract PSO 4792. The authors would also like to acknowledge the helpful modeling assistance and discussions with Jesper Møller Pedersen, DONG Energy.

7.9 References

[1] Glarborg, P.; Jensen, A.D.; Johnsson, J.E. Prog. Energ. Combust. Sci. 2003, 29, 89-113.

[2] Tian, F.; Yu, J.; McKenzie, L.J.; Hayashi, J.; Li, C. Energy Fuels 2007, 21, 517-521.

[3] Lindstedt, R.P.; Lockwood, F.C.; Selim, M.A. Combust. Sci. Technol. 1995, 108, 231-254.

[4] Glarborg, P.; Alzueta, M.U.; Dam-Johansen, K.; Miller, J.A. Combust. Flame 1998, 115, 1-27.

[5] Skreiberg, Ø.; Kilpinen, P.; Glarborg, P. Combust. Flame 2004, 136, 501-536.

[6] Tian, Z.; Li, Y.; Zhang, L.; Glarborg, P.; Qi, F. Combust. Flame 2009, 156, 1413-1426.

[7] De Soete, G.G. Proc. Combust. Inst. 1975, 15, 1093-1102.

[8] Mitchell, J.W.; Tarbell, J.M. AIChe J. 1982, 28, 302-311.

[9] Brink, A.; Kilpinen, P.; Hupa, M. Energy Fuels 2001, 15, 1094-1099.

[10] Duo, W.; Dam-Johansen, K.; Østergaard, K. Can. J. Chem. Eng. 1993, 70, 1014-1020.

[11] Jensen, A.; Johnsson, J.E.; Andries, J.; Laughlin, K.; Read, G.; Mayer, M.; Baumann, H.; Bonn, B. Fuel 1995, 74, 1555-1569.

[12] Brouwer, J.; Heap, M.P.; Pershing, D.W.; Smith, P.J. Proc. Combust. Inst. 1996, 26, 2117-2124.

[13] Fluent 6.3 users guide, Fluent inc., Centerra Resource Park, 10 Cavendish Court, Lebanon, NH 03766 (2005)

[14] Pedersen, L.S.; Glarborg, P.; Dam-Johansen, K. Combust. Sci. Technol. 1998, 131, 193-196.

[15] Norström, T.; Kilpinen, P.; Brink, A.; Vakkilainen, E.; Hupa, M. Energy Fuels 2000, 14, 947-952.

[16] Visona, S.P.; Stanmore, B.R. Chem. Eng. Sci. 1998, 53, 2013-2027.

[17] Sheng, C.; Moghtaderi, B.; Gupta, R.; Wall, T.F. Fuel 2004, 83, 1543-1552.

[18] Klason, T.; Bai, X.S. Fuel 2007, 86, 1465-1474.

[19] Le Bris, T.; Cadavid, F.; Caillat, S.; Pietrzyk, S.; Blondin, J.; Baudoin, B. Fuel 2007, 86, 2213-2219.

[20] Ma, L.; Jones, J.M.; Pourkashanian, M.; Williams, A. Fuel 2007, 86, 1959-1965.

[21] Yang, Y.B.; Newman, R.; Sharifi, V.; Swithenbank, J.; Ariss, J. Fuel 2007, 86, 129-142.

[22] Saario, A.; Oksanen, A. Energy Fuels 2008, 22, 297-305.

[23] Diez, L.I.; Cortes, C.; Pallares, J. Fuel 2008, 87, 1259-1269.

[24] Glarborg, P.; Lilleheie, N.; Byggstøyl, S.; Magnussen, B., Kilpinen, P.; Hupa, M. Proc. Combust. Inst. 1992, 24, 889-898.

[25] Andersen, J.; Jensen, P.A.; Meyer, K.E.; Hvid, S.L.; Glarborg, P. Experimental and numerical investigation of gas phase freeboard combustion. Part I: Main combustion process", submitted for publication (2009)

[26] Mendiara, T.; Glarborg, P. Ammonia chemistry in oxy-fuel combustion of methane, Combust. Flame, 2009, 156, 1937-1949

[27] Hanson, R.K.; Salimian, S. Survey of Rate Constants in H/N/O Systems. In W.C. Gardiner, editor, Combustion Chemistry, page 361, 1984.

[28] Westbrook, C.K.; Dryer, F.L. Prog. Energy Comb. Sci. 1984, 10, 1-57.

[29] Jones, W.P.; Lindstedt, R.P. Combust. Flame 1988, 73, 233-249.

[30] Yang, B.; Pope, S.B. Combust. Flame 1998, 112, 16-32.

[31] Streibel, T.; Hafner, K.; Mühlberger, F.; Adam, T.; Warnecke, R.; Zimmerman, R. Anal. Bioanal. Chem. 2006, 384, 1096-1106.

[32] Åmand, L.-E.; Kassman, H.; Karlsson, M.; Leckner, B. J. Inst. Energy 1997, 70, 25-30.

[33] Kassman, H.; Åmand, L.-E.; Leckner, B. J. Inst. Energy 1997, 70, 95-101.

[34] Glarborg, P. Proc. Combust. Inst. 2007, 31, 77-98.

Chapter 8

Scaling issues

The experimental setup is not a direct downscaling of the freeboard of an actual grate fired boiler. This chapter does however make a simplified comparison of the fluid dynamic and turbulent length scales present in the experimental setup with that of a full scale biomass boiler, the Avedøre biomass combustion facility in Copenhagen (AVV). In table 8.1 comparable dimensions and flow properties for the pilot scale experimental setup and AVV are listed.

The Reynolds numbers $Re = \frac{Dv}{\nu}$ displayed in table 8.1 is found by using the characteristic jet and freeboard diameters and the physical properties (density and viscosity of air) at temperatures close to the expected mean temperatures in the furnace and air jet region. The dominating process responsible for oxidation of fuel and pollutant formation in most industrial combustion systems is the turbulent mixing of reactants (and heat). This mixing is dominated by the dissipation of large size eddies (eddies in the order of magnitude similar to the geometry dimensions) to smaller and smaller eddies, eventually down to the Kolmogoroff length scale, l_k where the inertial

	Exp. setup	Avedøre	unit
Freeboard diameter	0.49	6.5	m
Typical secondary air jet diameter	0.25	3.0	cm
Total flow in freeboard	1	2250	Nm^3/min
Secondary air through one nozzle	1.5	432	Nl/min
Avg. freeboard velocity (T=1300K)	0.33	4.4	m/s
Avg. seconday air jet velocity (T=600K)	10.8	22.8	m/s
Re freeboard (T=1300K)	900	150000	-
Re secondary air jet (T=600K)	500-1000	13000	-

Table 8.1: Comparison of dimensions and volume flows in the experimental setup compared to a full scale facility, when calculating the Reynolds numbers the dynamic viscosity of the gas is assumed to equal that of air, $\nu_{1300K} = 1.9 \cdot 10^{-4}$ and $\nu_{600K} = 5.3 \cdot 10^{-5}$ (physical properties from [1])

and viscous forces balance.

On its way to complete dissipation the turbulent eddy takes on other characteristic length scales starting at the integral length scale, l_0 (macroscale) where the eddy size is in the order of magnitude close to the geometry dimensions, L. Further dissipation leads to the Taylor microscale,l_λ which is a measure for the average eddy size, where most of the dissipation occurs. The integral, Taylor and Kolmogoroff length scales can be estimated roughly according to Ertesvaag [2] through estimating the dissipation rate and the

turbulent kinetic energy:

$$\epsilon \approx \frac{u'^3}{L} \tag{8.1}$$

$$k \approx \frac{3}{2} \cdot u'^2 \tag{8.2}$$

$$l_\lambda \approx \left(\frac{10\nu k}{\epsilon}\right)^{0.5} \tag{8.3}$$

$$l_k = \left(\frac{\nu^3}{\epsilon}\right)^{0.25} \tag{8.4}$$

In equations 8.1 to 8.4 ν is the kinematic viscosity, u' is the velocity fluctuations (assumed to be isotropic) and ϵ is the eddy dissipation.

Table 8.2 summarizes the rough estimations of the turbulent length scales in the flow based on equations 8.1 to 8.4. To make these estimations, a rough estimate of the velocity fluctuations needs to be made. In the experimental setup the typical maximal measured velocity fluctuation is approximately 0.9 m/s. For the Avedøre biomass unit no velocity measurements exists, so fluctuations of 10 m/s are assumed. This value is based on the full scale LDA measurements performed by Ereaut and Gover [3], where a maximum RMS value of 10 m/s was found at a position with maximum mean velocities of 25 m/s in a full scale burner. Table 8.2 shows, that even though the dimensions and velocities of the compared plants deviate significantly, the size of the turbulent length microscales are in the same order of magnitude, indicating a scaling agreement between the facilities.

8.1 Traditional scaling of combustion systems

Spalding [4] referred to scaling of combustion systems as *partial modeling* in 1962. The reason for the phrase partial was, that he had realized that

	Exp. setup	AVV	units
Velocity fluctuation u'	0.9	10	m/s
k	1.2	150	m^2/s^2
ϵ	1.5	154	m^2/s^3
Taylor Microscale l_λ	2	5	cm
Kolmogorof length scale l_k	0.6	0.5	mm

Table 8.2: Characteristic turbulent length scales and Reynolds numbers for the experimental setup and AVV based on data from table 8.1

complete combustion modeling scaling is impossible [4]. Spalding lists in his paper several scaling criteria, for chemical kinetics, radiation, diffusion, buoyancy, heat and mass transfer etc. All these quantities scales with each other by different dimensionless groups, furthermore geometrical and time scaling adds to the complexity of scaling combustion systems. The essence of Spalding's paper is that for relevant information of a "full-scale" combustion system it is not necessary (or possible) to model(scale) all parameters, but only those dominating the effects that is to be examined.

8.1.1 Scaling of burners

Traditionally two basic criteria are used to scale burners and flames; constant-velocity scaling or constant residence time scaling. The burner flame scale is normally defined by the load i.e. volume flow of fuel through the flame (see (8.5)) [5].

$$Q_0 \prec \rho_0 U_0 D_0^2 \tag{8.5}$$

By assuming constant fluid density, the constant velocity scaled flame scales

in the proportions displayed in equation (8.7)

$$U_0 = constant \tag{8.6}$$

$$\frac{Q_{0,baseline}}{Q_{0,scaled}} = \left(\frac{D_{0,baseline}}{D_{0,scaled}}\right)^2 \tag{8.7}$$

Similarly for the constant residence time scaling:

$$\tau_{macro} = \frac{D_0}{U_0} = constant \tag{8.8}$$

$$\frac{Q_{0,baseline}}{Q_{0,scaled}} = \left(\frac{D_{0,baseline}}{D_{0,scaled}}\right)^3 \tag{8.9}$$

This indicates that it is impossible to scale a flame and maintain both residence time and flame velocity. Smart [5] chooses to define a macro-mixing time scale (see equation (8.9)). Scaling by constant macro mixing time scale will account for the large scale mixing of fuel and oxidiser, however fuel and air do not react to products before they are mixed down to molecular level, at the Kolmogoroff turbulent mixing scale. The turbulent mixing at the micro time scale is defined by:

$$\tau_{micro} = \nu^{0.5}\left(\frac{l}{u'^3}\right)^{0.5} \tag{8.10}$$

$$\tau_{micro} = \nu^{0.5}\left(\frac{100D_0}{U_0}\right)^{0.5} \tag{8.11}$$

Where l is the characteristic turbulent mixing scale, ν_t is the turbulent diffusivity and u' is the turbulent velocity fluctuations. Equation (8.11) is a rewrite of (8.10), where the factor 100 accounts for the assumed length scale of the micro-mixing process l is $0.1D_0$ and the assumed characteristic turbulent velocity is 0.1 U_0. Smart [5] defines a global mixing-time, $\tau_{mix,flame}$ as

the sum of the micro and macro mixing times:

$$\tau_{mix,flame} = \tau_{macro} + \tau_{micro} \tag{8.12}$$

$$\tau_{mix,flame} = \frac{D_0}{U_0} + \nu_t^{0.5} \left(\frac{100 D_0}{U_0^3} \right)^{0.5} \tag{8.13}$$

Figure 8.1 states the theoretical relationship between the mixing constant and the scaling exponent, n. In the figure a constant turbulent diffusivity is assumed across all scaling ranges, this assumption is only valid if all flames are fully turbulent.

Figure 8.1 states that a constant velocity (down)scaled flame will mix the reactants too fast, and chemical reactions will dominate, whereas the opposite is true for the constant residence time mixing, which mixes too slow [5].

Smart [5] therefore argues that flame characteristics can not be downscaled using either constant residence time or constant velocity scaling.

The experimental setup is not directly comparable with a burner setup, but by comparing the dimensions in the setup, with the full scale facility, an estimation of the scaling exponent can be done. Table 8.3 shows calculations of the scaling exponent based on the dimensional relationships between the Avedøre biomass boiler and the experimental setup. The experimental setup was designed from a constant residence time principle, which is confirmed by the approximate scaling exponent of 3 for the freeboard specific velocity and dimensions. When instead comparing on single secondary air jet, the scaling exponent ranges from 2.04 to 2.3 (depending on whether it is compared to experimental setting 1 or 2), indicating that the jets have comparable inlet velocities with the large scale facility.

According to Figure 8.1 the constant residence time scaling indicates that mixing processes becomes more dominant. However arguably the constant

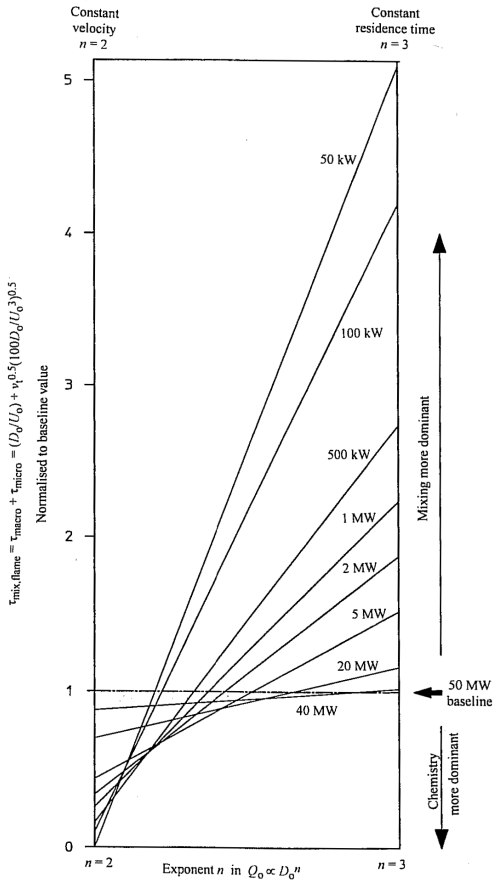

Figure 8.1: Relationship for the mixing time scale $\tau_{mix,flame}$ and the scaling exponent n.[5]

velocity scaling of the secondary inlet jets could indicate the opposite. Weber [6] argues that this discussion of scaling only makes sense, when comparing similar flow patterns. Although it is impossible to maintain all important dimensionless groups during flame-scaling it is usually argued, that at least the Reynolds number should be sufficiently high [4, 6]. This is not the case for the present experimental setup as Table 8.1 displays. Therefore the main difference between the present setup and larger scale facilities is arguably the

	Exp. setup	Avedøre	units
Freeboard			
D_0	0.49	6	m
U_0	0.34	4.3	m^2/s^2
n		**3.01**	cm
Sec. air jet			
D_0	0.0025	0.03	m
U_0	10.8-22.3	22.7	m^2/s^2
n		**2.04-2.3**	cm

Table 8.3: Scaling exponent estimations for the experimental setup in relation to a full scale boiler.

lower Reynolds numbers seriously challenging the validity of turbulence and turbulence-chemistry interaction models.

8.1.2 NO_X emissions scaling

Smart supports the argument that a constant velocity (down)scaled flame will mix the reactants too fast, and chemical reactions will dominate, by comparing NO_X emissions for a baseline (12MW) and two downscaled (2.5MW) pulverised coal flames. The result is that the constant velocity scaled flame increases NO_X emissions, while constant residence time decreases NO_X emissions [5].

Hsieh et al. [7] published an extensive study on scaling of NO_X emissions. They used the extensive experimental data from a study named SCALING 400, where both the burner and furnace part of a fuel staged swirl burner

system fired with natural gas was scaled from 30kW to 12MW using the constant velocity scaling principle. Differing NO_X emissions was found for identical scaled systems, indicating that thermal NO_X formation is not scalable directly using the constant velocity principle, which fails to reproduce aerodynamic similarity in the near burner region.

Santos and Costa also described the prediction thermal NO formation, but from unconfined vertical turbulent jet flames of propane and ethylene.[8] The NO_X emissions from such a flame is controlled by parameters such as flame volume, relative importance of various chemical NO formation routes, superequilibrium radical concentrations, temperature, flame strain and flame radiation.[8] In accordance with Hsieh et al. [7] Santos and Costa state that the flame volume is the leading parameter for NO_X formation, and that this flame volume scales with the Froude number for buoyancy controlled flames. Santos and Costa do however emphasize that the fuels propensity for soot formation can influence the scaling of NO_X formation significantly. [8] The NO_X formation route in these gas scaling studies are all primarily thermal NO, the scaling of conversion of fuel N to NO is presumably more difficult to scale, since the release of fuel N (from solid fuels) depends on particle size as well as char and tar residues may react with gas phase nitrogen. HCN and NH_3 is the gas species primarily released from solid fuels and the oxidation of these compounds depends largely on air excess ratio [6, 9].

Sadakata and Hirose [10] stated that flow pattern as well as micro and macro mixing scales needed to coincide in order to scale pollutant emissions. For high Reynolds numbers, Re was not expected to affect the flow field. Sadakata and Hirose [10] listed the most important scaling phenomena for

pollutant formation and concluded that micro mixing time and air-fuel ratio seems to be the most important parameters to have coinciding with large scale conditions when interested in fuel NO formation and CO emission.

8.2 Description of jet flows

The flow field in the experimental setup is presumably dominated by the high momentum injection of secondary air through 210 small (2.5mm in diameter) round jets positioned in a circle with a 45 degrees inclinement. In the original construction a round slit with a gap of 1mm was designed, corresponding to an axisymmetric planar jet, unfortunately it was not possible to construct and maintain the gab width constant during operation, so the circle of holes was instead implemented. As the secondary air jet enters the freeboard area, it will meet with the low velocity primary gas and a free shear layer flow will develop. The following chapters briefly describe the characteristics of jet flows.

8.2.1 Jets

Jets are normally divided into three regimes; laminar, transitional and turbulent. It is stated, that the transitional regime for a round free jet starts at Re$\approx$1000 and for Re$>$3000 the jet is fully turbulent [11]. Whereas planar jets show transitional behavior starting already at Re$\approx$30 [11].

The experimental setup is capable of reaching Reynolds numbers up to 1000, Reynolds numbers betweeen 500 and 1000 are used in the current testcases.

The flow regime in the current testcases are probably transitional - LDA measurements show considerable velocity fluctuation and visual inspection of the flame also reveals what seems to be turbulent eddies.
Even though a flow is not fully turbulent it may still exhibit transient behavior. For a transitional diffusion flame (see Figure 8.2) the current instabilities may occur:

- The Kelvin-Helmholtz (KH) instability results from velocity shears between two flows. These flows do not even have to have different densities. Any time there is a non-zero curvature, the flow of one fluid around another will lead to a slight centrifugal force which in turn leads to a change in pressure thereby amplifying the ripple.[12, 13]
- Reactions at the flame front causes thermal expansion, which leads to vortex formation. [12, 14]
- Buoyancy effects causes gradients resulting in vortices.[12, 13]
- pairing of vortices causes secondary vortices.[12, 13]

All these effects may play an important role in the experimental setup, thereby making it more complicated and comprehensive to satisfactorily model the combustion system. It is also difficult to asses the importance of the different effects, since the experimental setup does not exactly compare to a standard jet or flame type. The setup is some kind of hybrid between a round and planar-axisymmetric confined jet. Furthermore it is not directly comparable to a jet diffusion flame, since the jet flow is the cold air flow entering into a fuel flow with less momentum. Buoyancy effects do not compare directly to that of a diffusion flame either, because the fuel flow

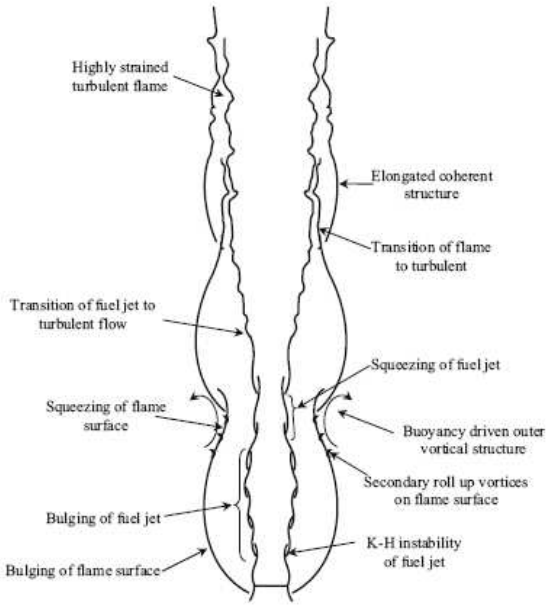

Figure 8.2: Schematic of typical transitional flame showing various instabilities. [13]

is pre-heated by the 1st stage reactions, but also because the setup is down-fired. This means that although hot gases are formed at the flame front, the buoyant force, which is expected to make the gases rise is not as pronounced as in a jet flame because of a lower temperature and thereby density gradient.

8.2.2 Modeling of jets and jet flames

Several studies have been performed on modeling low-Re jet[1], flows with several interacting jets or jet diffusion flames.

Yimer et al. [15] modeled the mixing of a strong air jet(Re = 30000) with a weak fuel jet (Re = 5000) using the standard $k - \epsilon$ turbulence model. They

[1]The term low-Re jet is here referred to as a jet flow with a jet Reynolds number in the transitional or lower turbulent regime

found that the modeling generally picked up the trends in the jet profiles well. However an arching of the fuel jet was not captured well by the model, and the authors state that this is due to the well known weakness of the $k-\epsilon$ model to model flows with strong streamline curvatures. [15]

Lai and Nasr [16] compared the performance of 3 turbulence models in predicting the free shear flow field from two parallel planar (non-reacting) jets (Re = 11000). The standard $k-\epsilon$, the RNG $k-\epsilon$ and the Reynolds Stress Models were compared, and the authors found that all of the models qualitatively predicted the flow field nicely. The standard $k-\epsilon$ and Reynolds Stress Models predicted the merging length of the jets better than the RNG model. However all of the models seriously underpredicted the turbulence intensities (with up to 50%).[16]

In a similar study Anderson and Spall [17] compared numerical modeling and experimental results when analyzing two identical planar parallel jets (Re = 6000). They conclude that both the standard $k-\epsilon$ and Reynolds Stress models obtained excellent agreement in the location of the merge and combination points of the jets and both models are capable of predicting the mean symmetry plane velocity profiles to good accuracy. [17]

Yaras and Grosvenor [18] evaluated four low-Re RANS models (a modified $k-\epsilon$ model, Wilcox and SST $k-\omega$ models and the Spalart Almares one equation model) ability to capture the vortex flow generated from an inclined jet (Re = 4910) in a cross flow. The authors found no significant difference in the performance of the four models, they also found that all four models were able to reproduce the rate of diffusion of the streamwise vortex with downstream distance and the trajectory of this vortex reasonably well, but

predictions of the overall velocity field, and the extent of cross-stream mass and momentum transfer were not as accurate.[18]

Based on the above mentioned references it seems that the standard RANS turbulence models have been applied to modeling of turbulent jets with some success, however the secondary air jets dominating the flow in the experimental setup are only in the transitional regime. Large Eddy Simulation is a more advanced and computationally prohibitive technique for turbulence modeling, which has proved to be able to capture detailed flow characteristics from turbulent jet flames, as for instance the modeling of the Sandia D flame conducted by Sheikhi et al. [19].

2D transitional jet flames has previously been modeled by Liu et al. [20] using 2D LES with dynamic Smagorinsky sub grid scaling and a reduced 4 step chemistry treatment. The results compared well with DNS results for a planar jet [20].

James and Jaberi [21] conducted both Direct Numerical Simulation (DNS) and 2D LES modeling of a transitional jet diffusion flame (Re = 1500), and found excellent agreement between the two methods. The authors contribute this fine agreement to the nature of a transitional planar jet, which close to the inlet, the flow is mainly characterized by large scale 2D structures, hence 3D effects are less important [21].

8.3 Summary on scaling issues

The experimental setup is not a direct geometrical down scale of a grate fired furnace, however a geometrical comparison with a full scale facility show that a constant residence time down scaling from a full scale freeboard conditions

can be assumed. However the secondary air jets also display velocities comparable to those in a large scale facility. A constant residence time scaling for burners and flames lead to increased importance of mixing compared to finite rate chemistry. It is not easily interpreted if this conclusion also is valid for the experimental setup compared to a full scale grate fired facility. The most critical issue regarding scale comparisons are that the Reynolds number for the experimental setup is in the transitional regime. Even though transitional jets display some sort of transient turbulent behavior it is doubtful whether RANS based models are valid. Hence at least 2D LES modeling could be interesting to apply for the current setup.

8.4 References

[1] S.E. Turns. *An Introduction to Combustion: Concepts and Applications, 2nd edition*. McGraw-Hill, 2000.

[2] I.S. Ertesvaag. *Turbulent strøyming og forbrenning*. Tapir, 2000.

[3] P.R. Ereaut and M.P. Gover. *J. Inst. Energy*, 64.

[4] D.P. Spalding. *Proc. Combust. Inst.*, 9:833–843, 1962.

[5] J.P. Smart. *J. Inst. Energy*, 71:152–155, 1998.

[6] R. Weber. *Proc. Combust. Inst.*, 26.

[7] T.-C A. Hsieh, W.J.A. Dahm, and J.F. Driscoll. *Combust. Flame*, 114:54–80, 1998.

[8] A. Santos and M. Costa. *Combust. Flame*, 142:160–169, 2005.

[9] P. Glarborg, A.D. Jensen, and J.E. Johnsson. *Prog. Energy. Combust. Sci.*, 29:89–113, 2003.

[10] M. Sadakata and Y. Hirosa. *Fuel*, 73:1338–1342, 1994.

[11] R.D. Blevins. *Applied Fluid Dynamics Handbook*. Van Nostrand Reinhold Company Inc., 1984.

[12] W.R. Katta and W.M. Roquemore. *Combust. Flame*, 92.

[13] P.S. Kohe and A.K. Agraval. *Flow Turbulence Combust.*, 79.

[14] C. Duwig, L. Urbina, L. Fucs, P. Griebel, and P. Siewert. *44th AIAA Aeros. Sci. meeting and exhibit*, 157.

[15] I. Yimer, H.A. Becker, and E.W. Grandmaison. *Combust. Flame*, 124.

[16] J.C.S Lai and A. Nasr. *Proc. Inst. Mech. Engrs.*, 212 G.

[17] E.A. Anderson and R.E. Spall. *J. Fluids Eng.*, 123.

[18] M.I. Yaras and A.D. Grosvenor. *Int. J. Numer. Meth. Fluids*, 42.

[19] M.R.H. Sheikhi, T.G. Drozda, P. Givi, F.A. Jaberi, and S.B. Pope. *Proc. Combust. Inst.*, 30.

[20] Y. Liy, K.S. Lau, C.K. Chan, Y.C. Guo, and W.Y. Lin. *Int. J. of Heat and Mass Transfer*, 46.

[21] S. James and F.A. Jaberi. *Combust. Flame*, 123.

Chapter 9

Conclusions

Experimental data from an approximately axisymmetric bench scale setup constructed to imitate the conditions second stage combustion in a grate fired boiler is produced. Two different experimental settings are analysed. The only difference between the settings is the secondary air addition, however the settings differ dramatically regarding flow pattern, location of combustion zone and quantity of NO formed.

The CFD modeling captures the main features of the combustion process and alternation in flow patterns between the two settings. The conventional CFD modeling approach by applying an Eddy Dissipation Model for the gas combustion, results in a reasonable prediction of flow, turbulence levels, temperature and major species concentrations.

The application of more advanced turbulence chemistry interaction models and finite rate chemistry does not result in improved agreement between measurements and results compared to traditional eddy dissipation modeling.

More advanced combustion mechanisms is tested by using the Eddy Dissipation Concept turbulence interaction model. A four step global mechanism and a skeletal mechanism provide reasonable agreement with the experimental data, although they also predict a slower CO conversion than observed and this at a considerably increased computational expense.

The experimental setup does not serve as a perfect validation case. The Reynolds numbers in the system put the flow regime in the transitional region, where turbulence modeling is difficult. Furthermore, the inclined jets show an affinity towards wall attachment, the entire modeling result is very sensitive to the prediction of these jets.

Ammonia is added to the natural gas to imitate fuel nitrogen. Various ammonia oxidation mechanisms are tested both in ideal isothermal plug flow reactor conditions and in CFD modeling.

The global mechanism by De Soete, which is the default mechanism in Fluent, is slow compared to other NH_3 oxidation mechanisms and also slower than the fuel oxidation. None of the global ammonia oxidation mechanisms tested matched the detailed mechanism NO predictions at all conditions. A reduced nitrogen mechanism proved to be a valid reduction of the nitrogen chemistry. The skeletal mechanism provided similar results as the detailed mechanism, and a combination of the skeletal combustion mechanism and the reduced nitrogen chemistry seemed to be a valid simplification of the detailed mechanism.

In the CFD implementation, the combination of the skeletal combustion mechanism and the reduced nitrogen chemistry provided good agreement with experimental data in both settings analyzed. But also the standard fluent approach by post-processing with the De Soete mechanism provided a reasonable agreement with the experimental data. The main combustion solution on which the ammonia oxidation is based seems to have a large impact on the quantitative NO formation.

Based on the results of the present work, the additional computational effort to implement the more detailed chemistry using the EDC approach may not yield improved computational accuracy. In the investigated system, the fuel conversion is dominated by the mixing process of fuel and air, and finite rate effects are negligible or within the uncertainties of the measurements. However, the Reynolds number in the system is quite low (Re $\approx$ 1000), and the assumptions of fully turbulent isotropic turbulence within the k-ϵ turbulence model is probably not as good as it would be in a fully turbulent large scale facility. This concern also goes for some of the constants within the turbulence chemistry interaction models.

Nomenclature

Greek letters

ρ	fluid density
$\overline{\overline{\tau}}$	viscous stress tensor
μ	molecular viscosity
ν	kinematic viscosity
ϕ	scalar variable
σ_s	a scattering coefficient
σ	the Stefan-Boltzmann constant
Φ	a phase function
Ω'	a solid angle
$\nu'_{i,r}$	stoichiometric coefficient of species i due in reaction r
τ^*	EDC time scale for chemical reactions

Roman letters

t	time
$\mathbf{v}$	direction velocity vector
S_m	source term
p	pressure
$\overline{\overline{I}}$	unit tensor
E	Energy
k	conductivity
k_{eff}	effective conductivity
k_t	turbulent thermal conductivity
$\mathbf{J}_j$	diffusion flux of species j
h_j	enthalpy of species j
Y_i	individual species mass fraction
R_i	production (or consumption) of species due to chemical reaction
S_i	source term for species production
$\mathbf{A}$	area vector
Γ_ϕ	diffusion coefficient of scalar
S_ϕ	source term for scalar
Re	Reynolds number
D	diameter
l_0	large eddy length scale
l_K	Kolmogorov length scale
x	direction variable
v	velocity variable
$\vec{s}'$	scattering direction vector
s	path length
a	medium absorption coefficient
n	refractive index
I	radiation intensity
k	chemical reaction rate constant
A_r	pre-exponential factor
β_r	dimensionless temperature exponent
E_r	the activation energy for the reaction
R	universal gas constant
K_r	equilibrium constant
$R_{i,r}$	rate of production of species i due to reaction r
M_w	molar weight
A	empirical constant
B	empirical constant
P	any product species
R	any reactant species
C_γ	volume fraction constant
C_τ	EDC model constant (=0,4082)
t_K	Kolmogorov time scale
f	mixture fraction
Z	elemental mass fraction
Sc_t	turbulent Schmidt number

Appendix A

Oxy fuel paper

This chapter contains the paper titled Global Combustion Mechanisms for Use in CFD Modeling Under Oxy-Fuel Conditions. The paper was made during this PhD, when supervising a project related to this PhD focusing on CFD modeling of gas phase oxy-fuel combustion.

The paper is published in energy and fuels: J.Andersen, C.L. Rasmussen, T. Giselsson and P. Glarborg, Energy Fuels 23:1379-1389 (2009)

Global Combustion Mechanisms for Use in CFD Modeling under Oxy-Fuel Conditions

Jimmy Andersen, Christian Lund Rasmussen, Trine Giselsson, and Peter Glarborg*

Department of Chemical and Biochemical Engineering Technical University of Denmark, DK-2800 Kgs. Lyngby, Denmark

Received May 16, 2008. Revised Manuscript Received December 16, 2008

Two global multistep schemes, the two-step mechanism of Westbrook and Dryer (WD) and the four-step mechanism of Jones and Lindstedt (JL), have been refined for oxy-fuel conditions. Reference calculations were conducted with a detailed chemical kinetic mechanism, validated for oxy-fuel combustion conditions. In the modification approach, the initiating reactions involving hydrocarbon and oxygen were retained, while modifying the $H_2-CO-CO_2$ reactions in order to improve prediction of major species concentrations. The main attention has been to capture the trend and level of CO predicted by the detailed mechanism as well as the correct equilibrium concentration. A CFD analysis of a propane oxy-fuel flame has been performed using both the original and modified mechanisms. Compared to the original schemes, the modified WD mechanism improved the prediction of the temperature field and of CO in the post flame zone, while the modified JL mechanism provided a slightly better prediction of CO in the flame zone.

Introduction

Oxy-fuel combustion is a promising technique for separating gaseous CO_2 with the intention of storing it, for instance in geological reservoirs. The separation of CO_2 is facilitated by removing the atmospheric nitrogen from air before combustion. Recirculated combustion products are used for diluting a pure O_2 stream. Due to the higher heat capacity and radiative properties of CO_2 compared to N_2, an increased oxygen concentration is required to obtain the same thermal conditions as combustion in air. For natural gas, a mixture of 28% O_2 and 72% CO_2 will result in a temperature field similar to combustion in air.[1] Oxy-fuel combustion will eventually result in a flue gas consisting mainly of CO_2 and steam. The flue gas can then undergo a condensation process to remove the H_2O, before a part of this flue gas consisting almost entirely of CO_2 is recirculated, while the remaining part is ready for compression and storage.[2]

Computational fluid dynamics (CFD) is becoming an important industrial tool for trouble-shooting and optimization. However, CFD modeling of industrial combustion applications is a computationally demanding task. For this reason, it is often necessary to apply simplified reaction mechanisms to reduce the computing effort. Chemistry is often represented by a mixed-is-burned assumption or an assumption of chemical equilibrium. Breussin et al.[3] performed a CFD analysis of a pure natural gas/oxygen flame, and found good predictions for the fluid dynamics, temperature and main chemical species concentration fields (O_2, CO_2) using both an Eddy Dissipation/mixed-is-burned approach and an EDC/chemical equilibrium approach. The mixed-is-burned model did, however, fail in predicting CO properly. In all the flames predicted, the equilibrium model showed to be superior to the mixed-is-burned model. The temperature and species concentrations predictions were better, since the effect of molecular dissociation has been accounted for. An alternative to these approaches is to employ finite-rate chemistry, using a scheme consisting of one or several global reactions. A number of simplified methane oxidation mechanisms has been proposed in literature.[4−9] Brink et al.[10] tested this approach under perfectly stirred reactor conditions. An equilibrium approach was compared with a three-step irreversible mechanism,[10] the four-step mechanism suggested by Jones and Lindstedt[6] and a detailed mechanism suggested by Glarborg et al.[11] Their conclusions were that thermodynamic equilibrium provides a poor description under conditions with a strong coupling between turbulent mixing and chemical reactions. The global mechanisms resembled the detailed model well at fuel-lean conditions. At fuel-rich conditions, the accuracy of the three-step irreversible model was less satisfactory, whereas the four-step mechanism performed better and correctly approached the equilibrium composition at long residence times. The four-step mechanism was reported to be a good compromise between accuracy and computational effort.[10]

Examples of CFD modeling using the global mechanisms can be found in the literature.[10,12−14] Also, in industrial CFD modeling, the global mechanisms are used frequently, presum-

* To whom correspondence should be addressed. Tel: +45 4525 2840. Fax: +45 4588 2258. E-mail: pgl@kt.dtu.dk.

(1) Andersson, K.; Johnsson, F. *Fuel* **2007**, *86*, 656–688.
(2) Wall, T. F. *Proc. Combust. Inst.* **2007**, *31*, 31–47.
(3) Breussin, F.; Lallemant, N.; Weber, R. *Combust. Sci. Technol.* **2000**, *160*, 369–397.
(4) Dryer, F. L.; Glassman, I. *Proc. Combust. Inst.* **1972**, *14*, 987–1003.
(5) Westbrook, C. K.; Dryer, F. L. *Combust. Sci. Technol.* **1981**, *27*, 31–44.
(6) Jones, W. P.; Lindstedt, R. P. *Combust. Flame* **1988**, *73*, 233–249.
(7) Dupont, V.; Pourkashanian, M.; Williams, A.; J. *Inst. Energy* **1993**, *66*, 20–28.
(8) Nicol, D. G.; Malte, P. C.; Hamer, A. J.; Roby, R. J.; Steele, R. C. *J. Eng. Gas Turbines Power* **1999**, *121*, 272–280.
(9) Meredith, K. V.; Black, D. L. *44th AIAA Aerospace Sciences Meeting* **2006**, *19*, 14161–14167.
(10) Brink, A.; Kilpinen, P.; Hupa, M.; Kjaldman, L. *Combust. Sci. Technol.* **1999**, *141*, 59–81.
(11) Glarborg, P.; Alzueta, M. U.; Dam-Johansen, K.; Miller, J. A. *Combust. Flame* **1998**, *115*, 1–27.
(12) Brink, A.; Mueller, C.; Kilpinen, P.; Hupa, M. *Combust. Flame* **2000**, *123*, 275–279.

Table 1. Westbrook and Dryer Global Multi Step Methane Combustion Mechanism with Kinetic Data (units in cm, s, cal, and mol)

mechanism	reactions	A	β	E_a	reaction orders	ref
WD1	$CH_4 + 1.5\ O_2 \rightarrow CO + 2\ H_2O$	1.59×10^{15}	0	47.8×10^3	$[CH_4]^{0.7}[O_2]^{0.8}$	4
WD2	$CO + 0.5\ O_2 \rightarrow CO_2$	3.98×10^{14}	0	40.7×10^3	$[CO][O_2]^{0.25}[H_2O]^{0.5}$	4
WD2r	$CO_2 \rightarrow CO + 0.5\ O_2$	5.0×10^8	0	40.7×10^3	$[CO_2]$	5

ably because the models are simple, cheap, and readily available. Furthermore, computationally simple mechanisms do provide adequate results if only the main species concentrations and the temperature picture is of interest. The simplified schemes cannot be expected, however, to work as well under oxy-fuel combustion conditions, as they do for conventional combustion. The exchange of the largely inert N_2 with a chemically reactive compound, CO_2; at least at high temperatures, has been shown to change the importance of some of the elementary reactions governing the combustion,[15] thereby requiring a modification of the global multistep reaction mechanisms to make them valid under oxy-fuel conditions.

The objective of the present work is to modify two simple multistep mechanisms, used frequently for describing conventional combustion, to handle the increased CO_2 concentration under oxy-fuel conditions. The two-step hydrocarbon oxidation mechanism by Westbrook and Dryer (WD)[5] is selected, since this scheme is directly available as default in the commercial CFD code Fluent.[16] The second scheme selected is the four-step mechanism of Jones and Lindstedt (JL).[6] The JL scheme is more complex but also has a higher accuracy and similar to the WD scheme, it is used regularly in CFD modeling of industrial applications.

The selected simplified mechanisms are compared with reference calculations, conducted with the detailed combustion mechanism proposed by Glarborg and Bentzen.[15] Their kinetic model provides good agreement with oxy-fuel combustion experiments. The work presented herein bears some resemblance to the work of Brink et al.[10] They also tested the Jones and Lindstedt four-step mechanism with reference calculations with a detailed mechanism, but only for conventional combustion conditions.

Modeling Approach. The Eddy Dissipation Concept (EDC) is a popular turbulence chemistry interaction model for CFD analysis of combustion applications. The Eddy Dissipation Concept is an extension of the Eddy Dissipation model[17] based on the work by Gran and Magnussen.[18,19] In the EDC model, chemical reactions are assumed to occur in the fine structures of the computational cells. These small scale structures can be pictured as a part of the cell, where Kolmogorov-sized eddies containing combustion species are situated so close together that mixing on the molecular level is taking place. The EDC model evaluates the volume of each cell, where mixing on a molecular scale is occurring, and treats this part of the cell as a Perfectly Stirred Reactor (PSR/CSTR). The cell volume fraction and reactor residence time is depending on turbulence parameters for the specific computational cell.[18,19]

Since the turbulence/chemistry interaction description in CFD may involve ideal reactor modeling, a comparison of the performance of different global multistep reaction mechanisms should be conducted under similar conditions. True to the concept of Gran and Magnussen,[18,19] Brink et al.[10] tested the simplified models under perfectly stirred reactor conditions. However, it is questionable whether commercial CFD codes actually employ a PSR solver for the chemistry, since the resulting algebraic equations may yield convergence problems. More likely, codes like Fluent employ a numerical solver that performs an integration in time. Consequently, in the present work, isothermal plug flow reactor (PFR) modeling, rather than PSR calculations, is used to compare the global and detailed mechanisms. Detailed model predictions have been obtained from plug flow simulations using the Senkin code from the Chemkin−II library.[20] The global multistep model PFR calculations have been performed in Matlab. Even though the Chemkin 4.0 package[21] can handle the noninteger reaction orders that are often applied in global mechanisms, the Matlab code was preferred because it facilitated comparison of several parameters for both the detailed and global models. It should be noted, however, that convergence can be problematic when using non-integer reaction coefficients and because of this, the stiff numerical solver ode15s was preferred over ordinary ODE solvers.

Detailed Chemical Kinetic Model (DCKM). In this work, the global mechanisms are compared to the detailed chemical kinetic mechanism (DCKM) presented by Glarborg and Bentzen.[15] To the authors' knowledge, this mechanism is the only one that has been validated against oxy-fuel experiments. The mechanism satisfactorily predicts CO, CO_2 and O_2 concentrations from oxidation of CH_4 by an O_2/CO_2 mixture in a flow reactor with residence times of approximately 1 s.[15]

The Westbrook and Dryer Two-Step Mechanism (WD). The WD model consists of two reactions, where the last step, oxidation of CO to CO_2, is reversible. The mechanism is listed in the form of three irreversible steps,

$$CH_4 + 1.5O_2 \rightarrow CO + 2H_2O \quad \text{(WD1)}$$

$$CO + 0.5O_2 \rightarrow CO_2 \quad \text{(WD2)}$$

$$CO_2 \rightarrow CO + 0.5O_2 \quad \text{(WD3)}$$

Table 1 displays the reaction rate data for the WD mechanism. The rate constants for (WD1) and (WD2) originate from Dryer and Glassman[4] who studied high temperature oxidation reactions of carbon monoxide and methane under fuel lean conditions ($\lambda > 2$) in a turbulent flow reactor. Later, Westbrook and Dryer[5] included the reverse reaction step for CO_2 decomposition (WD3) in order to reproduce the proper heat of reaction and pressure dependence of the $[CO]/[CO_2]$ equilibrium.

The Jones and Lindstedt Four-Step Mechanism (JL). Jones and Lindstedt[6] developed four-step global mechanisms for several hydrocarbon fuels. For methane, it involves the following steps:

$$CH_4 + 0.5O_2 \rightarrow CO + 2H_2 \quad \text{(JL1)}$$

$$CH_4 + H_2O \rightarrow CO + 3H_2 \quad \text{(JL2)}$$

$$H_2 + 0.5O_2 \rightleftarrows H_2O \quad \text{(JL3)}$$

$$CO + H_2O \rightleftarrows CO_2 + H_2 \quad \text{(JL4)}$$

The mechanism consists of two irreversible reactions, (JL1) and (JL2), describing the initial oxidation steps of a hydrocarbon. The two reversible reactions, (JL3) and (JL4), control the rate of reaction for CO and H_2. The rate coefficients for methane combustion are displayed in Table 2. Jones and Lindstedt validated the model against data for premixed methane and propane flames along with diffusion flame data for a methane-air flame. The mechanism was reported to perform well for both fuel-lean and moderately fuel-rich stoichiometries.[6] Two sets of rate parameters for reaction (JL3) were presented. Set (JL3a) was the preferred expression, but since it involved negative

Table 2. Jones Lindstedt Global Multi-Step Methane Combustion Mechanism with the Kinetic Rate Data (units in cm, s, cal, and mol)

no.	reactions	A	β	E_a	reaction orders	ref
JL1	$CH_4 + 0.5\ O_2 \rightarrow CO + 2\ H_2$	7.82×10^{13}	0	30.0×10^3	$[CH_4]^{0.5}[O_2]^{1.25}$	6
JL2	$CH_4 + H_2O \rightarrow CO + 3\ H_2$	0.30×10^{12}	0	30.0×10^3	$[CH_4][H_2O]$	6
*JL3*a	$H_2 + 0.5\ O_2 \rightleftharpoons H_2O$	4.45×10^{18}	−1	40.0×10^3	$[H_2]^{0.5}[O_2]^{2.25}[H_2O]^{-1}$	6
*JL3*b	$H_2 + 0.5\ O_2 \rightleftharpoons H_2O$	1.21×10^{18}	−1	40.0×10^3	$[H_2]^{0.25}[O_2]^{1.5}$	6
JL4	$CO + H_2O \rightleftharpoons CO_2 + H_2$	2.75×10^{12}	0	20.0×10^3	$[CO][H_2O]$	6

Table 3. Chemkin-Code for the JL Mechanism (3b H_2−O_2 Reaction) (units: cm, s, cal, mol, and K)

```
ELEMENTS C O H N END
SPECIES CH4 O2 H2O N2 CO CO2 H2 END
REACTIONS
CH4 + 0.5 O2 = > CO+ 2H2          7.82 × 10^13   0   30.0 × 10^3   !Jones Lindstedt 88
FORD /CH4 0.5/
FORD /O2 1.25/
CH4 + H2O = > CO + 3H2            0.30 × 10^12   0   30.0 × 10^3   !Jones Lindstedt 88
H2 + 0.5 O2 = > H2O               1.209 × 10^18  −1  40.0 × 10^3   !Jones Lindstedt 88
FORD /H2 0.25/
FORD /O2 1.5/
H2O + 0 O2 +0 H2 = > H2 + 0.5 O2  7.06 × 10^17   −0.877  97.9 × 10^3  !Calculated
FORD /H2 −0.75/
FORD /O2 1/
FORD /H2O 1/
CO + H2O = CO2+H2                 0.275 × 10^13  0   20.0 × 10^3   !Jones Lindstedt 88
END
```

reaction orders that might cause numerical problems, the set for (JL3b) was proposed as an alternative.[6]

If (JL3) had been an elementary reaction, the reverse rate constant could be determined from expression 1,

$$\frac{\dot{R}_{JL3,f}}{\dot{R}_{JL3,r}} = K_{JL3} = \frac{k_{JL3,f}[H_2][O_2]^{0.5}}{k_{JL3,r}[H_2O]} \tag{1}$$

Here, K_{JL3} is the equilibrium constant, k_{JL3} is the rate constant, and the f and r subscribts refer to the forward and reverse reactions, respectively. However, (JL3) is a global reaction and the forward reaction orders do not follow the stoichiometry. For this reason, the reverse reaction order for reaction (JL3a) or (JL3b) cannot be derived according to eq 1. In order for an equilibrium approach to be maintained for a global reaction, the expression 1 must still hold at equilibrium, here exemplified with reaction (JL3b):

$$\frac{\dot{R}_{JL3,f}}{\dot{R}_{JL3,r}} = \frac{\dot{R}^*_{JL3b,f}}{\dot{R}^*_{JL3b,r}} = \frac{k_{JL3,f}[H_2][O_2]^{0.5}}{k_{JL3,r}[H_2O]} = \frac{k^*_{JL3b,f}[H_2]^{0.25}[O_2]^{1.5}}{k^*_{JL3b,r}[H_2O]} \tag{2}$$

The superscript * refers to the global rate expressions. Since the forward rate constant for the global and the stoichiometric expression, respectively, must be identical ($k_{JL3,f} = k^*_{JL3b,f}$), the concentration dependence of the reverse reactions can be found as follows:

$$k^*_{JL3b,r} = k_{JL3,r}[H_2]^{-0.75}[O_2] \rightarrow \dot{R}^*_{JL3b,r} = k_{JL3,r}[H_2]^{-0.75}[O_2][H_2O] \tag{3}$$

In the present work, the derivation of the backward rates is done by evaluating the forward rates divided by the equilibrium constant at a series of temperatures (from 500 to 2500 K with 100 K increments) and then fitting an Arrhenius expression to the results, to obtain an individual expression for the reverse reaction. For reaction (JL3a) we obtain the expression,

$$k^*_{JL3a,r}(T) = 2.6 \times 10^{18} \cdot T^{-0.877} \cdot \exp\left(-\frac{49260}{T}\right) \tag{4}$$

and for reaction (JL3b),

$$k^*_{JL3b,r}(T) = 7.1 \times 10^{17} \cdot T^{-0.877} \cdot \exp\left(-\frac{49260}{T}\right) \tag{5}$$

These expressions make it possible to implement the forward and reverse reactions as irreversible steps, facilitating the use in commercial CFD software such as Fluent.[16]

In the following, only reaction 3b of the JL mechanism is used. Attempts to use 3a resulted in problems with convergence which may limit its use in CFD. Another concern related to 3a is that the reverse rate for (JL3a) is independent of the H_2O concentration. This makes sense when the purpose of the reaction is to dampen the forward reaction, but under conditions with large H_2O concentrations or even H_2O in the oxidizer stream a zero reaction order may be inappropriate.

A way to implement the JL mechanism in Fluent[16] is to import it as a Chemkin input file. In the newer versions of Chemkin, the FORD keyword is used to overwrite the forward reaction order, allowing global expressions to be implemented. Table 3 shows an example of a Chemkin input file, with reaction (3b) implemented. Note that in the reverse H_2−O_2 reaction, H_2 and O_2 have been added as reactants with 0 as stoichiometry coefficients. This is required to allow the program to overwrite the forward reaction orders.

Results and Discussion

In this work, we evaluate the performance of the WD and JL schemes under conditions of conventional combustion and oxy-fuel combustion, respectively, assuming plug-flow. Then the two schemes are revised for use under oxy-fuel conditions and tested again against reference calculations with the detailed mechanism. Finally, the original and modified schemes are implemented and compared for CFD calculations of a turbulent diffusion propane/O_2/CO_2 flame under conditions similar to those reported recently by Andersson and Johnsson.[1]

Performance of the WD and JL Mechanisms. Both the JL and the WD global mechanisms have been used extensively in CFD models for conventional combustion in air. Before we investigate how the schemes function under oxy-fuel conditions, we test them under normal combustion conditions by comparing with reference calculations with the detailed reaction mechanism. Since the mechanisms were optimized for fuel-lean conditions, we evaluate them at conditions with excess air.

Figure 1 compares CO, O_2 and CO_2 concentrations in an isothermal plug flow reactor at 1600 K and an excess air ratio

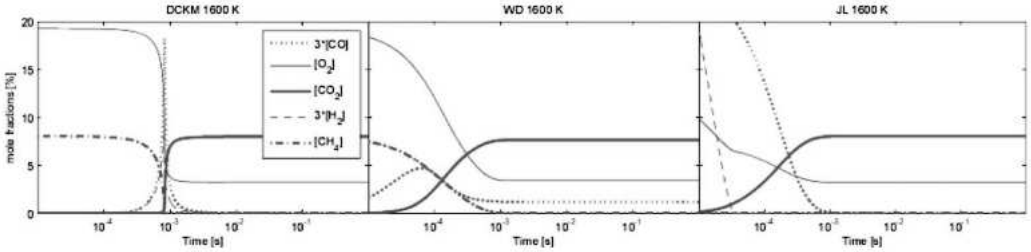

Figure 1. Major species concentrations in plug flow calculations. Comparison between the DCKM, the WD and the JL mechanisms at $\lambda = 1.2$ and 1600 K under "air" firing conditions (21% O_2 and 79% N_2).

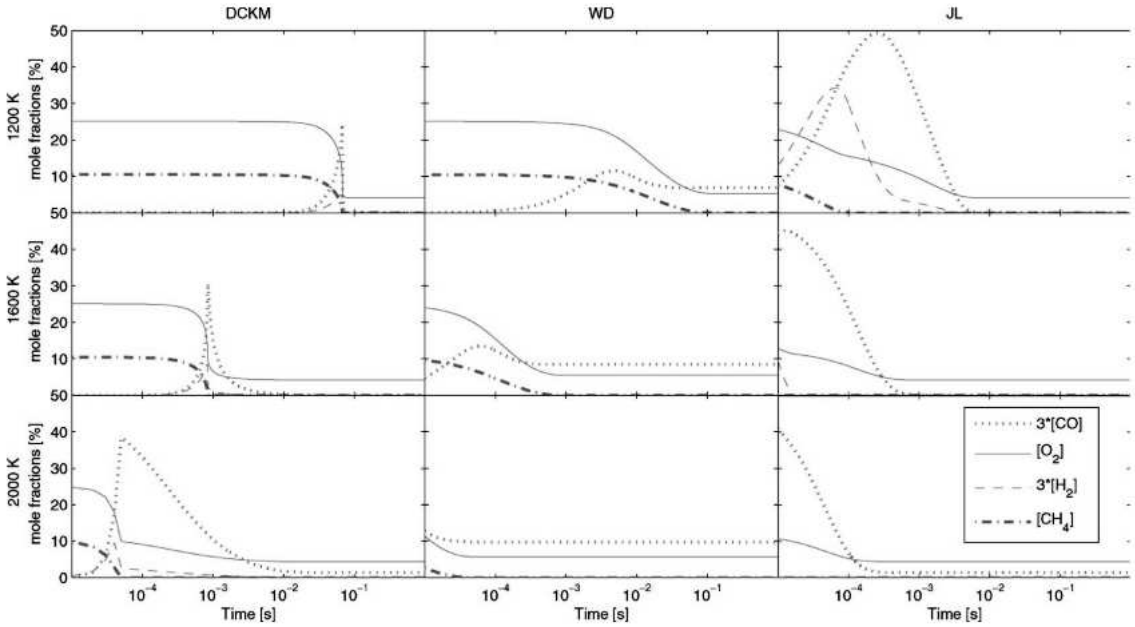

Figure 2. Major species concentrations in plug flow calculations. Comparison between the DCKM, the WD, and the JL mechanisms at $\lambda = 1.2$ and 1200 K (top), 1600 K (middle), and 2000 K (bottom) under "oxy"-firing conditions (28% O_2 and 72% CO_2).

of $\lambda = 1.2$. These results, along with other simulations, show that both the WD and JL mechanisms adequately predict O_2 and CO_2 levels at fuel lean conditions. Thereby, they would also yield a satisfactory prediction of the heat release for nonisothermal conditions at these stoichiometries. Only the JL mechanism predicts CO correctly at longer times under fuel lean conditions. The WD mechanism tends to overpredict the CO exit concentration and may not be sufficiently accurate for CO emission modeling.

As expected, the results show differences in the predicted ignition time between the three models. Only the detailed model can describe the slow build-up of the radical pool that eventually lead to ignition in a plug-flow calculation. The global schemes cannot account for an ignition delay. The WD mechanism was developed to describe the postignition fuel-consumption rate in PFR experiments, whereas the JL mechanism was optimized for flame conditions, where a radical pool is available through diffusional processes. It is difficult to assess how inaccuracies in the description of ignition affect a CFD calculation. In the EDC approach, PSR/PFR reactor residence times may be in the range of 10^{-4} to 10^{-3} s, i.e., time scales where there are considerable differences between modeling predictions. However, all three models predict the time scale for complete conversion of CH_4 to CO_2 to be of the order of 10^{-3} s, which is satisfactory.

The performances of the WD and JL mechanisms under fuel-lean oxy-firing conditions are displayed in Figures 2 and 3. At low temperatures (<1300 K) consumption of CO_2 is practically negligible,[15] and CO_2 is expected to have little chemical effect under these conditions. At higher temperatures, such as in the figures, atomic hydrogen may start to convert CO_2 to CO, resulting in a change in both the CO/CO_2 ratio and the composition of the O/H radical pool compared to conventional combustion. In general, the level of agreement between the global mechanisms and the reference calculations is similar to that observed under conventional combustion conditions. As expected, the WD mechanism cannot predict the CO exit concentration accurately; differences are seen at all temperatures. With the exception of the ignition timing, predictions of the JL mechanism generally compare well with those of the detailed mechanism. The ability of the JL scheme to compensate for the water−gas shift reaction (JL4) allows it to capture most changes caused by the elevated CO_2 concentration. Consequently, it predicts correct levels for all major species at longer reaction times, even under fuel-rich conditions. However, the CO peak levels are overpredicted in most cases.

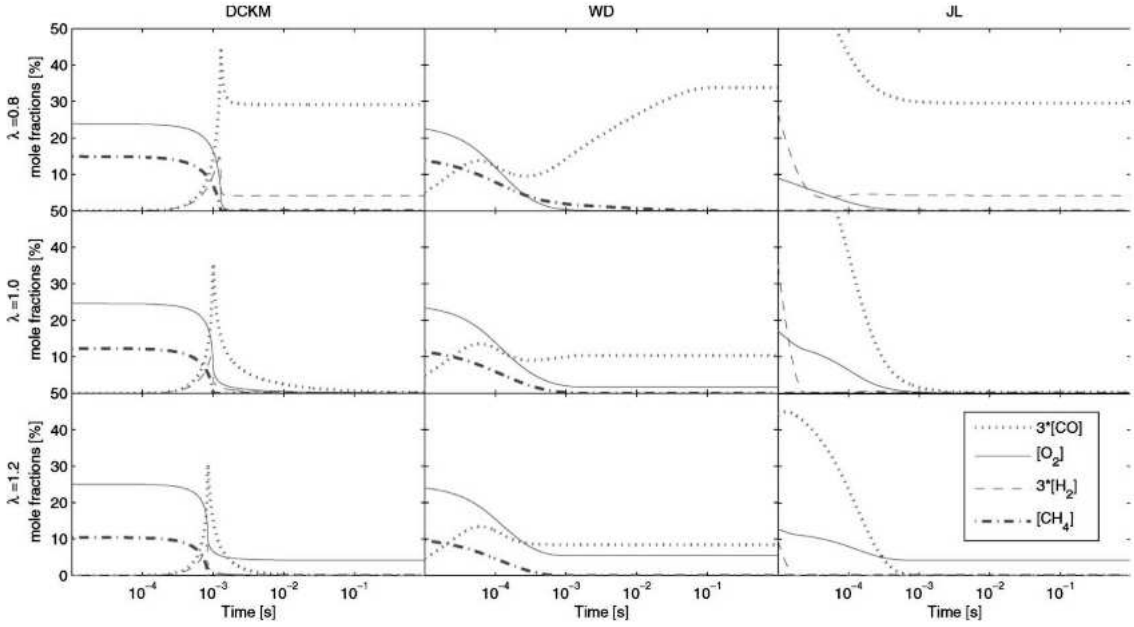

Figure 3. Major species concentrations in plug flow calculations. Comparison between the DCKM, the WD and the JL mechanisms at 1600 K and $\lambda = 0.8$ (top), $\lambda = 1.0$ (middle), and $\lambda = 1.2$ (bottom) under "oxy"-firing conditions (28% O_2 and 72% CO_2).

Table 4. Modified Multi Step Methane Combustion Mechanisms with Kinetic Rate Data - units in cm, s, cal, mol

reaction number	reactions	A	β	E_a	reaction orders
WD1	$CH_4 + 1.5\ O_2 \rightarrow CO + 2\ H_2O$	1.59×10^{13}	0	47.8×10^3	$[CH_4]^{0.7}[O_2]^{0.8}$
WD2(modified)	$CO + 0.5\ O_2 \rightarrow CO_2$	3.98×10^8	0	10.0×10^3	$[CO][O_2]^{0.25}[H_2O]^{0.5}$
WD3(modified)	$CO_2 \rightarrow CO + 0.5\ O_2$	6.16×10^{13}	−0.97	78.4×10^3	$[CO_2][H_2O]^{0.5}[O_2]^{-0.25}$
JL1	$CH_4 + 0.5\ O_2 \rightarrow CO + 2\ H_2$	7.82×10^{13}	0	30.0×10^3	$[CH_4]^{0.5}[O_2]^{1.25}$
JL2	$CH_4 + H_2O \rightarrow CO + 3\ H_2$	3.00×10^{11}	0	30.0×10^3	$[CH_4][H_2O]$
JL3(modified)	$H_2 + 0.5\ O_2 \rightarrow H_2O$	5.0×10^{20}	−1	30.0×10^3	$[H_2]^{0.25}[O_2]^{1.5}$
JL3 reverse	$H_2O \rightarrow H_2 + 0.5\ O_2$	2.93×10^{20}	−0.877	97.9×10^3	$[H_2]^{-0.75}[O_2][H_2O]$
JL4	$CO + H_2O \rightleftharpoons CO_2 + H_2$	2.75×10^{12}	0	20.0×10^3	$[CO][H_2O]$

Refined Schemes for Oxy-Fuel Combustion. It is apparent that the WD mechanism needs improvement to become applicable for oxy-fuel conditions due to the poor CO prediction. The JL mechanism works satisfactorily under oxy-fuel conditions, even though the prediction of the peak CO levels could be improved. In the present work, both global models are modified to improve the prediction of the steady state concentrations and the CO trends compared to the reference calculations.

The global mechanisms, refined for oxy-fuel conditions, are summarized in Table 4. The following criteria were employed in the modification procedure:

- In time, the concentrations should approach correctly the chemical equilibrium values.
- The peak CO concentrations should approximate the values predicted by the detailed model.

The modification window involved temperatures of 1200−2000 K and stoichiometries in the range $0.8 < \lambda < 1.5$.

In the WD scheme, the major issue was the rate coefficients for reaction (WD3), which did not secure an approach to equilibrium values for CO and CO_2. These were consequently modified by applying the global mechanism equilibrium approach for the $CO-CO_2$ reaction, following the procedure discussed above (see eqs 2−5). This change caused the WD scheme to predict the approach to equilibrium correctly, but resulted in an underprediction of CO at higher temperatures. To improve the CO prediction, it was necessary also to modify (WD2). Consequently, both the A-factor and the activation energy for (WD2) was lowered to match better the detailed model predictions.

When comparing the CO levels predicted by the JL mechanism with the detailed mechanism, it was observed that besides the difference in ignition timing, the peak CO levels deviated, most pronounced under oxy-fuel conditions (Figures 2 and 3). The predicted CO oxidation rate in the JL scheme is governed by the reaction with water vapor (JL4). Examination of the mechanism showed that it was the availability of H_2O (formed in reaction JL3), as well as the rate constant for (JL4), that limited the CO oxidation rate. Attempts to modify the JL4 rate constant proved unsuccesful; a decrease in k_{JL4} resulted in undesired changes at some conditions (prolonged burnout period), whereas an increase had little effect, since the formation

(13) Mueller, C.; Brink, A.; Kilpinen, P.; Hupa, M.; Kremer, H. *Clean Air* **2002**, *3*, 145–163.
(14) Saario, A.; Oksanen, A. *Energy Fuels* **2008**, *22*, 297–305.
(15) Glarborg, P.; Bentzen, L. L. B. *Energy Fuels* **2007**, *22*, 291–296.
(16) Fluent 6.2 users guide, Fluent Inc., Centerra Resource Park, 10 Cavendish Court, Lebanon, NH 03766, 2005.
(17) Magnussen, B. F.; Hjertager, B. H. *Proc. Combust. Inst.* **1971**, *13*, 649–657.
(18) Gran, I.; Magnussen, B. F. *Combust. Sci. Technol.* **1996**, *119*, 171–190.
(19) Gran, I.; Magnussen, B. F. *Combust. Sci. Technol.* **1996**, *119*, 191–217.
(20) Lutz, A. E.; Kee, R. J.; Miller, J. A.;*Senkin: A Fortran Program for Predicting Homogeneous Gas Phase Chemical Kinetics With Sensitivity Analysis*, Report No. SAND87−8248 Laboratories, 1990.

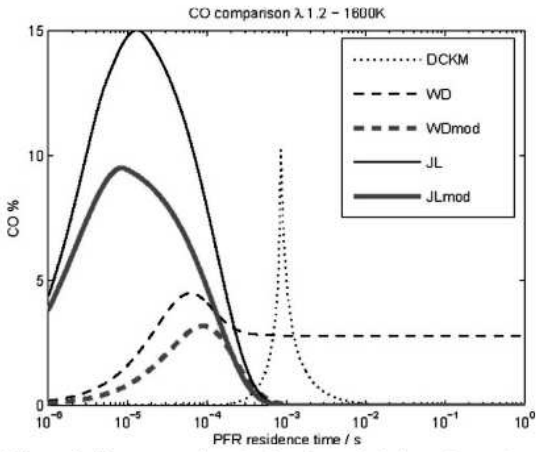

Figure 4. CO concentrations in plug flow calculations. Comparison between the DCKM, WD, JL, and modified mechanisms at 1600 K and $\lambda = 1.2$ under "oxy"-firing conditions (28% O_2 and 72% CO_2).

of H_2O (through JL3) became rate limiting. Consequently, predictions with the JL scheme were improved by modifying the rate coefficients for JL3, increasing the pre-exponential factor and decreasing the activation energy.

The parameters for the fuel-specific reactions were not part of the modification procedure; the kinetic data for the initiating reactions, i.e., (JL1), (JL2) and (WD1), were all retained. This is consistent with the flow reactor results of Glarborg and Bentzen[15] that indicate that the temperature for the initiation of reaction are very similar for reactive flows with and without CO_2. This implies that the main chemical difference between combustion in O_2/N_2 and O_2/CO_2 relates to the CO/H_2 reaction subset. Since the fuel-specific steps have been retained, the proposed schemes can easily be modified to describe higher hydrocarbons by adopting the appropriate rate data from the original mechanisms.[4,6] However, the inability of the global schemes to predict ignition timing has not been addressed.

PFR Tests of the Refined Schemes. The impact of the modifications on the CO prediction is illustrated in Figure 4 for lean conditions and 1600 K. The modification of the WD mechanism results in an improved prediction of the exit CO concentration, while the peak value is slightly lowered. The modified JL mechanism predicts a reduced peak CO level, due to the increased value of k_{JL3}. The major species concentrations predicted by the modified mechanisms are displayed in Figures 5 and 6. The results confirm that the modified schemes constitute an improvement over the WD and JL mechanisms for oxy-fuel conditions. Compared to the original schemes, the prediction in particular of the CO concentration has been improved. The improvement is most pronounced for the WD mechanism, which now predicts both the trend in CO and the approach to equilibrium concentrations reasonably well. For the modified JL mechanism, the predictions of the CO trend and the peak CO levels have been improved. Under fuel-rich conditions, both modified mechanisms approach steady-state concentrations reasonably well, as shown in Figure 6. This indicates that the schemes may be applied also for modeling staged or slightly understoichiometric combustion applications.

Figure 7 shows the performance of the modified global mechanisms when simulating a recirculated flue gas containing H_2O as well as CO_2; an option considered for oxy-fuel-fired power plants. Calculations were conducted for an oxidizer stream consisting of 28% O_2, 40% CO_2 and 32% H_2O instead of the 28% O_2 and 72% CO_2. The results confirm that the modified schemes predict the major species concentrations fairly well also under these conditions.

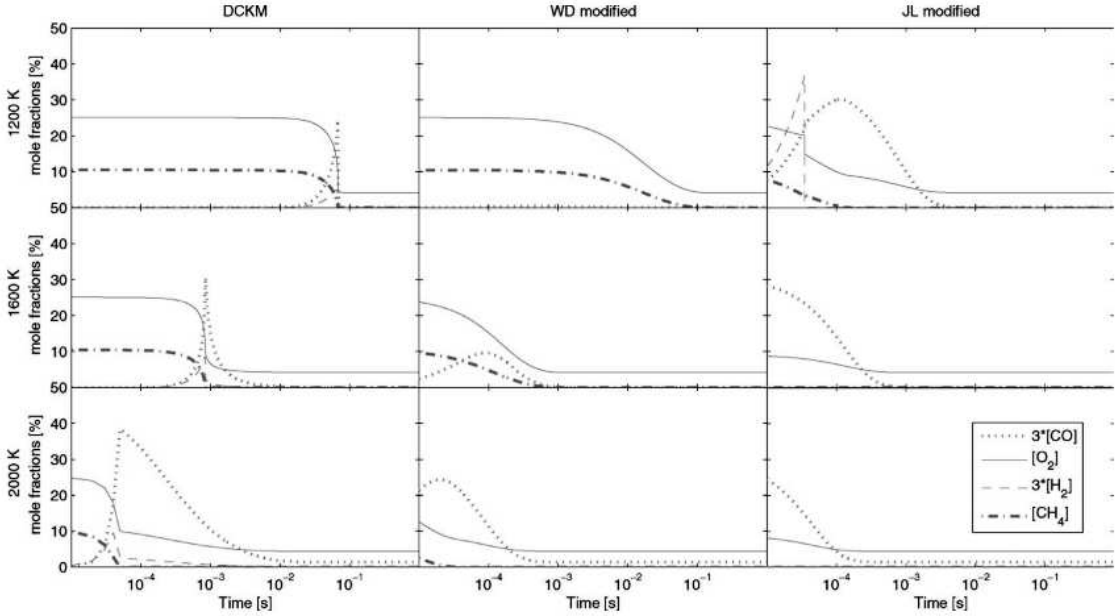

Figure 5. Major species concentrations in plug flow calculations. Comparison between the DCKM, the modified WD and the modified JL mechanisms at $\lambda = 1.2$ and 1200 K (top), 1600 K (middle), and 2000 K (bottom) under "oxy"-firing conditions (28% O_2 and 72% CO_2).

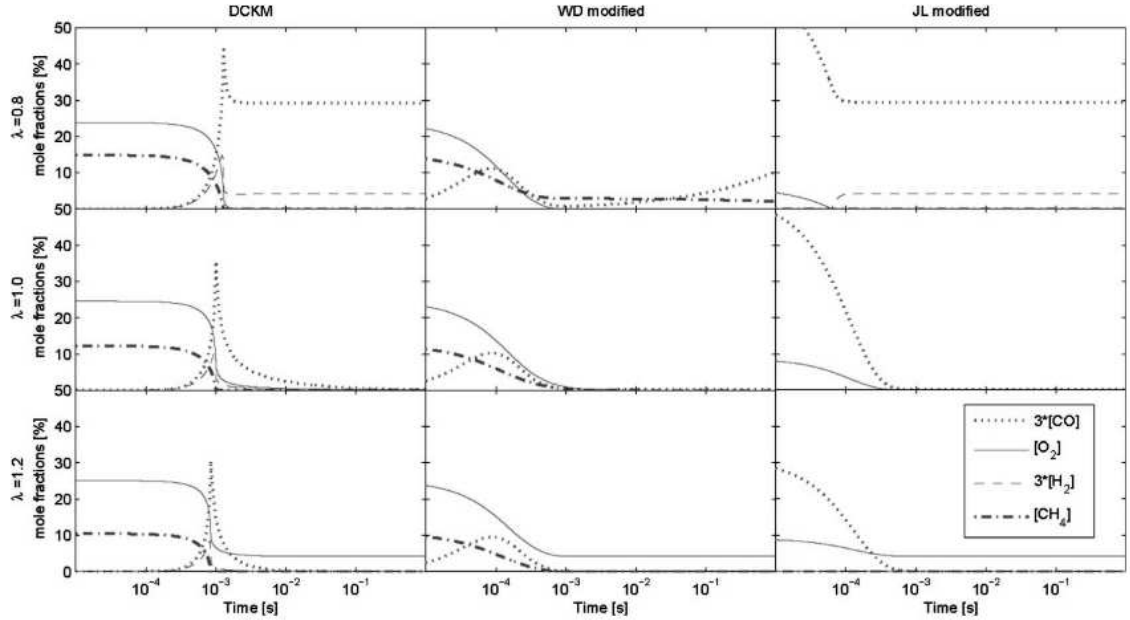

Figure 6. Major species concentrations in plug flow calculations. Comparison between the DCKM, the modified WD and the modified JL mechanisms at 1600 K and $\lambda = 0.8$ (top), $\lambda = 1.0$ (middle), and $\lambda = 1.2$ (bottom) under "oxy"-firing conditions (28% O_2 and 72% CO_2).

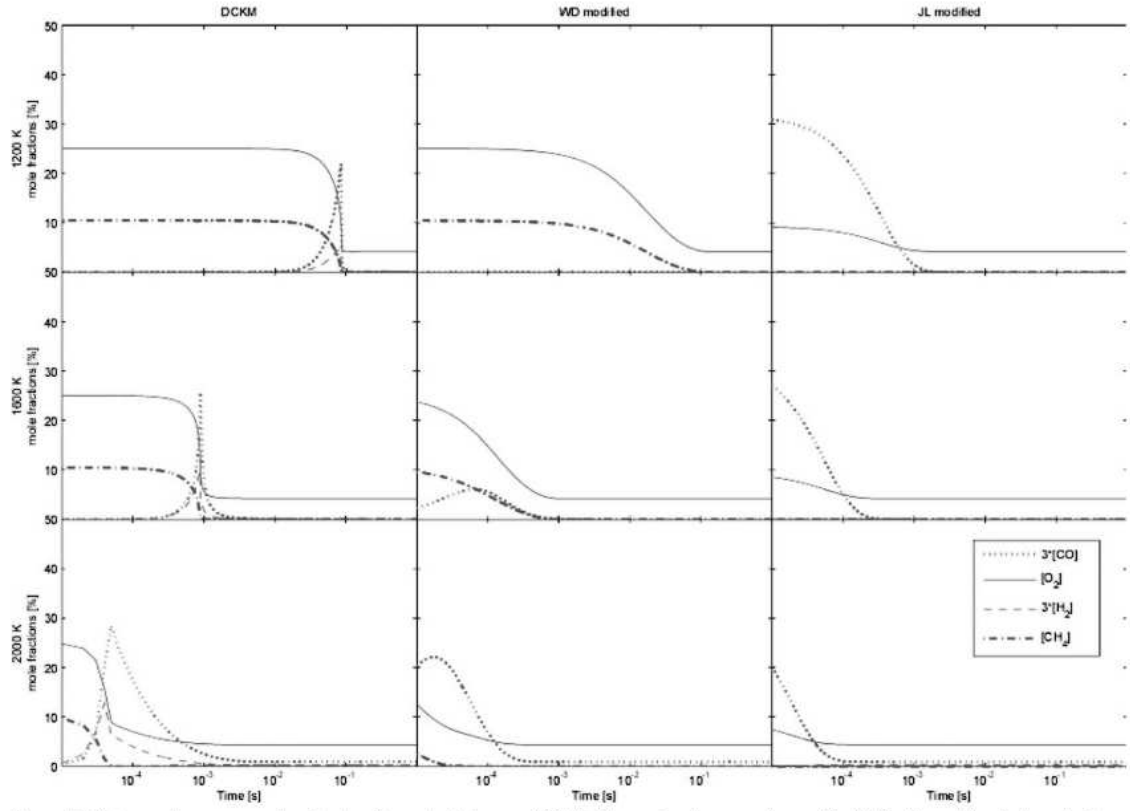

Figure 7. Major species concentrations in plug flow calculations at 1600 K. Comparison between the modified WD, JL, and detailed mechanisms under "oxy"-firing conditions with an oxidizer stream of 28% O_2, 40% CO_2 and 32% H_2O.

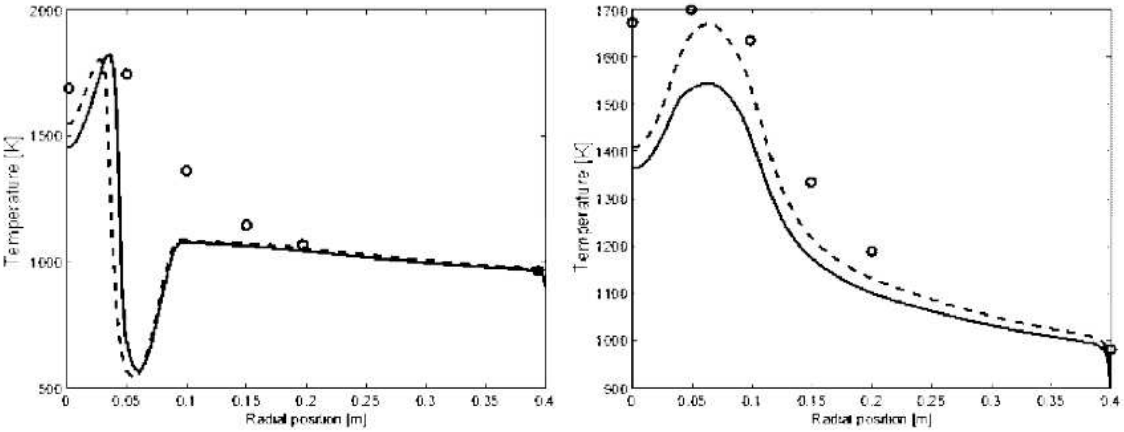

Figure 8. Temperature [K] Left: at 21.5 cm downstream of the burner. Right: at 38.4 cm downstream of the burner. Dots: Experimental data from Andersson and Johnsson.[1] Dashed line: Modified WD mechanism. Solid line: Original WD mechanism.

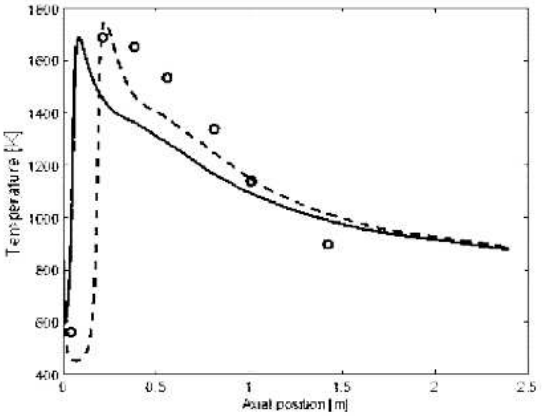

Figure 9. Temperature [K] Axial temperature at the centerline of the setup. Dots: Experimental data from Andersson and Johnsson.[1] Dashed line: Modified WD mechanism. Solid line: Original WD mechanism.

Table 5. Submodels and settings for the CFD analysis

grid	turbulence	radiation	chemistry interaction	mechanisms
2D 30.000 cells	realizable $k-\varepsilon$	P1	Eddy Dissipation concept	modified (Table *3*) original JL and WD (Tables *1,2*)

The turbulent mixing time scales applied in the individual CFD cells are of the order of 0.1−100 ms.[22] As expected, the modified mechanisms do not match the detailed mechanism on the smaller timescales. This implies that the global schemes have a limited accuracy in describing changes occurring on a small time scale or on an individual cell basis in a CFD computation. However, in terms of larger time scales or larger cell areas, the global mechanisms are capable of predicting satisfactorily the heat release and major species concentrations, provided the turbulence modeling provides accurate turbulence level predictions as input for the EDC turbulence chemistry interaction model.

CFD Modeling with the Refined Schemes. Recently, Andersson and Johnsson[1] reported measurements in a turbulent diffusion flame operated under oxy-fuel conditions. The experimental setup consisted of a 100 kW down-fired refractory lined furnace, with a swirl burner configuration. The fuel used was propane and the oxy-fuel experiments (27% oxygen in CO_2) were compared with data obtained in air. As part of the evaluation of the global schemes, we have conducted a CFD analysis the oxy-fuel flame. The geometry of the setup was simplified to a 2D case, even though the setup was not entirely axi-symmetric, due to four cooling tubes near the furnace walls. The heat loss to the cooling tubes was accounted for by applying a piecewise constant wall temperature to obtain gas temperatures near the walls in agreement with measurements. The grid was constructed with ~30.000 cells. A grid-independency check indicated that this grid size was sufficient.

The commercial CFD code Fluent was used for the calculation. The realizable $k-\varepsilon$ turbulence model was adopted along with the P1 radiation model. Second-order upwind discretization was used for all transported scalars. The CFD settings are summarized in Table 5. Both the Eddy Dissipation Model (EDM) and the Eddy Dissipation Concept (EDC) were applied in the modeling of the oxy-fuel flame. We recommend to use the EDC turbulence chemistry interaction model, when modeling oxy-fuel flames. The traditional "mixed-is-burned" approach offered by the EDM is not likely to be applicable in reaction systems where reverse reactions play an important role, as is the case under oxy-fuel conditions due to CO_2 decomposition at high temperatures. Limitations of the EDM model are discussed in more detail by Brink et al.[12]

The CFD results presented here were all performed using the EDC turbulence-chemistry interaction model, applying both the original WD and JL mechanisms and the modified versions suggested in Table 4. Since the fuel used in the experiments is propane, rate data and stoichiometric relationships for the initiating reactions (JL1, JL2, and WD1, see Table 4) were modified according to the original references.[4,6] These reactions are identical in the original and modified versions.

(21) Kee, R. J.; Rupley, F. M.; Miller, J. A.; Coltrin, M. E.; Grear, J. F.; Meeks, E.; Moffat, H. K.; Lutz, A. E.; Dixon-Lewis, G.; Smooke, M. D.; Warnatz, J.; Evans, G. H.; Larson, R. S.; Mitchell, R. E.; Petzold, L. R.; Reynolds, W. C.; Caracotsios, M.; Stewart, W. E.; Glarborg, P.; Wang, C.; Adigun, O.; Houf, W. G.; Chou, C. P.; Miller, S. F.; Ho, P.; Young, D. J.; CHEMKIN Release 4.0, Reaction Design, Inc., San Diego, CA (2004).

(22) Kjaldman, L.; Brink, A.; Hupa, M. *Combust. Sci. Technol.* **2000**, *154*, 207–227.

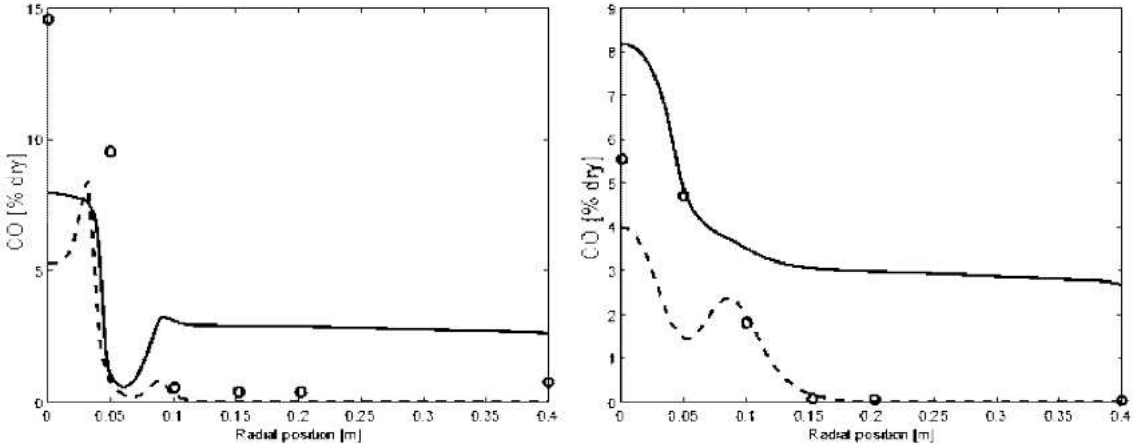

Figure 10. Radial CO concentration (%dry) Left: at 21.5 cm downstream of the burner. Right: at 38.4 cm downstream of the burner. Dots: Experimental data from Andersson and Johnsson.[1] Dashed line: Modified WD mechanism. Solid line: Original WD mechanism.

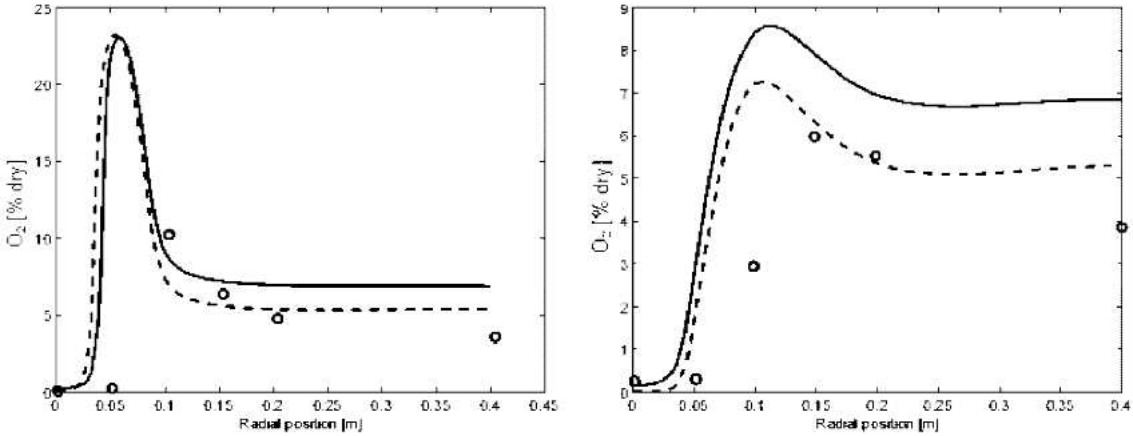

Figure 11. Radial O_2 concentration (%dry) Left: at 21.5 cm downstream of the burner. Right: at 38.4 cm downstream of the burner. Dots: Experimental data from Andersson and Johnsson.[1] Dashed line: Modified WD mechanism. Solid line: Original WD mechanism.

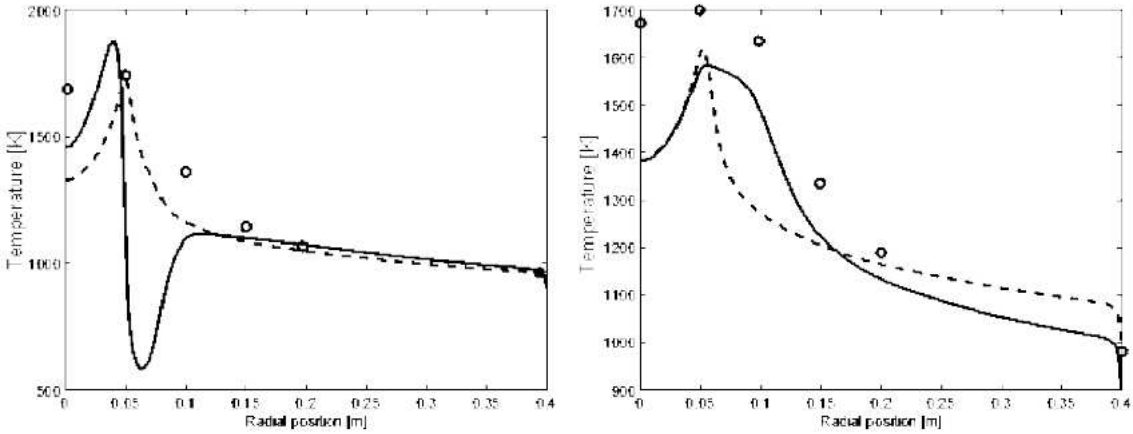

Figure 12. Temperature [K] Left: at 21.5 cm downstream of the burner. Right: at 38.4 cm downstream of the burner. Dots: Experimental data from Andersson and Johnsson.[1] Dashed line: Modified JL mechanism. Solid line: Original JL mechanism.

A satisfactory agreement between major species concentrations predicted by the CFD model and experimental results was achieved for the air case. Here, only results from the oxy-fuel case is presented. It should be noted that deviations

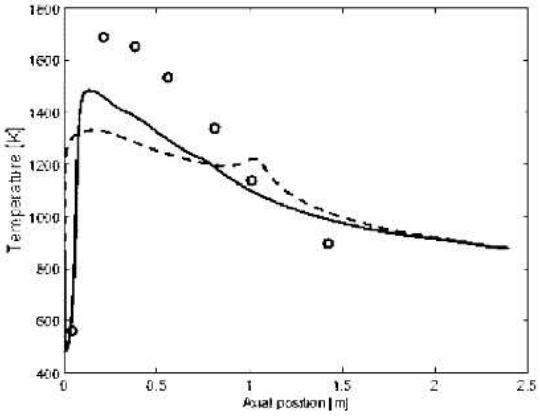

Figure 13. Temperature [K] Axial temperature at the centerline of the setup. Dots: Experimental data from Andersson and Johnsson.[1] Dashed line: Modified JL mechanism. Solid line: Original JL mechanism.

between the CFD predictions and the experimental results can only partly be attributed to an insufficient combustion mechanism. A satisfactory prediction of turbulence and flow field is essential; unfortunately, no data for velocity and velocity fluctuations are available from the oxy-fuel experiments. Radiative properties are also affected when changing from air to oxy-fuel combustion, and it is likely that differences in the temperature profiles are due to insufficient radiative modeling along with the simplifications in geometry (neglection of the cooling tubes). Furthermore, soot formation, which is important for the flame radiation, was not accounted for in the modeling.

Figures 8 and 9 show comparison between experimental results[1] and modeling predictions with the WD schemes for the radial and centerline temperature profiles, respectively, while Figures 10 and 11 show results for radial CO and O_2 concentrations. The CO and O_2 concentrations are shown for two measurement planes, 21.5 and 38.4 cm downstream of the burner. Solid lines denote calculations with the original WD scheme, while dashed lines donte predictions with the modified WD scheme. In general, the modified WD mechanism provides an improved prediction of both the temperature and the postflame conditions and emissions, compared to the original scheme. The modified mechanism predicts well the CO levels in the region outside the flame zone (Figure 10). The improvement can be attributed to the new equilib-

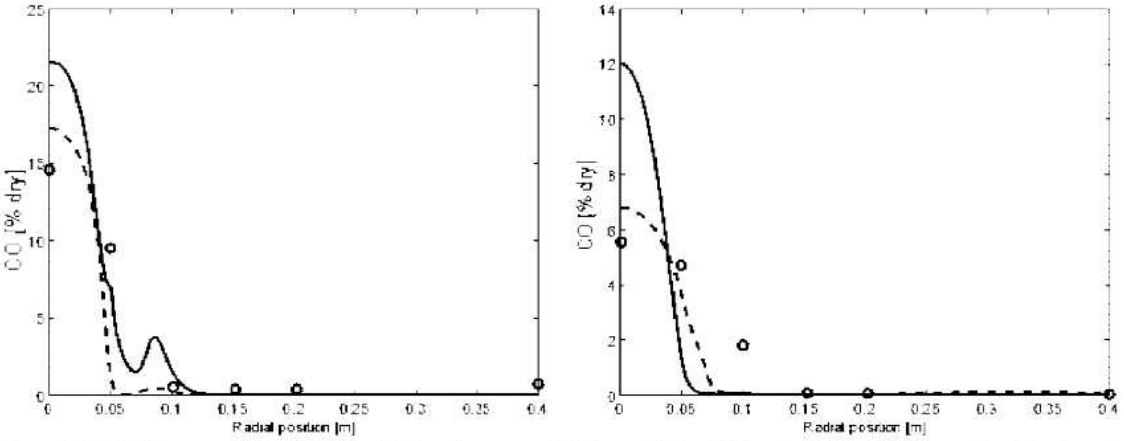

Figure 14. Radial CO concentration (%dry) Left: at 21.5 cm downstream of the burner. Right: at 38.4 cm downstream of the burner. Dots: Experimental data from Andersson and Johnsson.[1] Dashed line: Modified JL mechanism. Solid line: Original JL mechanism.

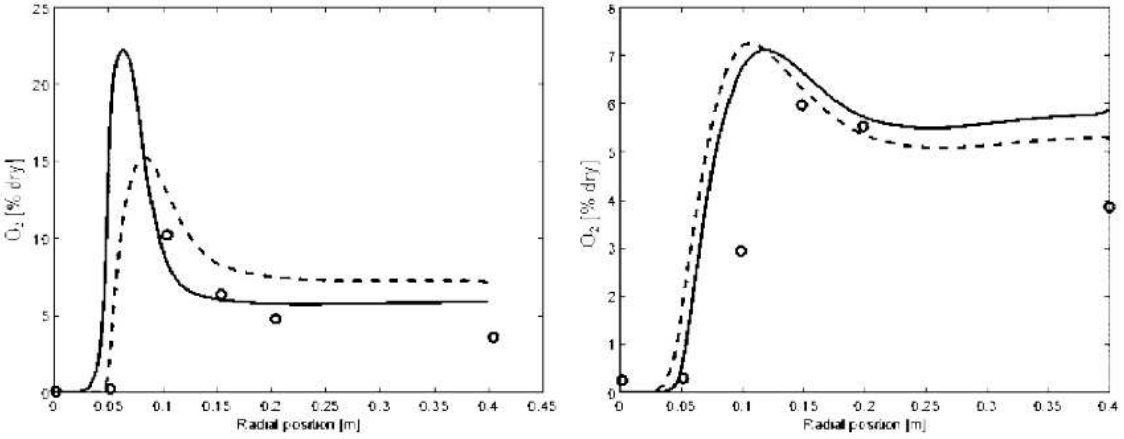

Figure 15. Radial O_2 concentration (%dry) Left: at 21.5 cm downstream of the burner. Right: at 38.4 cm downstream of the burner. Dots: Experimental data from Andersson and Johnsson.[1] Dashed line: Modified JL mechanism. Solid line: Original JL mechanism.

rium fit for the WD3 reaction. The modified model also predicts a different CO level in the flame zone, but due to the limited experimental data points for CO in this region, both sets of predictions are considered to be within experimental uncertainty. The differences in the predicted CO levels do, however, emphasize the importance of the chemical mechanism in the CFD computation. In the very fuel-rich parts of the flame, the CO levels are underpredicted in this CFD analysis. This indicates that it may be necessary to apply a more complex model than the WD scheme for reliable modeling of fuel-rich regions of a combustion system.

Comparisons for temperature profiles (Figures 12 and 13) and CO/O_2 concentrations prediction (Figures 14 and 15) have also been conducted for the JL schemes. Figures 14 and 15 compare CO and O_2 concentrations from the original JL mechanism and the modified mechanism with the experimental measurements at two measurement planes 21.5 and 38.4 cm downstream of the burner. From Figure 14, it can be seen that the modified JL mechanism predicts a lower CO concentration in the center of the furnace inside the flame, improving the agreement with experiment. The prediction of a lower CO level by the modified scheme is consistent with the PFR calculations discussed above. The modifications in the JL mechanism also induce changes in the temperature predictions (Figures 12 and 13) and the O_2 prediction (Figure 15), but whether these changes constitute improvements over the original mechanism cannot be concluded.

Conclusions

Two global multistep mechanisms, the two-step mechanism by Westbrook and Dryer and the four-step mechanism by Jones and Lindstedt, have been tested and refined for oxy-fuel conditions, based on comparison with model predictions with a detailed chemical kinetic mechanism. In the modification, the initiation reactions involving the hydrocarbon fuel were unaltered. Changes were made in the $CO-CO_2$ reaction subset to obtain an improved fit for CO levels and steady state emissions as predicted by the detailed mechanism.

The modified schemes provide improved agreement with the detailed mechanism compared to the original mechanisms for isothermal plug flow reactor modeling under oxy-fuel combustion conditions. The improvement was most pronounced for WD mechanism, where the modified scheme yielded a better prediction of the peak and exit concentrations of CO. The modified JL mechanism offers a slight improvement in predicting CO trends.

A CFD analysis of a propane oxy-fuel flame was performed using both the original and modified mechanisms. The modified JL mechanism performed slightly better than the original, regarding CO predictions in the flame zone. The modified WD mechanism improved the prediction of CO especially in the post flame zone, but also a better temperature agreement with experimental data was obtained. In general, it is recommended to use the EDC turbulence chemistry interaction model, when modeling oxy-fuel flames. The traditional "mixed is burned" approach offered by the Eddy Dissipation Model is not likely to be applicable in a combustion system where the CO_2 dissociation can have a significant chemical effect.

Acknowledgment. This work was funded by Vattenfall Research and Development AB with Karin Eriksson as project manager. The authors would like to thank Anders Brink and W.P. Jones for helpful discussions.

EF8003619

Appendix B

Experimental description

In order to be able to generate a computational mesh of the freeboard section, sketches with measures are stated here. The freeboard simulator consists of two natural gas fuel inlets the primary one provides fuel for a swirl stabilized flame, which is to simulate the burnout of biomass on a grate. The rest of the natural gas is let in further downstream to simulate the release of volatile gases from the fuel as illustrated in 2.1 on page 8. Notice that the gas flow is from the top and down in opposition to a full scale boiler. Figure 2.2 on page 9 sketches the key measures in the setup - all measures in mm.

B.1 Primary section - swirl burner

A swirl burner is mounted on top of the 1st stage reaction chamber; the entire top section of the setup is carried on from a previous setup, where this low NOx swirl burner was the essential part. The primary flame is caused by a swirl burner device (see Figure B.1), where the natural gas runs from the gas feeding system to the burner in the inner annular of the pipe, and

a swirling combustion air runs on the outer annular side meeting the fuel at the reactor chamber, as illustrated in. It is possible to supply the primary air in three different ways; as tangential air, as axial air or as feeder air. The tangential air provides the swirling motion which creates recirculation zones in the 1st stage of the reactor. The feeder air enters the burner mouth with a lower velocity than the tangential and axial air. Flow settings for air gas and ammonia during the two analysed conditions are summarized in Table B.1.

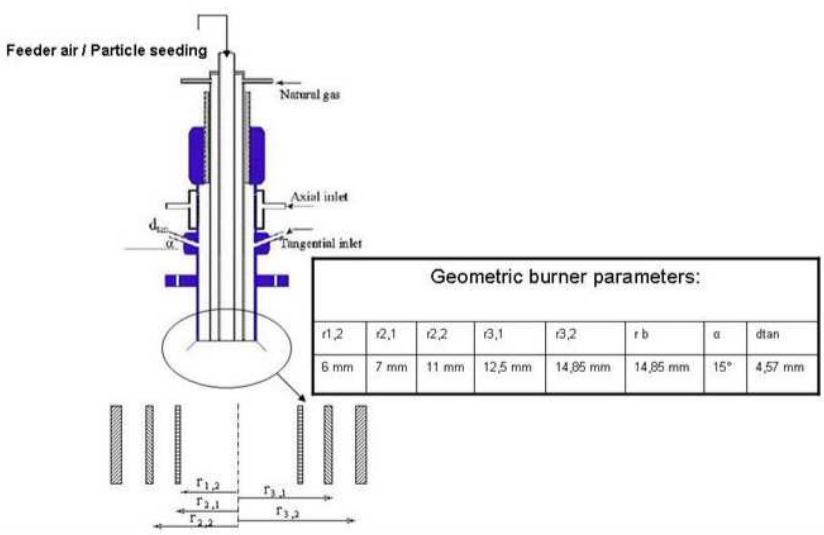

Figure B.1: Cross section of the swirl burner.

It is also possible to inject particles through the inner pipe along with the feeder air, this feature has previously been used for injecting coal or wood particles. In this study it was only used during the LDA measurements.

The secondary air inlet consists of 210 small holes with a diameter of 2.5 mm positioned in a circle 221 mm from the center axis. The secondary air enters the freeboard section in a 45 degree angle. The top freeboard section with

Table B.1: Flow boundary conditions.

Setting 1		
Primary gas flow	46.5	l/min @ 0°C 1atm
Secondary gas flow	22.3	l/min @ 0°C 1atm
Feeder air flow	100	l/min @ 0°C 1atm
Tangential air flow	330	l/min @ 0°C 1atm
Axial air flow	0	l/min @ 0°C 1atm
Secondary air flow	575	l/min @ 0°C 1atm
Ammonia added	18.5	l/min @ 0°C 1atm
Setting 2		
Primary gas flow	46.5	l/min @ 0°C 1atm
Secondary gas flow	22.3	l/min @ 0°C 1atm
Feeder air flow	100	l/min @ 0°C 1atm
Tangential air flow	330	l/min @ 0°C 1atm
Axial air flow	0	l/min @ 0°C 1atm
Secondary air flow	303	l/min @ 0°C 1atm
Ammonia added	18.5	l/min @ 0°C 1atm

the secondary air addition is sketched in Figure B.2.

The actual temperature of the secondary air entering the Freeboard section was measured by thermocouples in the air channel just before the inlet. The temperature varied from 300-350°C - in the calculation a temperature of 600K was applied. This heat up of the secondary air is caused by the process heating up the air channels of the secondary air. The primary air and both natural gas inlets are entering at ambient temperature, which is

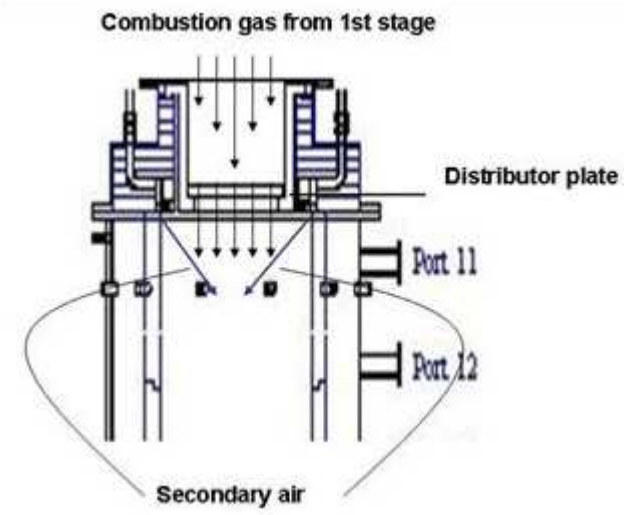

Figure B.2: Illustration of the top freeboard section with flow indications.

approximately 25-35°C.

Figure B.3displays the measures for the secondary air injection through 210 holes (ø2.5mm) in a radius of 221 mm from the centre of the reactor.

Figure B.4 displays the dimension of the flow sthraightner plate. The diameter of the individual 103 holes is 16 mm.

B.2 2D geometry

In order to construct a 2D mesh of the setup some measures are important:

Total assembly

The radius of the freeboard is: 245 mm and it is 1255mm long.

1st stage gas inlet

The radius of the 1st stage inlet gas is 135 mm.

Secondary air inlet

The secondary air is assumed added axisymmetric, so the area of the 210

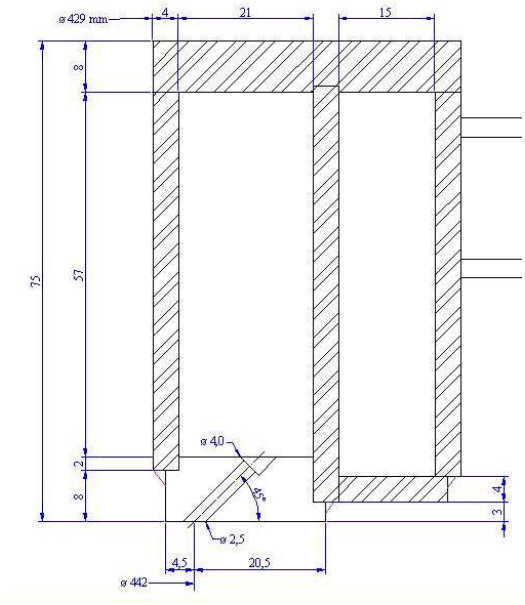

Figure B.3: Illustration of the secondary air inlet jets - measures in mm.

entrance holes is treated as a slit.

Slit area: $210 * (1,25mm)^2 * \pi = 1031mm^2$

Slit centre 221 mm from reactor centerline (24 mm from wall).

Slit radius = 0,371 mm (gives same total cross sectional area)

$(221 + 0,371)^2 * \pi - (221 - 0,371)^2 * \pi = 1031mm2$

The secondary air enters in a 45 degrees angle. In the presented results, the slit was extended 5mm into the furnace to avoid jet attachment.

Outlet In a 2D axi symmetric model the outlet can be chosen at the Ø300 constriction (see 2.2 on page 9).

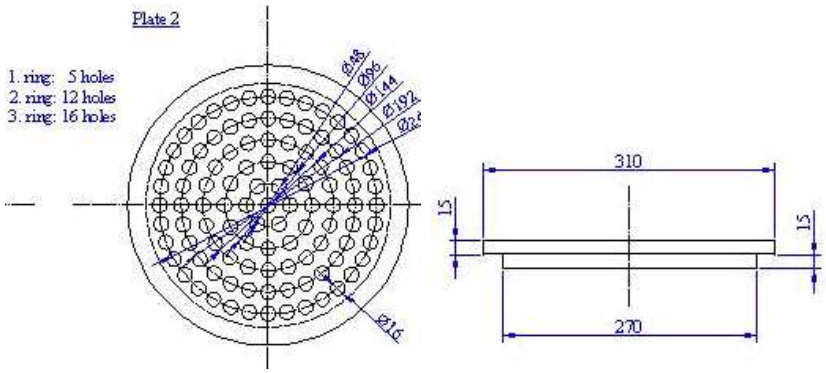

Figure B.4: Flow sthraigtner dimensions all measures in mm.

Appendix C

Measurement data - tabulated

This Appendix contains tabulated measurement data for the two experimental conditions analysed. Negative radial positions indicate far side measurements.

C.1 Setting 1 - high secondary air flow

Table C.1: O_2, CO and CO_2 % dry for setting 1

Rad. pos.	-240	-220	-200	-180	-160	-140	-120	-100	-80	-60	-40	-20	0	20	40	60	80	100	120	140	160	180	200	220	240
Traverse mm			O_2																						
88	6.7	6.75	6.8	7	7.2	8.1	8.1	7.8	2.7	4.4	4.4	4.9	4.5	4	6	5.4	5.2	6.2	7.3	9.1	8.5	7.8	7.4	7.6	7.8
188	6.7	6.75	6.8	6.65	6.5	6.55	6.6	7.1	7.6	6.6	5.6	5.5	5.4	5.5	5.6	5.95	6.3	6.85	7.4	7.4	7.4	7.4	7.4	7.35	7.3
288	6.8	6.85	6.9	6.7	6.5	6.75	7	7.05	7.1	7.2	7.3	6.95	6.6	6.45	6.3	6.35	6.4	6.55	6.7	6.95	7.2	7.25	7.3	7.4	7.5
388	6.8	6.8	6.8	6.75	6.7	6.65	6.6	6.65	6.7	6.7	6.7	6.7	6.7	6.65	6.6	6.7	6.8	6.85	6.9	7	7.1	7.15	7.2	7.25	7.3
488	6.9	6.8	6.7	6.65	6.6	6.5	6.4	6.4	6.4	6.4	6.4	6.4	6.4	6.4	6.4	6.4	6.4	6.45	6.5	6.65	6.8	6.85	6.9	7	7.1
688	6.9	6.8	6.7	6.65	6.6	6.55	6.5	6.5	6.5	6.5	6.5	6.5	6.5	6.5	6.5	6.5	6.5	6.45	6.4	6.5	6.7	6.75	6.8	6.7	6.7
788	6.9	6.8	6.7	6.6	6.5	6.45	6.4	6.4	6.4	6.45	6.5	6.45	6.4	6.45	6.5	6.5	6.5	6.5	6.5	6.5	6.6	6.7	6.8	6.8	6.8
988	7	6.9	6.8	6.7	6.6	6.6	6.6	6.6	6.6	6.6	6.6	6.6	6.6	6.6	6.6	6.6	6.6	6.6	6.6	6.65	6.7	6.7	6.7	6.85	7
Traverse mm			CO																						
88	0	0	0	0	0	0.01	0.07	0.1	0.4	0.3	0.3	0.28	0.36	0.35	0.13	0.13	0.08	0.04	0.05	0.05	0.04	0	0	0	0
188	0	0	0	0	0	0	0.01	0.02	0.02	0.02	0.02	0.04	0.05	0.06	0.06	0.04	0.02	0.01	0	0	0	0	0	0	0
288	0	0	0	0	0	0	0	0	0	0	0	0	0	0	0	0	0	0	0	0	0	0	0	0	0
388	0	0	0	0	0	0	0	0	0	0	0	0	0	0	0	0	0	0	0	0	0	0	0	0	0
488	0	0	0	0	0	0	0	0	0	0	0	0	0	0	0	0	0	0	0	0	0	0	0	0	0
688	0	0	0	0	0	0	0	0	0	0	0	0	0	0	0	0	0	0	0	0	0	0	0	0	0
788	0	0	0	0	0	0	0	0	0	0	0	0	0	0	0	0	0	0	0	0	0	0	0	0	0
988	0	0	0	0	0	0	0	0	0	0	0	0	0	0	0	0	0	0	0	0	0	0	0	0	0
Traverse mm			CO_2																						
88	7.2	7.25	7.3	7.4	7.5	6.9	6.9	7	9.8	8.9	8.8	9.6	8.8	8.5	8.1	8.4	8.9	8.1	7.3	6.5	6.7	7.2	7.4	7.25	7.1
188	7.3	7.3	7.4	7.45	7.5	7.55	7.6	7.35	7.1	7	6.9	7.22	7.54	7.87	8.2	8	7.8	7.5	7.2	7.15	7.1	7.15	7.2	7.2	7.2
288	7.5	7.45	7.4	7.5	7.6	7.65	7.7	7.65	7.6	7.45	7.3	7.4	7.5	7.7	7.9	7.85	7.8	7.7	7.7	7.5	7.4	7.3	7.3	7.25	7.2
388	7.5	7.5	7.6	7.6	7.7	7.75	7.8	7.65	7.5	7.4	7.4	7.35	7.3	7.3	7.4	7.4	7.5	7.5	7.6	7.4	7.3	7.3	7.3	7.25	7.2
488	7.7	7.7	7.7	7.7	7.7	7.7	7.7	7.7	7.7	7.7	7.7	7.7	7.7	7.7	7.7	7.7	7.7	7.7	7.7	7.6	7.5	7.4	7.4	7.35	7.3
688	7.6	7.6	7.6	7.6	7.7	7.7	7.7	7.7	7.7	7.7	7.7	7.7	7.7	7.7	7.7	7.675	7.65	7.65	7.65	7.6	7.55	7.5	7.5	7.5	7.4
788	7.6	7.6	7.6	7.65	7.7	7.7	7.7	7.7	7.7	7.7	7.7	7.7	7.7	7.7	7.7	7.7	7.6	7.6	7.6	7.6	7.6	7.6	7.6	7.5	7.5
988	7.4	7.5	7.5	7.6	7.6	7.6	7.6	7.6	7.6	7.65	7.7	7.7	7.7	7.7	7.7	7.6	7.6	7.6	7.6	7.6	7.6	7.6	7.6	7.5	7.4

Table C.2: NO [ppm dry], NH_3 [ppm] and temperatures for setting 1

Rad. pos.	-240	-220	-200	-180	-160	-140	-120	-100	-80	-60	-40	-20	0	20	40	60	80	100	120	140	160	180	200	220	240
Traverse mm			NO																						
88	170	167	165	174	183	166	175	171	203	201	206	208	209	210	206	205	202	184	163	143	144	182	170	175	181
188	172	176	180	188	196	202	208	207	206	214	223	224	225	222	220	220	220	214	208	204	201	194	187	188	190
288	189	190	191	196	201	208	214	213	211	209	206	207	207	211	214	212	210	208	205	202	199	199	199	195.5	192
388	206	208	210	212	214	212	211	210	209	206	204	202	200	204	209	206.5	204	205	205	206	207	205	204	203	202
488	208	209	210	212	214	213	212	212	212	211	210	210	210	210	210	210	209	207	206	206	207	204	202	200	198
688	208	209	210	212	214	214	214	213	213	213	212	212	213	212	212	212	211	210	209	209	208	207	206	204	203
788	207	209	210	212	213	214	215	215	214	214	214	215	215	215	214	214	213	212	211	211	210	210	209	208	208
988	202	203	205	206	206	207	207	207	208	208	208	208	208	208	207	207	206	206	205	205	204	205	205	203	200
Traverse mm			NH_3																						
88	4	4	4	4	5	6	12	14	53	47	56	42	68	45	57	20	12	5	4	4	4	4	4	4	4
188	2	2	2	2	2	2	2	2	2	2	2	2.5	3	3	3	3	3	2.5	2	2	2	2	2	2	2
288	2	2	2	2	2	2	2	2	2	2	2	2	2	2	2	2	2	2	2	2	2	2	2	2	2
388	2	2	2	2	2	2	2	2	2	2	2	2	2	2	2	2	2	2	2	2	2	2	2	2	2
488	2	2	2	2	2	2	2	2	2	2	2	2	2	2	2	2	2	2	2	2	2	2	2	2	2
688	2	2	2	2	2	2	2	2	2	2	2	2	2	2	2	2	2	2	2	2	2	2	2	2	2
788	2	2	2	2	2	2	2	2	2	2	2	2	2	2	2	2	2	2	2	2	2	2	2	2	2
988	2	2	2	2	2	2	2	2	2	2	2	2	2	2	2	2	2	2	2	2	2	2	2	2	2
Traverse mm			Temperature °C)																						
88	1032	1022	1019	1007	969	975	1026	1174	1197	1225	1205	1170	1177	1202	1168	1145	1083	1037	973	966	964	956	941		
188	1020	1022	1023	1024	1024	1020	1015	1009	1020	1050	1078	1103	1112	1110	1085	1063	1040	1026	1011	996	980	960	940		
288	1000	1005	1010	1012	1013	1019	1020	1021	1027	1036	1045	1049	1068	1065	1055	1025	1015	995	988	978	967	954	940		
388	1003	1014	1025	1028	1031	1034	1037	1041	1044	1050	1055	1063	1070	1069	1068	1065	1062	1048	1033	1022	1010	996	981		
488	1025	1029	1032	1034	1036	1040	1044	1048	1051	1054	1057	1063	1068	1065	1062	1063	1063	1060	1056	1045	1034	1021	1007		
688	1018	1024	1030	1033	1035	1039	1042	1045	1048	1051	1054	1056	1057	1057	1056	1053	1049	1046	1043	1038	1032	1020	1007		
788	1013	1015	1017	1021	1024	1028	1031	1035	1038	1040	1042	1044	1046	1045	1044	1042	1040	1040	1040	1035	1029	1017	1004		
988	1010	1012	1013	1016	1019	1022	1025	1027	1029	1030	1030	1031	1032	1033	1034	1034	1033	1035	1037	1029	1020	1010	1000		

Table C.3: Axial velocities and RMS axial velocities for setting 1

Radial pos.	-240	-200	-160	-120	-80	-40	0	40	80	120	160	200	240
Traverse mm			Axial velocity										
133	0	-0.5568	5.1264	5.0304	3.0144	2.208	2.208	2.9184	4.5696	6.6048	-0.384	-1.7088	-1.1904
373	0	0.1536	2.2272	3.6672	3.552	2.7456	2.7456	3.6096	1.7472	1.2672	-1.1712	-1.632	-0.2304
533	0.5184	0.2304	2.112	0.672	2.0352	1.6704	1.6704	1.2288	1.1328	0.3456	0.8832	0.3648	-0.192
733	0.0768	0.6144	0.7104	1.2096	1.2288	1.2672	1.2672	1.4016	1.3056	1.0368	1.0752	0.9984	-0.4224
893	0.2688	0.4032	0.6336	0.9792	0.9984	1.3632	1.3632	1.2288	1.0944	0.6528	0.8448	0.4608	0.1536
1110	0.0384	0.3456	0.7488	1.1712	1.4208	1.4784	1.4784	1.5552	1.4976	1.344	0.8064	0.5952	0.3264
Traverse mm			RMS										
133	0.0576	1.3632	2.8992	1.5552	1.4592	1.3056	1.3056	1.1136	1.2864	1.9776	1.9584	0.7104	0.576
373	0.0576	0.6144	1.1136	0.864	0.6528	0.48	0.48	0.672	3.4944	4.0128	1.5168	1.1712	0.5184
533	1.248	1.9008	1.7088	2.3424	1.9008	1.9968	1.9968	2.112	2.2464	1.6704	1.9776	1.2096	1.0176
733	0.9792	1.1712	1.3248	1.3056	1.3056	1.344	1.344	1.5168	1.4592	1.1136	1.0752	1.056	0.6528
893	0.4608	0.4416	0.6144	0.7296	0.8064	0.7296	0.7296	0.768	0.8256	0.768	0.7296	0.6144	0.48
1110	0.1536	0.2496	0.2688	0.2496	0.2688	0.2496	0.2496	0.2304	0.2304	0.2304	0.192	0.1344	0.192

C.2 Setting 2 - low secondary air flow

Table C.4: O_2, CO and CO_2 % dry for setting 2

Rad. pos.	-240	-220	-200	-180	-160	-140	-120	-100	-80	-60	-40	-20	0	20	40	60	80	100	120	140	160	180	200	220	240
Traverse mm			O_2																						
88	1.4	1.3	1.2	1.45	1.7	3.3	4.3	4	1.7	0.3	0.11	0	0	0	0	0.3	1.5	2.3	4.6	6	5.9	3.3	2.8	2.7	2.6
188	1.3	1.3	1.3	1.35	1.4	1.65	1.9	3.9	2.25	2.1	1.3	0.4	0.3	0.3	0.3	0.3	2.5	3.8	4.5	4.4	3.9	3.35	2.8	2.75	2.7
288	1.7	1.65	1.6	1.75	1.9	1.7	1.5	2.9	1.9	1.8	1.8	1.2	0.6	0.55	0.5	0.85	1.2	2.3	3	3.4	3.3	3.1	2.9	2.75	2.6
388	1	1	1	1.05	1.1	1.15	1.2	1.65	2.1	1.55	1	1.05	1.1	0.95	0.8	0.85	0.9	2.5	4.1	3.45	2.8	2.7	2.6	2.55	2.5
488	1	0.85	0.7	0.6	0.5	0.5	0.5	0.5	0.5	0.5	0.6	0.6	0.6	0.6	0.6	0.8	0.9	1.2	1.4	1.55	1.7	1.55	1.4	1.4	1.4
688	0.9	0.8	0.7	0.65	0.6	0.6	0.6	0.55	0.5	0.55	0.6	0.6	0.6	0.6	0.6	0.65	0.7	0.75	0.8	0.8	0.8	0.9	1	1.05	1.1
788	0.7	0.7	0.7	0.7	0.7	0.65	0.6	0.6	0.6	0.6	0.6	0.6	0.6	0.6	0.6	0.6	0.6	0.65	0.7	0.7	0.7	0.7	0.7	0.75	0.8
988	0.8	0.8	0.8	0.75	0.7	0.7	0.7	0.7	0.7	0.7	0.7	0.7	0.7	0.7	0.7	0.7	0.7	0.7	0.7	0.7	0.7	0.75	0.8	0.85	0.9
Traverse mm			CO																						
88	0.00	0.00	0.00	0.04	0.07	0.02	0.02	0.40	1.30	1.80	2.50	2.70	2.80	2.90	3.00	2.50	2.10	0.95	0.34	0.09	0.02	0.00	0.00	0.00	0.00
188	0.00	0.00	0.00	0.00	0.00	0.00	0.00	0.10	0.18	0.12	0.90	1.00	1.40	2.10	1.95	1.10	0.58	0.17	0.06	0.01	0.00	0.00	0.00	0.00	0.00
288	0.00	0.00	0.00	0.00	0.00	0.05	0.10	0.15	0.20	0.70	1.20	1.30	1.40	1.15	0.90	0.42	0.19	0.90	0.01	0.01	0.01	0.01	0.01	0.01	0.01
388	0.00	0.00	0.00	0.00	0.00	0.00	0.00	0.08	0.15	0.28	0.40	0.60	0.80	0.78	0.75	0.53	0.30	0.02	0.01	0.00	0.00	0.00	0.00	0.00	0.00
488	0.00	0.00	0.00	0.00	0.00	0.00	0.00	0.04	0.07	0.11	0.15	0.26	0.36	0.39	0.40	0.40	0.35	0.28	0.25	0.17	0.08	0.04	0.01	0.00	0.00
688	0.00	0.00	0.00	0.00	0.00	0.00	0.00	0.01	0.01	0.02	0.02	0.04	0.05	0.05	0.04	0.06	0.07	0.04	0.01	0.01	0.01	0.00	0.00	0.00	0.00
788	0.00	0.00	0.00	0.00	0.00	0.00	0.00	0.00	0.00	0.00	0.00	0.00	0.00	0.00	0.00	0.00	0.00	0.02	0.04	0.02	0.00	0.00	0.00	0.00	0.00
988	0.00	0.00	0.00	0.00	0.00	0.00	0.00	0.00	0.00	0.00	0.00	0.00	0.00	0.00	0.00	0.00	0.00	0.00	0.00	0.00	0.00	0.00	0.00	0.00	0.00
Traverse mm			CO_2																						
88	10.3	10.4	10.4	10.5	10.6	9.8	9.2	9.1	9.7	9.7	9.6	9.5	9.4	9.4	9.3	9.5	9.6	9.6	8.8	8.2	8.3	9.8	10.2	10.3	10.3
188	10.4	10.5	10.6	10.6	10.5	10.9	11.2	9.5	10.3	10.3	10.2	10.1	9.9	10.0	10.0	9.9	9.8	9.4	9.1	9.2	9.5	9.9	10.2	10.2	10.1
288	10.8	10.8	10.8	10.8	10.7	10.7	10.6	10.5	10.4	10.4	10.3	10.2	10.0	10.1	10.1	10.1	10.1	9.9	9.7	9.6	9.6	9.8	10.0	10.1	10.1
388	10.9	11.0	11.0	11.0	11.0	11.0	11.0	10.9	10.8	10.7	10.6	10.5	10.4	10.4	10.3	10.3	10.2	9.2	8.1	9.0	9.8	9.9	10.0	10.0	10.0
488	10.7	10.6	10.4	10.8	11.2	11.2	11.2	11.2	11.1	11.1	11.0	11.0	10.9	10.8	10.8	10.7	10.7	10.6	10.6	10.5	10.4	10.5	10.6	10.6	10.6
688	11.0	11.1	11.1	11.1	11.1	11.2	11.2	11.2	11.2	11.2	11.1	11.1	11.0	11.0	11.0	11.1	11.1	11.1	11.0	11.0	11.0	11.0	11.0	11.0	11.0
788	11.1	11.1	11.1	11.1	11.1	11.1	11.1	11.1	11.1	11.1	11.1	11.1	11.1	11.1	11.1	11.1	11.1	11.1	11.0	11.0	11.0	11.0	11.0	11.0	11.0
988	11.1	11.1	11.1	11.1	11.1	11.1	11.1	11.1	11.1	11.1	11.1	11.1	11.1	11.1	11.1	11.1	11.0	11.0	11.0	11.1	11.1	11.1	11.1	11.1	11.1

Table C.5: NO [ppm dry] and NH_3 [ppm] for setting 2

Rad. pos.	-240	-220	-200	-180	-160	-140	-120	-100	-80	-60	-40	-20	0	20	40	60	80	100	120	140	160	180	200	220	240
Traverse mm			NO																						
88	145	134	123	123	122	104	103	110	125	107	88	74	59	52	45	73	100	135	131	128	134	162	163	162	161
188	160	158	156	151	145	144	143	142	141	144	146	121	95	103	110	126	142	149	152	155	159	165	171	167	163
288	161	163	165	164	163	160	156	157	158	156	154	154	154	142	130	142	154	167	169	167	172	176	179	178	176
388	160	162	164	164	164	159	153	155	157	158	159	159	158	155	151	154	157	154	150	158	166	168	169	168	166
488	160	158	155	155	155	155	154	155	155	156	156	155	154	153	152	153	154	158	162	164	165	165	165	163	161
688	160	161	161	160	159	160	160	160	160	160	160	160	160	160	160	161	161	162	162	164	165	163	161	161	161
788	164	164	164	163	162	163	163	163	163	164	165	166	167	166	165	165	165	165	165	165	164	163	162	162	161
988	167	166	165	165	165	165	165	165	165	166	167	169	171	171	170	170	170	170	169	169	169	168	166	165	163
Traverse mm			NH_3																						
88	5	6	7	7	6	5	16	44	180	300	300	300	300	300	300	300	160	195	37	8	6	3	4	4	4
188	5	6	7	7	7	7	7	15	23	117	210	230	250	225	200	134	67	23	20	11	9	9	9	9	9
288	5	4	2	3	4	7	9	23	37	64	90	105	120	128	135	61	30	13	8	8	7	8	8	8	8
388	5	6	6	6	5	10	14	27	40	52	63	87	110	99	88	59	30	26	22	8	8	8	8	7	5
488	4	4	4	5	5	6	6	10	13	14	15	20	26	31	35	39	29	22	16	13	10	8	5	5	4
688	4	4	4	4	4	4	4	4	4	4	4	5	5	5	5	5	5	5	4	4	4	4	4	4	4
788	4	4	4	4	4	4	4	4	4	4	4	5	5	5	5	5	5	5	5	5	5	5	5	5	5
988	4	4	4	4	4	4	4	4	4	4	4	4	4	4	4	4	4	4	4	4	4	4	4	4	4
Traverse mm			Temperature (°C)																						
88	1114	1119	1123	1109	1095	1132	1220	1189	1175	1166	1158	1134	1132	1122	1160	1217	1246	1173	1069	1075	1085	1080	1082		
188	1145	1150	1155	1157	1158	1160	1162	1173	1203	1215	1202	1195	1193	1197	1213	1247	1195	1160	1125	1123	1120	1114	1107		
288	1160	1165	1169	1171	1173	1179	1184	1189	1194	1202	1209	1210	1211	1207	1202	1183	1164	1153	1142	1135	1127	1118	1109		
388	1164	1173	1182	1189	1195	1202	1208	1217	1225	1234	1243	1246	1249	1247	1245	1226	1207	1190	1173	1154	1134	1113	1092		
488	1168	1174	1179	1182	1185	1187	1189	1197	1204	1208	1211	1213	1214	1211	1207	1190	1173	1171	1168	1157	1145	1129	1113		
688	1156	1167	1177	1181	1184	1193	1201	1203	1205	1209	1213	1213	1212	1210	1207	1203	1199	1191	1183	1174	1165	1148	1130		
788	1158	1158	1158	1159	1160	1164	1168	1174	1180	1188	1195	1190	1185	1183	1180	1176	1171	1168	1164	1142	1119	1114	1109		
988	1140	1135	1129	1133	1136	1138	1140	1143	1145	1148	1150	1149	1148	1148	1147	1144	1140	1124	1107	1091	1075	1062	1048		

Table C.6: Axial velocities and RMS axial velocities for setting 1

Radial pos.	-240	-200	-160	-120	-80	-40	0	40	80	120	160	200	240
Traverse mm			Axial velocity										
133	0	-0.9792	1.5744	3.2832	2.4576	1.4016	1.4016	1.2288	2.3232	4.3392	0.2688	-0.7296	-0.1728
373	0	0.1536	2.2272	3.6672	3.552	2.7456	2.7456	3.6096	3.2064	0.96	-0.6144	-1.3824	-0.576
533	0.0576	0.9024	1.2288	1.7664	1.7088	2.2464	2.2464	1.8816	0.9984	0.192	0.4992	-0.8064	-0.7296
733	0.0384	0.6336	0.7872	1.1904	0.7488	1.1328	1.1328	1.0176	0.768	1.1328	1.1328	0.768	-0.2112
893	0	0.0576	0.6528	0.7296	0.8256	0.864	0.864	0.8064	0.6336	0.4992	0.4608	0.5184	0.2112
1110	0	0.1344	0.7488	0.9792	0.9216	1.2288	1.2288	0.9408	0.96	2.1504	1.0752	0.7104	0.096
Traverse mm			RMS										
133	0.0768	0.8064	1.7664	0.9984	0.672	0.48	0.48	0.3648	0.6336	1.1328	1.056	0.48	0.3456
373	0.0576	0.6144	1.1136	0.864	0.6528	0.48	0.48	0.672	1.0944	1.3632	1.0752	0.7104	0.4224
533	0.384	0.7872	0.9024	0.9792	0.9792	0.6912	0.6912	0.96	1.0368	0.9792	1.056	0.5568	0.384
733	1.0176	1.0944	1.1328	1.248	1.4208	1.3248	1.3248	1.3248	1.2288	1.4208	1.1328	0.9024	0.7104
893	0	0.192	0.3264	0.4032	0.4608	0.4416	0.4416	0.4416	0.384	0.3456	0.3072	0.288	0.1344
1110	0.0384	0.4992	0.7872	0.864	0.768	0.96	0.96	0.768	0.7872	0.9792	0.8256	0.768	0.3648

Appendix D

NO_X UDFs

The Fluent User Defined Function (UDF) used to implement the NO mechanism within the EDC framework is presented in listing D.1. The approach for implementing this mechanism (or any of the global NO mechanisms) on a combustion solution is as follows:

- In the materials data panel import the N-species NH_3 and NO.
- Remember to relocate N_2 as the last (bulk) specie and patch the concentration of the new N-species in N_2's old position to 0. Check that the N_2 concentration is as before the N-species imports.
- In Define->User-Defined->Functions compile and load the UDF.
- In Define->User-Defined->Function hooks enable the the UDF.
- Under Solve->Controls disable all but species transport equations, and set appropriate under-relaxation factors (suggesting 0.001 for the already solved species and 0.95 for the new N-species).
- Define boundary conditions for the new N-species.

- Define new monitors and custom field functions as desired and start solving.

The UDF used to implement the same mechanism in the framework of the Fluent standard NO_x postprocessor is stated in listing D.2. The approach taken to apply this mechanism is as stated in the Fluent manual - the main steps are restated here:

- Enable the Eddy Dissipation turbulence chemistry interaction model instead of EDC.
- Enable the NO model for Fuel NO
- In Define->User-Defined->Functions compile and load the UDF.
- In Define->Models->species->NOx enable Fuel NOx and enable the UDF.
- In Define->Models->species->NOx enable choose appropriate turbulence interaction parameters.
- Under Solve->Controls disable all but N-species transport equations, and set appropriate under-relaxation factors.
- Define boundary conditions for the new N-species.
- Define new monitors and custom field functions as desired and start solving.

Listing D.1: UDF for implementing the LSP NO mechanism in Fluent - used for approach where NO is calculated within the EDC turbulence-chemistry framework

```
#include "udf.h"
#include "math.h"
/*****************************************************************************/
/* This UDF defines reaction rates for the species NO and NH3. HCN is outcommented  */
/* It is based on:                                                           */
/* "Pedersen, L. S., Glarborg, P. and Dam-Johansen, K. 1998."                */
/* "A Reduced Reaction Scheme for Volatile Nitrogen Conversion in Coal Combustion." */
/* "Combustion Science and Technology. 1998, 131, pp. 193-196."              */
/*                                                                           */
/*Species listing:                                                           */
/*0:CH4 1:O2 2:CO2 3:CO 4:H2O 5:H2 6:H 7:OH 8:O 9:CH3 10:HCO 11:HO2         */
/*12:H2O2 13:CH2O 14:CH3O 15:NH3 16:NO 17:N2                                */
/*If your species composition deviate or appear in another order in your Fluent case*/
/* alternation should be made in lines 20-21 and 105-112                    */
/*****************************************************************************/
DEFINE_NET_REACTION_RATE(LSP,c,t,particle,pressure,temp,yi,rr,jac)
{

/*Variables for computing Molar weights and variables used to find the concentration of species*/
    double m_w[18] = {16.04, 32.0, 44.0, 28.0, 18.02, 2.02, 1.01, 17.02,
    16.0, 15.0, 29.02, 32.99, 34.0, 30.01, 31.01, 17.03, 30.0, 28.01};
    double Rgas, rho;
    int i, j;

/*The variables for the non steady state species that are provided by the combustion calculations*/
    double C_O2, C_H2O, C_H2, C_N2, C_O, C_OH, C_H;

/*The total concentration is computed from the ideal gas law. Pressure / R * Temperature.
Again the unit is mole/cm^3*/
    double C_M = *pressure / (1000 * UNIVERSAL_GAS_CONSTANT * *temp);

/*The arrays for the constants for the k-values are initialized*/
    double k_f[37];
    double k_K[37];

/*The variables for the concentration of NO, HCN, NH3*/
    double C_NO, C_HCN, C_NH3;

```

```
/*The variables for the steady state and equilibrium species are initialized*/
        double C_HOCN, C_CN, C_NCO, C_HNCO, C_NH, C_NH2, C_N;

/*The variables for the reaction rates for the reactions of the mechanism*/
        double w_1, w_2, w_3, w_4, w_5, w_15, w_16, w_18, w_21, w_22;
        double w_23, w_26, w_27, w_28, w_30, w_31, w_33, w_34, w_35, w_36;
        double rr_N2;

/*The variables for intermediates used to compute the steady state species are
    initialized*/
        double HOCN_upper, HOCN_lower, CN_upper, CN_lower, D_NCO, N1_NCO, N2_NCO, D_HNCO
            ,N1_HNCO,
                N2_HNCO, D_NH2, N1_NH2, N2_NH2, D_NH, N1_NH, N2_NH, N3_NH, D_N, N1_N, N2
                    _N,
                C_NH_upper, C_NH_lower;


/*Constants for the rate constants for the forward reaction of the 36 reactions in the
    mechanism*/
        double Cons_k_A[37] = {0, 3.6e8, 1.4e4, 3.5e3, 8e12, 5.9e4, 2e7, 1.5e4, 6.4e5, 6
            e13,
                7.5e12, 6.4e5, 7.6e2, 3.1e16, 5e13, 4.7e13, 1.4e18, 1.1e16, 1e12, 2.2e7,
                    9.6e7,
                2.2e16, 2.0e6, 6.4e5, 4e13, 4e6, 1.3e16, 4.6e5, 1.3e6, 3e13, 9.2e13, 2
                    e13, 5e11,
                2.9e14, 3.8e13, 6.4e9, 3.3e12};

        double Cons_k_b[37] = {0, 1.55, 2.64, 2.64, 0, 2.4, 2.0, 2.64, 2.0, 0, 0, 2, 3,
            -0.5, 0,
                0, -1.73, 0, 0, 1.7, 1.41, 0, 2.04, 2.39, 0, 2, -1.25, 2, 1.5, 0, 0, 0,
                    0.5,
                -0.4, 0, 1, 0.3};

        double Cons_k_E[37] = {0, 3000, 4980, 4980, 7450, 12500, 2000, 4000, 2560, 0,
            -389, 2560,
                4000, 48000, 0, 0, 763, 86000, 35000, 3800, 8520, 93470, 566, 10171,
                    3650, 1000,
                0, 6500, 100, 0, 0, 0, 2000, 0, 0, 6280, 0};

/*Constants for the equilibrium constants for the 36 reactions in the mechanism*/

        double Cons_EQ_A[37] = {0, 0.1184e-3, 0, 0, 0.8317e-2, 0.22e-1, 0, 0, 0, 0, 0, 0
            .4231e0,
                0.3365e-1, 0, 0, 0, 0, 0, 0, 0, 0, 0.1629e7, 0.9605e2, 0.6746e4, 0.3367
                    e2, 0.4794e0,
                0, 0, 0, 0.8079e0, 0, 0, 0.1150e-1, 0, 0.2745e-1, 0.1066e2, 0.5007e0};

        double Cons_EQ_b[37] = {0, 0.9545, 0, 0, 0.6244, 0.1689, 0, 0, 0, 0, 0, -0.4127e
            -1, 0.3713,
                0, 0, 0, 0, 0, 0, 0, 0, 0.2232, -0.4878, -0.8179, -0.3772, -0.4711e-1,
                    0, 0, 0, -0.1602,
                0, 0, 0.1699, 0, 0.3095, -0.9635e-1, -0.9698e-1};
```

```
77
        double Cons_EQ_E[37] = {0, 0.1065e5, 0, 0, 0.2599e4, -0.3764e4, 0, 0, 0, 0, 0, 0
            .3862e4, 0.4190e4,
79                  0, 0, 0, 0, 0, 0, 0, 0, -0.5558e5, 0.4984e4, -0.3068e4, 0.5764e4, 0.1382
                        e5, 0, 0, 0,
                    0.1212e5, 0, 0, 0.2017e5, 0, 0.2458e5, 0.1593e5, 0.3771e5};
81
    /*The forward rate constants and the equilibrium constants are computed*/
83  /*The k-values for the forwards reactions and the equilibrium K of the mechanism are
        computed from
        k = B * T^n * exp(-E / RT). The UNIVERSAL_GAS_CONSTANT needs to be defined in
            cal/ (mole*K).
85      Since the E-values used to compute the rate constants are given i cal/mole.
            Hence the multiplication
        with 0.23885 in the denomenator (joule to cal)*/
87                          for (i=0; i <= 36; i++)
                            {
89                              k_f[i] = Cons_k_A[i] * pow( *temp, Cons_k_b[i]) * exp(-
                                    Cons_k_E[i] * 1000 /
                                        (0.23885 * UNIVERSAL_GAS_CONSTANT * *temp));
91                              k_K[i] = Cons_EQ_A[i] * pow(*temp , Cons_EQ_b[i]) * exp(
                                    Cons_EQ_E[i] / *temp);
                            }
93
    /*The local density must be found in order to find the concentrations*/
95      Rgas = 0.;
        i = 0;
97  spe_loop(i,n_spe)
                Rgas += yi[i] / m_w[i];
99  Rgas *= UNIVERSAL_GAS_CONSTANT;
    rho = *pressure / (Rgas * *temp);
101

103 /*The concentrations of the seven active species which are computed in the main
        equationssystem
        are determined in mole/cm^3 as these are the units of the k constants. It is
            computed as
105     density_total * massfraction_species_i / (10^3 * Molarmass_species_i). */
                        C_H2 = MAX( 1.e-28, rho * yi[5] / (1000 * m_w[5]));
107                     C_H2O = MAX( 1.e-28, rho * yi[4] / (1000 * m_w[4]));
                        C_O2 = MAX( 1.e-28, rho * yi[1] / (1000 * m_w[1]));
109                     C_N2 = MAX( 1.e-28, rho * yi[17] / (1000 * m_w[17]));
                        C_H = MAX( 1.e-28, rho * yi[6] / (1000 * m_w[6]));
111                     C_O = MAX( 1.e-28, rho * yi[8] / (1000 * m_w[8]));
                        C_OH = MAX( 1.e-28, rho * yi[7] / (1000 * m_w[7]));
113 /*And the concentration of NO, HCN and NH3 in mole / cm3*/
                        C_NO = MAX( 1.e-28, rho * yi[16] / (1000 * m_w[16]));
115                     C_HCN = 0; /* If HCN is included it should be defined here
                            accordingly*/
                        C_NH3 = MAX( 1.e-28, rho * yi[15] / (1000 * m_w[15]));
117
```

```
119
    /*The steady state species HOCN, CN, NCO, HNCO, NH, NH2 and N are computed*/
121 /*The HOCN concentration is computed based on steady state*/
                            HOCN_upper = k_f[5] * C_HCN * C_OH;
123                         HOCN_lower = (k_f[5] / k_K[5]) * C_H +  k_f[6] * C_H + k_f[7] *
                                C_O + k_f[8] * C_OH;
                            if (HOCN_lower == 0)
125                         {
                                    HOCN_lower = 1.e-20;
127                         }
                            C_HOCN = HOCN_upper / HOCN_lower;
129
    /*The CN concentration is computed based on steady state*/
131                         CN_upper = (k_f[1] / k_K[1]) * C_HCN * C_H  + (k_f[4] / k_K[4])
                                * C_HCN * C_OH;
                            CN_lower = k_f[1] * C_H2 + k_f[4] * C_H2O + k_f[9] * C_OH + k_f[
                                10] * C_O2;
133                         C_CN = CN_upper / CN_lower;

135 /*The NCO concentration is computed based on steady state*/
                            D_NCO = (k_f[11] / k_K[11]) * C_H2O + k_f[12] * C_H2 + k_f[13] *
                                 (C_M + C_N2 * (1.5 - 1)) + k_f[14] * C_H + k_f[15] * C_O +
                                k_f[16] * C_NO;
137                         N1_NCO = C_HOCN * ( k_f[7] * C_O + k_f[8] * C_OH ) + C_CN * ( k_
                                f[9] * C_OH +  k_f[10] * C_O2 ) + k_f[2] * C_HCN * C_O;
                            N1_NCO = N1_NCO / D_NCO;
139                         N2_NCO = k_f[11] * C_OH + (k_f[12] / k_K[12]) * C_H;
                            N2_NCO = N2_NCO / D_NCO;
141
                            D_HNCO = k_f[11] * C_OH + (k_f[12] / k_K[12]) * C_H + k_f[17] *
                                (C_M + C_N2 * (1.5 - 1)) + k_f[18] * C_O2 + k_f[19] * C_H +
                                k_f[20] * C_O;
143                         N1_HNCO = (k_f[6] * C_HOCN * C_H) / D_HNCO;
                            N2_HNCO = ( (k_f[11] / k_K[11]) * C_H2O + k_f[12] * C_H2 ) / D_
                                HNCO;
145
                            C_NCO = ( N1_NCO + (N2_NCO * N1_HNCO) ) / ( 1 - (N2_NCO * N2_
                                HNCO) );
147
    /*The HNCO concentration is computed based on steady state*/
149                         C_HNCO = N1_HNCO + (N2_HNCO * C_NCO);

151 /*The NH concentration is computed based on steady state*/
                            D_NH2 = (k_f[21] / k_K[21]) * C_H + (k_f[22] / k_K[22]) * C_H2O
                                + (k_f[23] / k_K[23]) * C_H2 + k_f[24] * C_H + k_f[25] * C_
                                OH + k_f[26] * C_NO;
153                         N1_NH2 = k_f[19] * C_HNCO * C_H + C_NH3 * (k_f[21] * C_M + k_f[
                                22] * C_OH + k_f[23] * C_H);
                            N1_NH2 = N1_NH2 / D_NH2;
155                         N2_NH2 = (k_f[24] / k_K[24]) * C_H2 + (k_f[25] / k_K[25]) * C_
                                H2O;
                            N2_NH2 = N2_NH2 / D_NH2;
```

```
157
                        D_NH = (k_f[24] / k_K[24]) * C_H2 + (k_f[25] / k_K[25]) * C_H2O
                            + (k_f[27] + k_f[28]) * C_O2 + k_f[29] * C_H + k_f[30] * C_O
                             + (k_f[31] + k_f[32]) * C_OH + k_f[33] * C_NO;
159                     N1_NH = k_f[3] * C_HCN * C_O + k_f[14] * C_NCO * C_H + C_HNCO *
                            ( k_f[17] * (C_M + C_N2 * (1.5 - 1) ) + k_f[20] * C_O );
                        N1_NH = N1_NH / D_NH;
161                     N2_NH = (k_f[29] / k_K[29]) * C_H2 + (k_f[32] / k_K[32]) * C_H2O
                            ;
                        N2_NH = N2_NH / D_NH;
163                     N3_NH = k_f[24] * C_H + k_f[25] * C_OH;
                        N3_NH = N3_NH / D_NH;
165
                        D_N = (k_f[29] / k_K[29]) * C_H2 + (k_f[32] / k_K[32]) * C_H2O +
                             k_f[34] * C_OH + k_f[35] * C_O2 + k_f[36] * C_NO;
167                     N1_N = k_f[13] * C_NCO * (C_M + C_N2 * (1.5 - 1) ) + C_NO * ( (k
                            _f[34] / k_K[34]) * C_H + (k_f[35] / k_K[35]) * C_O ) + (k_f
                            [36] / k_K[36]) * C_N2 * C_O;
                        N1_N = N1_N / D_N;
169                     N2_N = k_f[29] * C_H + k_f[32] * C_OH;
                        N2_N = N2_N / D_N;
171
                        C_NH_upper = N1_NH + N2_NH * N1_N + N3_NH * N1_NH2;
173                     C_NH_lower = 1 - N2_NH * N2_N - N3_NH * N2_NH2;
                        C_NH = C_NH_upper / C_NH_lower;
175
    /*The NH2 concentration is computed based on steady state*/
177                     C_NH2 = N1_NH2 + N2_NH2 * C_NH;

179 /*The N concentration is computed based on steady state*/
                        C_N = N1_N + N2_N * C_NH;
181
    /*Reaction rates for the elementary reactions */
183                     w_1 = k_f[1] * ( C_CN * C_H2 - C_HCN * C_H / k_K[1] );
                        w_2 = k_f[2] * C_HCN * C_O;
185                     w_3 = k_f[3] * C_HCN * C_O;
                        w_4 = k_f[4] * ( C_CN * C_H2O - C_HCN * C_OH / k_K[4] );
187                     w_5 = k_f[5] * ( C_HCN * C_OH - C_HOCN * C_H / k_K[5] );
                        w_15 = k_f[15] * C_NCO * C_O;
189                     w_16 = k_f[16] * C_NCO * C_NO;
                        w_18 = k_f[18] * C_HNCO * C_O2;
191                     w_21 = k_f[21] * ( C_NH3 * C_M - C_NH2 * C_H * C_M / k_K[21] );
                        w_22 = k_f[22] * ( C_NH3 * C_OH - C_NH2 * C_H2O / k_K[22] );
193
                        w_23 = k_f[23] * ( C_NH3 * C_H - C_NH2 * C_H2 / k_K[23] );
195                     w_26 = k_f[26] * C_NH2 * C_NO;
                        w_27 = k_f[27] * C_NH * C_O2;
197                     w_28 = k_f[28] * C_NH * C_O2;
                        w_30 = k_f[30] * C_NH * C_O;
199                     w_31 = k_f[31] * C_NH * C_OH;
                        w_33 = k_f[33] * C_NH * C_NO;
201                     w_34 = k_f[34] * ( C_N * C_OH - C_NO * C_H / k_K[34] );
```

```
                        w_35 = k_f[35] * ( C_N * C_O2 - C_NO * C_O / k_K[35] );
203                     w_36 = k_f[36] * ( C_N * C_NO - C_N2 * C_O / k_K[36] );

205 /*Reaction rates of NO, HCN and NH3. Multiplying with 1000 to go from mole/cm^3 to kmole
        /m^3*/
            rr[16] = 1000 * (w_15 - w_16 + w_18 - w_26 + w_27 + w_28 + w_30 + w_31 - w_33 +
                 w_34 + w_35 - w_36);
207         /*rr[HCN_number] = 1000 * (w_1 - w_2 - w_3 + w_4 - w_5);*/
            rr[15] = 1000 * (- w_21 - w_22 - w_23);
209
    /*Alternative way of determining the rates based on r_NO = -r_NH3 - r_HCN - 2 * r_N2.*/
211 /*In other words balancing the N-atoms*/
            /*rr_N2 = 1000 * (w_16 + w_26 + w_33 + w_36);*/
213         /*rr[16] = - rr[15] - 2 * rr_N2;*/
    }
```

Listing D.2: UDF for implementing the LSP NO mechanism in Fluent - used for approach where NO is calculated with the standard Fluent NO_x post-processor

```
#include "udf.h"
#include "math.h"
/*****************************************************************************/
/* This UDF defines reaction rates for the species NO and NH3. HCN is outcommented  */
/* It is based on:                                                           */
/* "Pedersen, L. S., Glarborg, P. and Dam-Johansen, K. 1998."                */
/* "A Reduced Reaction Scheme for Volatile Nitrogen Conversion in Coal Combustion." */
/* "Combustion Science and Technology. 1998, 131, pp. 193-196."              */
/*                                                                           */
/*****************************************************************************/
DEFINE_NOX_RATE(LSP_UDF,c,t,Pollut,Pollut_Par,NOx)
{
        Pollut->fluct.fwdrate = 0.0;
        Pollut->fluct.revrate = 0.0;

        switch (Pollut_Par->pollut_io_pdf)
        {
        case IN_PDF:


/* The mechanism is implemented as a Fuel NOx udf replace                    */
/* Beware that the mechanism includes thermal NOx                            */
/* This can be excluded by importing the N2 concentration as zero            */
                if (NOx->fuel_nox && NOx->fuel_udf_replace){
/* defining variables*/
                double NOx_Rate, NH3_Rate, HCN_Rate;
                double  NOx_Rate_Forward=0;
                double  NOx_Rate_Backward=0;
                double  HCN_Rate_Forward=0;
                double  HCN_Rate_Backward=0;
                double  NH3_Rate_Forward=0;
                double  NH3_Rate_Backward=0;
/*The variables for the non steady state species that are provided by the combustion
calculations*/
                double C_O2, C_H2O, C_H2, C_N2, C_O, C_OH, C_H;
/* The total concentration is computed from the ideal gas law. Pressure / R *
    Temperature*/
/* unit is mole/cm^3*/
        double C_M = 101325 / (1000 * UNIVERSAL_GAS_CONSTANT * C_T(c,t));

/*The arrays for the constants for the k-values are initialized*/
        double k_f[37];
        double k_K[37];
```

```
/*The variables for the concentration of NO, HCN, NH3*/
        double C_NO, C_HCN, C_NH3;

/*The variables for the steady state and equilibrium species are initialized*/
        double C_HOCN, C_CN, C_NCO, C_HNCO, C_NH, C_NH2, C_N;

/*The variables for the reaction rates for the reactions of the scelatal mechanism*/
        double w_1, w_2, w_3, w_4, w_5, w_15, w_16, w_18, w_21, w_22;
        double w_23, w_26, w_27, w_28, w_30, w_31, w_33, w_34, w_35, w_36;
        double rr_N2;

/*The variables for intermediates used to compute the steady state species are
    initialized*/
        double HOCN_upper, HOCN_lower, CN_upper, CN_lower, D_NCO, N1_NCO, N2_NCO, D_HNCO
            ,N1_HNCO,
                N2_HNCO, D_NH2, N1_NH2, N2_NH2, D_NH, N1_NH, N2_NH, N3_NH, D_N, N1_N, N2
                    _N,
                C_NH_upper, C_NH_lower;


/*Constants for the rate constants for the forward reaction of the 36 reactions in the
    sceletal mechanism*/
        double Cons_k_A[37] = {0, 3.6e8, 1.4e4, 3.5e3, 8e12, 5.9e4, 2e7, 1.5e4, 6.4e5, 6
            e13,
                7.5e12, 6.4e5, 7.6e2, 3.1e16, 5e13, 4.7e13, 1.4e18, 1.1e16, 1e12, 2.2e7,
                    9.6e7,
                2.2e16, 2.0e6, 6.4e5, 4e13, 4e6, 1.3e16, 4.6e5, 1.3e6, 3e13, 9.2e13, 2
                    e13, 5e11,
                2.9e14, 3.8e13, 6.4e9, 3.3e12};

        double Cons_k_b[37] = {0, 1.55, 2.64, 2.64, 0, 2.4, 2.0, 2.64, 2.0, 0, 0, 2, 3,
            -0.5, 0,
                0, -1.73, 0, 0, 1.7, 1.41, 0, 2.04, 2.39, 0, 2, -1.25, 2, 1.5, 0, 0, 0,
                    0.5,
                -0.4, 0, 1, 0.3};

        double Cons_k_E[37] = {0, 3000, 4980, 4980, 7450, 12500, 2000, 4000, 2560, 0,
            -389, 2560,
                4000, 48000, 0, 0, 763, 86000, 35000, 3800, 8520, 93470, 566, 10171,
                    3650, 1000,
                0, 6500, 100, 0, 0, 0, 2000, 0, 0, 6280, 0};

/*Constants for the equilibrium constants for the 36 reactions in the sceletal mechanism
    */

        double Cons_EQ_A[37] = {0, 0.1184e-3, 0, 0, 0.8317e-2, 0.22e-1, 0, 0, 0, 0, 0, 0
            .4231e0,
                0.3365e-1, 0, 0, 0, 0, 0, 0, 0, 0.1629e7, 0.9605e2, 0.6746e4, 0.3367
                    e2, 0.4794e0,
                0, 0, 0, 0.8079e0, 0, 0, 0.1150e-1, 0, 0.2745e-1, 0.1066e2, 0.5007e0};

```

```
        double Cons_EQ_b[37] = {0, 0.9545, 0, 0, 0.6244, 0.1689, 0, 0, 0, 0, 0, -0.4127e
            -1, 0.3713,
82              0, 0, 0, 0, 0, 0, 0, 0, 0.2232, -0.4878, -0.8179, -0.3772, -0.4711e-1,
                    0, 0, 0, -0.1602,
                0, 0, 0.1699, 0, 0.3095, -0.9635e-1, -0.9698e-1};
84
        double Cons_EQ_E[37] = {0, 0.1065e5, 0, 0, 0.2599e4, -0.3764e4, 0, 0, 0, 0, 0, 0
            .3862e4, 0.4190e4,
86              0, 0, 0, 0, 0, 0, 0, 0, -0.5558e5, 0.4984e4, -0.3068e4, 0.5764e4, 0.1382
                    e5, 0, 0, 0,
                0.1212e5, 0, 0, 0.2017e5, 0, 0.2458e5, 0.1593e5, 0.3771e5};
88      int i,j;
    /*The forward rate constants and the equilibrium constants are computed*/
90  /*The k-values for the forwards reactions and the equilibrium K of the sceletal
        mechanism are computed from
        k = B * T^n * exp(-E / RT). The UNIVERSAL_GAS_CONSTANT needs to be defined in
            cal/ (mole*K).
92      Since the E-values used to compute the rate constants are given i cal/mole.
            Hence the multiplication
        with 0.23885 in the denomenator (joule to cal)*/
94                      for (i=0; i <= 36; i++)
                        {
96                              k_f[i] = Cons_k_A[i] * pow( C_T(c,t), Cons_k_b[i]) * exp
                                    (-Cons_k_E[i] * 1000 /
                                        (0.23885 * UNIVERSAL_GAS_CONSTANT * C_T(c,t)));
98                              k_K[i] = Cons_EQ_A[i] * pow(C_T(c,t) , Cons_EQ_b[i]) *
                                    exp(Cons_EQ_E[i] / C_T(c,t));
                        }
100 /*The concentrations of the seven active species which are computed in the main
        equationssystem
        are collected in mole/cm^3 as these are the units of the k constants. */
102                     C_H2 = MAX( 1.e-28, MOLECON(Pollut, H2)/1e6);
                        C_H2O = MAX( 1.e-28, MOLECON(Pollut, H2O)/1e6);
104                     C_O2 = MAX( 1.e-28, MOLECON(Pollut, O2)/1e6);
                        C_N2 = MAX( 1.e-28, MOLECON(Pollut, N2)/1e6);
106                     C_H = MAX( 1.e-28, MOLECON(Pollut, H)/1e6);
                        C_O = MAX( 1.e-28, MOLECON(Pollut, O)/1e6);
108                     C_OH = MAX( 1.e-28, MOLECON(Pollut, OH)/1e6);
    /*And the concentration of NO, HCN and NH3 in mole / cm3*/
110                     C_NO = MAX( 1.e-28, MOLECON(Pollut, IDX(NO))/1e6);
                        C_HCN = 0; /*MAX( 1.e-28, MOLECON(Pollut, IDX(HCN))/1e6);*/
112                     C_NH3 = MAX( 1.e-28, MOLECON(Pollut, IDX(NH3))/1e6);

114 /*The steady state species HOCN, CN, NCO, HNCO, NH, NH2 and N are computed*/
    /*The HOCN concentration is computed based on steady state*/
116                     HOCN_upper = k_f[5] * C_HCN * C_OH;
                        HOCN_lower = (k_f[5] / k_K[5]) * C_H +  k_f[6] * C_H + k_f[7] *
                            C_O + k_f[8] * C_OH;
118                     if (HOCN_lower == 0)
                        {
120                             HOCN_lower = 1.e-20;
                        }
```

```
122                         C_HOCN = HOCN_upper / HOCN_lower;

124 /*The CN concentration is computed based on steady state*/
                            CN_upper = (k_f[1] / k_K[1]) * C_HCN * C_H  + (k_f[4] / k_K[4])
                                 * C_HCN * C_OH;
126                         CN_lower = k_f[1] * C_H2 + k_f[4] * C_H2O + k_f[9] * C_OH + k_f[
                                 10] * C_O2;
                            C_CN = CN_upper / CN_lower;
128
    /*The NCO concentration is computed based on steady state*/
130                         D_NCO = (k_f[11] / k_K[11]) * C_H2O + k_f[12] * C_H2 + k_f[13] *
                                  (C_M + C_N2 * (1.5 - 1)) + k_f[14] * C_H + k_f[15] * C_O +
                                 k_f[16] * C_NO;
                            N1_NCO = C_HOCN * ( k_f[7] * C_O + k_f[8] * C_OH ) + C_CN * ( k_
                                 f[9] * C_OH +  k_f[10] * C_O2 ) + k_f[2] * C_HCN * C_O;
132                         N1_NCO = N1_NCO / D_NCO;
                            N2_NCO = k_f[11] * C_OH + (k_f[12] / k_K[12]) * C_H;
134                         N2_NCO = N2_NCO / D_NCO;

136                         D_HNCO = k_f[11] * C_OH + (k_f[12] / k_K[12]) * C_H + k_f[17] *
                                 (C_M + C_N2 * (1.5 - 1)) + k_f[18] * C_O2 + k_f[19] * C_H +
                                 k_f[20] * C_O;
                            N1_HNCO = (k_f[6] * C_HOCN * C_H) / D_HNCO;
138                         N2_HNCO = ( (k_f[11] / k_K[11]) * C_H2O + k_f[12] * C_H2 ) / D_
                                 HNCO;

140                         C_NCO = ( N1_NCO + (N2_NCO * N1_HNCO) ) / ( 1 - (N2_NCO * N2_
                                 HNCO) );

142 /*The HNCO concentration is computed based on steady state*/
                            C_HNCO = N1_HNCO + (N2_HNCO * C_NCO);
144
    /*The NH concentration is computed based on steady state*/
146                         D_NH2 = (k_f[21] / k_K[21]) * C_H + (k_f[22] / k_K[22]) * C_H2O
                                 + (k_f[23] / k_K[23]) * C_H2 + k_f[24] * C_H + k_f[25] * C_
                                 OH + k_f[26] * C_NO;
                            N1_NH2 = k_f[19] * C_HNCO * C_H + C_NH3 * (k_f[21] * C_M + k_f[
                                 22] * C_OH + k_f[23] * C_H);
148                         N1_NH2 = N1_NH2 / D_NH2;
                            N2_NH2 = (k_f[24] / k_K[24]) * C_H2 + (k_f[25] / k_K[25]) * C_
                                 H2O;
150                         N2_NH2 = N2_NH2 / D_NH2;

152                         D_NH = (k_f[24] / k_K[24]) * C_H2 + (k_f[25] / k_K[25]) * C_H2O
                                 + (k_f[27] + k_f[28]) * C_O2 + k_f[29] * C_H + k_f[30] * C_O
                                  + (k_f[31] + k_f[32]) * C_OH + k_f[33] * C_NO;
                            N1_NH = k_f[3] * C_HCN * C_O + k_f[14] * C_NCO * C_H + C_HNCO *
                                 ( k_f[17] * (C_M + C_N2 * (1.5 - 1) ) + k_f[20] * C_O );
154                         N1_NH = N1_NH / D_NH;
                            N2_NH = (k_f[29] / k_K[29]) * C_H2 + (k_f[32] / k_K[32]) * C_H2O
                                 ;
156                         N2_NH = N2_NH / D_NH;
```

```
                        N3_NH = k_f[24] * C_H + k_f[25] * C_OH;
158                     N3_NH = N3_NH / D_NH;

160                     D_N = (k_f[29] / k_K[29]) * C_H2 + (k_f[32] / k_K[32]) * C_H2O +
                              k_f[34] * C_OH + k_f[35] * C_O2 + k_f[36] * C_NO;
                        N1_N = k_f[13] * C_NCO * (C_M + C_N2 * (1.5 - 1) ) + C_NO * ( (k
                             _f[34] / k_K[34]) * C_H + (k_f[35] / k_K[35]) * C_O ) + (k_f
                             [36] / k_K[36]) * C_N2 * C_O;
162                     N1_N = N1_N / D_N;
                        N2_N = k_f[29] * C_H + k_f[32] * C_OH;
164                     N2_N = N2_N / D_N;

166                     C_NH_upper = N1_NH + N2_NH * N1_N + N3_NH * N1_NH2;
                        C_NH_lower = 1 - N2_NH * N2_N - N3_NH * N2_NH2;
168                     C_NH = C_NH_upper / C_NH_lower;

170 /*The NH2 concentration is computed based on steady state*/
                        C_NH2 = N1_NH2 + N2_NH2 * C_NH;
172
    /*The N concentration is computed based on steady state*/
174                     C_N = N1_N + N2_N * C_NH;

176 /*Reaction rates for the elementary reactions */
                        w_1 = k_f[1] * ( C_CN * C_H2 - C_HCN * C_H / k_K[1] );
178                     w_2 = k_f[2] * C_HCN * C_O;
                        w_3 = k_f[3] * C_HCN * C_O;
180                     w_4 = k_f[4] * ( C_CN * C_H2O - C_HCN * C_OH / k_K[4] );
                        w_5 = k_f[5] * ( C_HCN * C_OH - C_HOCN * C_H / k_K[5] );
182                     w_15 = k_f[15] * C_NCO * C_O;
                        w_16 = k_f[16] * C_NCO * C_NO;
184                     w_18 = k_f[18] * C_HNCO * C_O2;
                        w_21 = k_f[21] * ( C_NH3 * C_M - C_NH2 * C_H * C_M / k_K[21] );
186                     w_22 = k_f[22] * ( C_NH3 * C_OH - C_NH2 * C_H2O / k_K[22] );
                        w_23 = k_f[23] * ( C_NH3 * C_H - C_NH2 * C_H2 / k_K[23] );
188                     w_26 = k_f[26] * C_NH2 * C_NO;
                        w_27 = k_f[27] * C_NH * C_O2;
190                     w_28 = k_f[28] * C_NH * C_O2;
                        w_30 = k_f[30] * C_NH * C_O;
192                     w_31 = k_f[31] * C_NH * C_OH;
                        w_33 = k_f[33] * C_NH * C_NO;
194                     w_34 = k_f[34] * ( C_N * C_OH - C_NO * C_H / k_K[34] );
                        w_35 = k_f[35] * ( C_N * C_O2 - C_NO * C_O / k_K[35] );
196                     w_36 = k_f[36] * ( C_N * C_NO - C_N2 * C_O / k_K[36] );

198 /*%%%%%%%%%%%%%%%%%%%%%%%%%%%%%%%%Reaction rates for NO, HCN and NH3
        %%%%%%%%%%%%%%%%%%%%%%%%%%%%%%%%*/
    NOx_Rate = w_15 - w_16 + w_18 - w_26 + w_27 + w_28 + w_30 + w_31 - w_33 + w_34 + w_35 -
        w_36;
200 /*HCN_Rate = w_1 - w_2 - w_3 + w_4 - w_5;*/
    NH3_Rate = - w_21 - w_22 - w_23;
202
```

```
204
    /*Forward and backwards reaction rates are defined according to the Fluent communication
        requirements*/
206 /* See Fluent UDF manual section 2.3.10*/
    if (NOx_Rate>0)
208         NOx_Rate_Forward=NOx_Rate;
            else
210                 NOx_Rate_Backward = NOx_Rate;

212 if (NH3_Rate>0)
            NH3_Rate_Forward=NH3_Rate;
214         else
            NH3_Rate_Backward=NH3_Rate;
216

218 /* The reaction rates are converted to Fluent NOx postprocessor units mol-m3-s by
        multiplying with 1e6*/

220                         if (POLLUT_EQN(Pollut_Par) == EQ_NO){
                            Pollut->fluct.fwdrate = NOx_Rate*1e6;
222                         Pollut->fluct.revrate = NOx_Rate_Backward*1e6 /MAX(1.e-20, C_
                                POLLUT(c,t,0));
                            }
224
                            /*if (POLLUT_EQN(Pollut_Par) == EQ_HCN){
226                         Pollut->fluct.fwdrate = HCN_Rate/v0;
                            Pollut->fluct.revrate = 0; /*HCN_Rate_Backward /
228                         MAX(1.e-20, C_POLLUT(c,t,0));
                            }*/
230
                            if (POLLUT_EQN(Pollut_Par) == EQ_NH3){
232                         Pollut->fluct.fwdrate = NH3_Rate_Forward*1e6;
                            Pollut->fluct.revrate = NH3_Rate_Backward*1e6 /MAX(1.e-20, C_
                                POLLUT(c,t,2));
234                         }

236                 }

238         case OUT_PDF:

240                 break;

242         default:
                    ;
244         }
    }
```

Appendix E

Flow problem analysis

One major problem when it comes to obtaining agreement between modeling and experimental data from the setup has been to obtain the correct flow field and turbulence levels. It appears that every approach taken in order to model the entrance of the inclined jet has resulted in a jet attachment to the top wall, which eventually results in underprediction of the mixing and consequently a very long reaction zone compared to the experimental modeling. Figure E.1 (left) displays the predicted velocity contours with jet attachment and Figure E.1 (right) shows the corresponding predicted CO contours for setting 2.

It is suspected that the jet attachment is not appearing in reality for the setting 2 conditions, but only in the CFD modeling. So in order to avoid this jet attachment, the jet entrance was elongated 5mm into the FBS area, this made it possible to obtain solutions without jet attachment, and these solutions obtain significantly different results as Figure E.2 illustrates.

It appears that in the elongated jet solution, the CO conversion is significantly faster due to enhanced mixing, this picture is also in better agreement

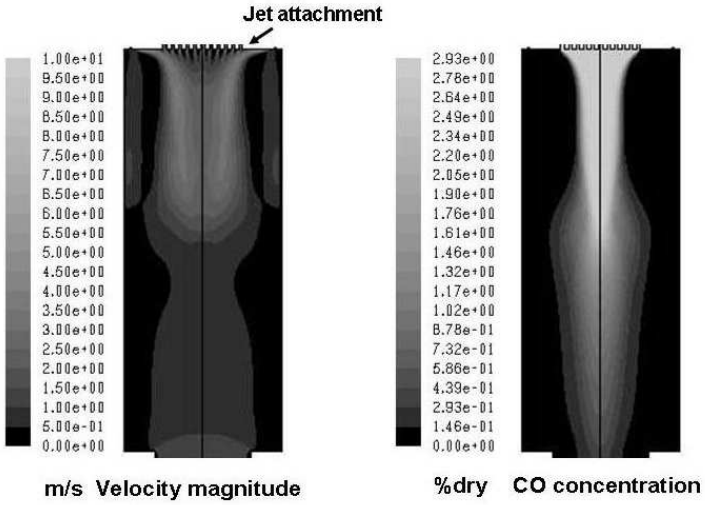

Figure E.1: Left: contour plot of velocity magnitude - illustrating the jet attachment. Right: Contour plot of the predicted CO concentration. These results obtained with standard k-ϵ turbulence model.

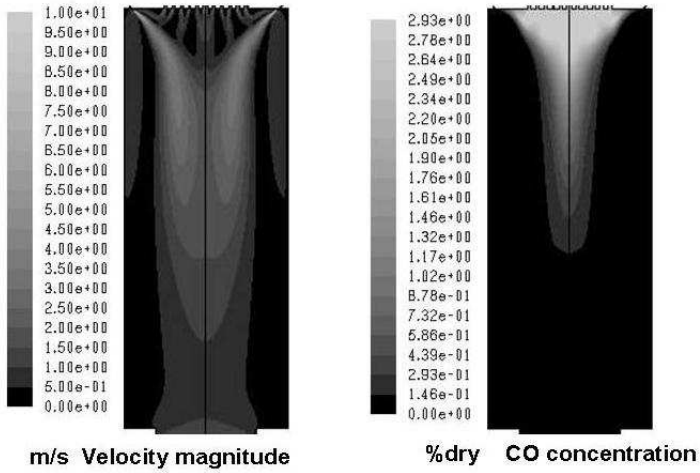

Figure E.2: Left: contour plot of velocity magnitude - whit elongated jet entrance. Right: Contour plot of the CO concentration. These results obtained with standard k-ϵ turbulence model.

with experimental results seen on Figure E.3.

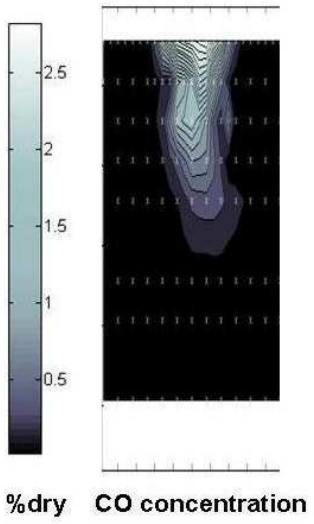

Figure E.3: Experimental CO contours.

When comparing the axial velocities at the first LDA measurement plane, it appears that the elongated jet solution predictions are in slightly better agreement with the experimental velocity measurements as Figure E.5 shows, also the predicted levels of turbulent velocity fluctuations are in better agreement with the experimental data, indicating that jet attachment does not take place. Furthermore a visual inspection of the secondary air injection position did indicate a free jet emerging into the FBS area.

Numerous attempts were made in order to obtain results without jet attachment, including simulation with several sized grids and several turbulence models were tested (SKE, RNG, Realizable, SST kw, RSM and laminar inlet zone). Various input values for the jet inlet boundary were attempted (turbulent kinetic energy 0-100%) but it still resulted in jet attachment. A 3D solution was sought, but this also resulted in jet attachment. Unsteady

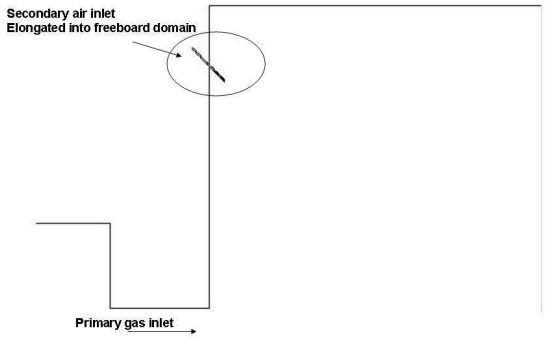

Figure E.4: Illustration of jet entrance elongation.

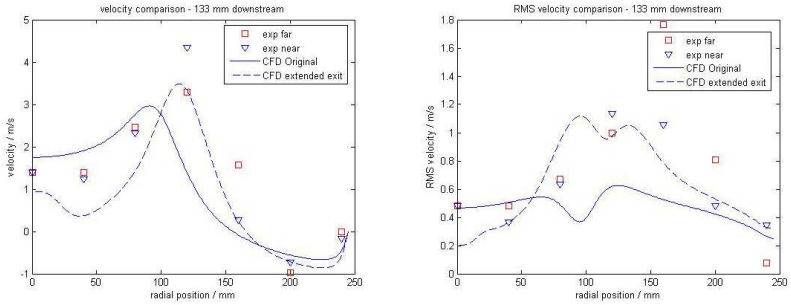

Figure E.5: Left: Axial velocity Right: Velocity fluctuations - 133 mm downstream of the FBS entrance.

modeling was tried with the same result. It was also attempted to include higher hydrocarbon in the fuel inlet stream, with the theory that combustion of these in the shear layer could result in a local pressure increase that could avoid jet attachment, but still jet attachment was obtained. Definition of slip wall at the jet inlet also lead to jet attachment.

The most simple, and the only way that the jet attachment was avoided, was to extend the jet entrance into the freeboard section as illustrated in Figure E.4.

E.1 Jet attachment theory - the Coanda effect

The attachment of a fluid to a solid surface is often described as the Coanda effect after Henri Coanda, who was one of the first to encounter the phenomenon during his early work with developing aircraft jet engines. The Coanda effect occurs for both gases and liquids [1] and can have various causes. When a stream of water from a tab attaches to a spoon and bends with the surface it is due to surface tension or Van der Waals attractive forces. When a gas flow attaches to a solid surface it is often due to shear flow effects; reduced entrainment from the wall side of the jet results in a lower pressure at the wall side. This ejector effect can pull the jet flow toward the solid surface [2, 3]. Other forces that can cause jet attachment are buoyancy forces, this is an accepted theory in the area of ventilation and air conditioning of rooms [4]. In the FBS the reaction between the inclined jet air and the primary combustion gas, which contains large amounts of CO, might result in a net decrease in molecules (especially when applying global mechanisms). This effect would also lower the pressure in the wall side region, thereby contributing to the Coanda effect.

E.2 References

[1] T. Panitz and D.T. Wasan. *AIChe J.*, 18:51–57, 1972.

[2] J. Hoch and L.M. Jiji. *J. Fluids Engineering*, 103:154–161, 1981.

[3] S.V. Alekseenko and D.M. Markovich. *J. Appl. Mech. Tech. Phys.*, 38:417–422, 1997.

[4] A. Triboix and D. Marchal. *Int. J. Heat Mass Transfer*, 43:2769–2775, 2000.